High-Field Transport at Heavily-Doped SiC Schottky Contacts and Formation of Non-Alloyed Ohmic Contacts

2024

Masahiro HARA

High-Field Transport at Heavily-Doped SiC Schottky Contacts and Formation of Non-Alloyed Ohmic Contacts

2024

Masahiro HARA

Electronic Science and Engineering
Kyoto University

Abstract

The semiconductor industry based on Silicon (Si) electronics has provided a core in modern society, and the rapid advances in Si technology have drastically improved our lives. To tackle the recent worldwide environmental issues, on the other hand, further energy conservation and novel functions are required for electronics, as well as higher performance. *Power electronics* and *high-temperature electronics* play a vital role in efficiently utilizing energy resources and electricity, the significance of which has been rapidly increasing. However, currently available Si-based electronics has encountered the performance limit determined by the material properties of Si, making it challenging to achieve innovative breakthroughs in these fields.

Silicon carbide (SiC), which possesses a high critical breakdown electric field ($\sim 2.5\,\mathrm{MV/cm}$) and wide bandgap ($3.26\,\mathrm{eV}$), is one of the most promising semiconductor materials for low-loss and high-voltage power devices and high-temperature operational logic transistors. Thanks to extensive research and development over the decades, SiC power devices such as Schottky barrier diodes (SBDs) and metal-oxide-semiconductor field-effect transistors (MOSFETs) have already been in mass production and commercialization. Regarding SiC-based high-temperature electronics, the successful operation of transistors and integrated circuits (ICs) at a temperature above 300°C has been demonstrated by several groups. On the other hand, several technical issues still hinder further improvement in the performance, reliability, and processing of SiC devices. Formation of ohmic contacts with a sufficiently low contact resistivity ($\rho_\mathrm{c} < 10^{-6}\,\Omega\mathrm{cm}^2$) through a low-temperature process is particularly important among these critical issues.

An ohmic contact is a type of metal/semiconductor junction at which current can flow in both directions and is an essential component to connect semiconductor devices to external circuits. In the case of SiC, the wide bandgap leads to a high energy barrier ($> 1\,\mathrm{eV}$) at metal/SiC interfaces, making it difficult to form low-resistance ohmic contacts just by depositing an electrode metal on SiC. Hence, annealing at a very high temperature (~ 1000°C) after the electrode deposition on heavily-doped SiC (doping density: $N_\mathrm{d} > 1 \times 10^{19}\,\mathrm{cm}^{-3}$) has widely been adopted to obtain a low contact resistivity. However, the mechanism of ohmic contact formation through the high-temperature treatment is not well understood even now, and thus, no quantitative guidelines exist to form good ohmic contacts on SiC. Besides, the high-temperature process has various negative impacts like surface roughing,

metal melting, and even device performance degradation. In order to resolve these issues, it is indispensable to clarify the fundamental properties of *non-alloyed metal/heavily-doped SiC interfaces* formed without performing high-temperature sintering, that is, *heavily-doped SiC Schottky interfaces*.

In this dissertation, the author systematically studies the barrier height and carrier transport at Schottky (non-alloyed) contacts formed on heavily-doped n-type SiC. Based on the understanding of the high-field carrier transport phenomena, namely, tunneling phenomena, at metal/heavily-doped SiC Schottky interfaces, a physical model to predict the contact resistivity at non-alloyed SiC ohmic contacts is proposed, and a design guideline for the formation of low-resistance ohmic contacts is presented.

In Chapter 2, the barrier height at metal/heavily-doped n-type SiC Schottky interfaces was carefully investigated through three different techniques. A method was established to accurately determine the barrier height in heavily-doped SiC SBDs, considering electron tunneling through a very thin Schottky barrier ($\sim 10\,\mathrm{nm}$). A significant barrier drop ($\sim 0.2\,\mathrm{eV}$) was observed in the Ni/heavily-doped SiC SBDs ($N_\mathrm{d} = 2 \times 10^{19}\,\mathrm{cm}^{-3}$), which is quantitatively explained by image force lowering caused by a high electric field at the Schottky interface ($>$ MV/cm) even at zero bias. Wide-range controllability of the barrier height (0.7–1.6 eV) regardless of the donor density of SiC was also demonstrated by employing various metals for Schottky electrodes.

In Chapter 3, the author fabricated vertical SBD structures on heavily-doped n-type SiC epitaxial layers and numerically analyzed the I–V characteristics based on the direct tunneling (DT) model, which includes the thermionic field emission (TFE) and field emission (FE) models. It turned out that the carrier transport in heavily-doped SiC Schottky structures ($N_\mathrm{d} > 10^{17}\,\mathrm{cm}^{-3}$) is quantitatively described by the DT process. Investigation of the energy where electron tunneling most frequently occurs (defined as E_peak) revealed that the TFE transport is predominant in forward-biased heavily-doped n-type SiC SBDs (N_d: mid-$10^{17}\,\mathrm{cm}^{-3}$–$1 \times 10^{19}\,\mathrm{cm}^{-3}$), while a higher electric field under a reverse bias changes the dominant tunneling process from TFE to FE (N_d: above mid-$10^{18}\,\mathrm{cm}^{-3}$). The N_d-independent critical conditions regarding the electric field and the barrier thickness for the TFE-FE transition were clarified, carefully considering the sharply changing electric field distribution in heavily-doped SiC Schottky structures.

In Chapter 4, phosphorus ion (P^+) implantation was conducted to fabricate vertical SBD structures (1×10^{17}–$8 \times 10^{19}\,\mathrm{cm}^{-3}$), and the carrier transport characteristics were compared with the Schottky contacts formed on epitaxial layers. The current density flowing through metal/heavily P^+-implanted SiC interfaces was several orders of magnitude larger than that on epitaxial layers, even with a similar barrier height and donor density. The enhanced tunneling current is plausibly explained by trap-assisted tunneling (TAT), which involves electron tunneling via deep levels induced by implantation damages. The numerical calculation of the TAT current was then performed by assuming various trap levels in the implanted layer, and it was speculated which kind of traps dominantly contribute to the

enhanced current observed in metal/heavily P^+-implanted SiC Schottky structures.

In Chapter 5, non-alloyed Ti and Mg contacts were formed on heavily P^+-implanted SiC (4×10^{18}–$2 \times 10^{20}\,\mathrm{cm^{-3}}$), and the contact resistivity (ρ_c) was systematically investigated through experiment and numerical calculation of the DT current. When N_d is below mid-$10^{19}\,\mathrm{cm^{-3}}$, the measured ρ_c value was much lower than expected from the DT calculation, which is qualitatively explained by the significant contribution of TAT. In a higher N_d range above $10^{20}\,\mathrm{cm^{-3}}$, the experimental ρ_c sharply decreased with increasing N_d, which is quantitatively predictable by the numerical calculation of the DT current. An extremely low ρ_c of 1–$2 \times 10^{-7}\,\Omega\mathrm{cm^2}$ was demonstrated for non-alloyed Mg and Ti ohmic contacts without high-temperature sintering ($\sim 1000^\circ\mathrm{C}$) by utilizing very high-dose P^+ implantation ($2 \times 10^{20}\,\mathrm{cm^{-3}}$). Through the experiment and calculation, a physics-based model considering the contributions of DT and TAT for ρ_c at non-alloyed ohmic contacts was proposed. Besides, based on the proposed model, a quantitative guideline for designing low-resistance non-alloyed ohmic contacts on P^+-implanted SiC was presented: a very low ρ_c ($< 10^{-6}\,\Omega\mathrm{cm^2}$) is achievable with a barrier height lower than about 1 eV and a donor density higher than about $3 \times 10^{19}\,\mathrm{cm^{-3}}$.

In Chapter 6, the summary of this dissertation and future prospects are given.

Acknowledgments

First of all, the author would like to express his most sincere gratitude to Professor Tsunenobu Kimoto for continuous and attentive supervision, invaluable guidance based on immense knowledge and experience, and considerate encouragement. He would like to particularly acknowledge Professor Masashi Shiraishi and Associate Professor Mitsuru Funato for their insightful comments and suggestions during regular meetings and for refereeing this thesis. He would also be grateful to Dr. Fabrizio Roccaforte at CNR Institute for Microelectronics and Microsystems (CNR IMM) for reviewing this dissertation and highly regarding this work.

The author would like to greatly appreciate Assistant Professor Mitsuaki Kaneko, who, with a good-natured personality, has offered constructive advice and tremendous support in daily work. He would also like to show deep gratitude to Assistant Professor Hajime Tanaka at Osaka University for the insightful comments and suggestions that were indispensable in accomplishing the numerical calculation in this study. He has significantly benefited from Associate Professor Yusuke Nishi at National Institute of Technology, Maizuru College, and Associate Professor Masahiro Horita at Nagoya University for their dedication to maintaining and improving experimental facilities.

The author would deeply appreciate Professor Heiji Watanabe at Osaka University for providing invaluable suggestions on research grant application writing and kindly accepting him as a postdoc researcher after graduation. He is very much obliged to Dr. Yasuo Koide and Dr. Toshihide Nabatame at the National Institute for Material Science (NIMS) for offering an opportunity to work on gallium nitride devices, through which he was able to gain extended knowledge and precious experiences. Special thanks are also given to all NIMS staff for their extensive support.

He is indebted to Dr. Satoshi Asada, who coached him a lot when he was an undergraduate student, including how to proceed with experiments and write logical sentences. He also appreciates Lecturer Takuya Maeda at the University of Tokyo for sharing deep insights into Schottky contacts through fruitful discussions. He would like to acknowledge Assistant Professor Takuma Kobayashi at Osaka University, who has offered heartfelt encouragement and helpful advice on an academic career.

He owes an important debt to what Assistant Professor Kazutaka Kanegae at Kyoto Institute of Technology did to make experimental environments in the laboratory neater

and more useful. The author has been stimulated by Dr. Keita Tachiki's outstanding research achievement and is grateful for kindly talking to him as a senior colleague. Deep gratitude goes to Dr. Koji Ito, Dr. Toshiki Miyatani, and Mr. Naoki Kanegami for sharing a joyful time and offering valuable suggestions during regular meetings.

The author profoundly appreciates Mr. Ryoya Ishikawa's considerable contribution to the laboratory. It is a precious memory of laboratory life, not only the pleasant times talking about research subjects and favorite music but also the difficult times handling many things outside of research. He also acknowledges Mr. Kyota Mikami for sharing enjoyable times and fruitful discussions and for supporting a lot in maintaining experimental equipment.

He is grateful to Mr. Takeaki Kitawaki, Mr. Kotaro Kuwahara, Mr. Manato Takayasu, Mr. Keishiro Maeda, and Mr. Kento Nomoto for working together on the physics of metal/heavily-doped SiC interfaces.

He is obliged to Mr. Hajime Takayama and Mr. Koki Izumi for their warmhearted encouragement as the same grade Ph.D. colleagues. Profound acknowledgments also go to Ms. Akane Adachi, Mr. Takao Saiki, Mr. Hiroyuki Dannoshita, and Mr. Yusuke Hiki, whose passionate attitude toward research has greatly motivated the author. Here, he also wishes to thank his friends, especially Mr. Chansoon Ku, Mr. Toshiya Kobayashi, and Mr. Kazutaka Yamada, who have supported him in many ways.

The author sincerely thanks Mr. Akio Kawamoto's enthusiastic teaching and encouragement to improve his English skills.

Special thanks go to all the laboratory members; Dr. Stefanakis Dionysios, Mr. Xilun Chi, Mr. Ryosuke Matsui, Mr. Masashi Nakajima, Mr. Shoma Yamashita, Mr. Yuto Tsuchiya, Mr. Takuya Ohku, Mr. Makoto Imuro, Mr. Mizuki Sato, Mr. Qimin Jin, Mr. Euihyeon Do, Mr. Gaku Gouhara, Mr. Katsuya Takahashi, Mr. Noriyuki Maeda, Mr. Taiga Matsuoka, Mr. Haruki Fujii, Mr. Akira Inoue, Mr. Shunya Shibata, Mr. Yuta Murakami, Mr. Shunsei Muraki, Mr. Ryusuke Ikeda, Mr. Shota Kozakai, Mr. Shion Toshimitsu, Mr. Genki Hiraoka, Mr. Ryoma Ito, Mr. Yuki Nakahara, Mr. Ryo Hasebe, and Mr. Tatsuki Yoshida. He also wishes to thank Ms. Yoriko Ohnaka, Ms. Chikako Tan, and Ms. Nami Fukao for their tremendous and attentive support.

The author's research activities have financially been supported by the Japan Society for the Promotion of Science (JSPS) through a Garnt-in-Aid for JSPS Fellows (Nos. 21J22891 and 22KJ1709), Doctoral Program for World-leading Innovative and Smart Education (WISE Program), and Yoshida Scholarship Foundation.

Finally, the author would like to extend his sincere gratitude to his parents, grandparents, sisters, and partner for their understanding and selfless love.

Kyoto, January, 2024
Masahiro HARA

Contents

Chapter 1

Introduction

1.1 Background

The term "*handotai*" (semiconductor) has become more familiar to ordinary citizens mainly due to the recent "*handotai busoku*" (semiconductor chip shortage), especially since 2021. The worldwide insufficient supply of semiconductor wafers and devices has significantly affected the production of electronic hardware, home appliances, and automobiles, to name a few. Consequently, the severe situation triggered us to appreciate how vital role the semiconductor industry plays in a highly civilized society.

Currently, almost all semiconductor devices are fabricated with silicon (Si), owing to the availability of large, low-priced, and high-quality single crystal wafers, a mature device fabrication process, and a deep understanding of the physical properties. Large-scale integrated circuits (LSIs) built with complementary metal-oxide-semiconductor (CMOS) technology are one of the most synonymous applications of Si devices. Decades of progress in the device fabrication process have enabled highly integrated circuits (ICs), dramatically improving the performance of computers and mobile gadgets year by year. *Power electronics*, proposed by Newell in 1973 [1], is another important implementation of Si devices. The function of power electronics is to control electrical power (i.e., voltage and/or frequency) to suitable forms, which is required several times during the delivery of electricity from power plants to our houses. The systems with a novel concept of power conversion based on fast switching of power semiconductor devices achieved higher energy efficiency than conventional linear regulators and rotary converters.

While Si-based devices and systems have provided us with innovative changes in the past decades, requirements for electronics are not only performance improvements but also further energy conservation and novel functions in modern society, which faces worldwide environmental issues and is rapidly becoming more developed and information-oriented. Taking power electronics, for instance, the conversion efficiency is insufficient in the currently available Si-based system. The performance of Si power devices has been improved, boosted by long-standing research and development, and is now approaching the theoretical limit

determined by the material properties of Si. Despite its maturity, however, the efficiency of Si power electronics is typically 85–95%, that is, about 10% of electrical power is wasted as heat at each conversion stage.

From an aspect of energy resource utilization, besides, the emphasis placed on *high-temperature electronics* [2, 3], which involves semiconductor devices and ICs operational at an elevated temperature, has been increasing. When drilling deeper into the earth for natural resource extraction and effective use of geothermal energy, for example, the underground ambient temperature reaches over 300°C. Thus, control and sensing systems must work stably at such a high temperature. However, it is inherently difficult for Si devices to operate at a temperature higher than 300°C, requiring severe thermal management with an external cooling system.

To overcome the "*Si limits*" and meet the needs of next-generation electronics, wide-bandgap (WBG) semiconductor materials that possess a higher critical breakdown electric field and a larger bandgap than Si have attracted considerable attention. Among several WBG semiconductors like gallium nitride (GaN), gallium oxide (Ga_2O_3), and diamond, silicon carbide (SiC) is widely accepted as one of the most promising materials because of the many advantages described in the next section.

1.2 Silicon Carbide (SiC)

1.2.1 Features of SiC

SiC is a IV-IV compound semiconductor containing an equal amount of Si and carbon (C) atoms. The chemical bonding between these atoms is very strong, giving this material high physical and chemical stability, high thermal conductivity [4], and unique electrical properties. Table 1.1 summarizes the major material properties of Si, 3C-SiC, 4H-SiC, and 6H-SiC [5–17]. Among quite a wide variety of polytypes, which are classified based on the stacking sequence of Si-C pairs, 4H-SiC is a particularly suitable material for kinds of electronic device applications because of its high electron mobility ($1200\,cm^2/Vs$) [10, 11], high critical electric field (2.5–2.8 MV/cm) [16], and wide bandgap (3.26 eV) [8]. Hereafter, the term "SiC" represents 4H-SiC otherwise specified.

In addition to the attractive material properties, SiC has many advantages from a technical point of view. It is a good example to describe the superiority of SiC that doping density in both n- and p-type SiC can be controlled in a vast range (10^{14}–$10^{19}\,cm^{-3}$) through epitaxial growth [18]. Mature ion implantation technology also enables the formation of n- and p-type SiC regions with a very high doping density ($> 10^{20}\,cm^{-3}$) [19–23]. The wide-range controllability of doping density, which is hardly achieved in other WBG semiconductors, is an exceptional feature to help design and fabricate various SiC electronic devices.

The author explains how SiC devices contribute to developing power electronics and high-temperature operational ICs in the following sections.

Table 1.1: Major material properties of Si and various polytypes of SiC (data obtained at room temperature) [5–17].

Property	Si	3C-SiC	4H-SiC	6H-SiC
Bandgap (eV)	1.12	2.36	3.26	3.02
Electron Mobility (cm^2/Vs)	1450	~ 1000	1200 ($\parallel c$) 1000 ($\perp c$)	100 ($\parallel c$) 450 ($\perp c$)
Hole Mobility (cm^2/Vs)	500	100	85 ($\parallel c$) 95 ($\perp c$)	100
Electron Saturated Drift Velocity (cm/s)	1×10^7	2×10^7	2.2×10^7	1.9×10^7
Critical Electric Field (MV/cm) *at $1 \times 10^{16}\,cm^{-3}$	0.4	1.4	2.5 ($\parallel c$) 2.2 ($\perp c$)	2.8 ($\parallel c$) 1.7 ($\perp c$)
Relative Dielectric Constant	11.9	9.72	10.3 ($\parallel c$) 9.76 ($\perp c$)	10.0 ($\parallel c$) 9.66 ($\perp c$)

1.2.2 Applications in Power Electronics

Figure 1.1 depicts a typical DC–AC conversion circuit (inverter) for three-phase motor control. The electrical power conversion is performed with a pair of a transistor (switching device) and a diode (rectifier), which are the fundamental components of power semiconductor devices. Schematic illustrations of the current–voltage (I–V) characteristics of (a) rectifiers and (b) switching devices are shown in Fig. 1.2. Ideally, power devices are expected to have no voltage drop (no resistance, $0\,\Omega$) during the "ON"-state operation and no leakage current (infinite resistance, $\infty\,\Omega$) even with any high voltage applied in the "OFF" state. However, real devices inevitably exhibit a finite ON-state resistance ($R_{\rm ON}$) and, in the OFF state, have a finite leakage current and breakdown voltage ($V_{\rm BD}$) at which a very sharp current increase occurs. These non-ideal characteristics are the main cause of the static loss in power devices. Regarding the switching operation, furthermore, it takes a finite delay in the transition between ON and OFF states, resulting in switching loss. Consequently, the primary requirement for power devices is to simultaneously achieve a low on-resistance, a negligible leakage current, and fast switching under a given blocking voltage. From these points of view, SiC power devices can exhibit significant advantages compared to Si-based devices.

Figure 1.3(a) schematically illustrates the electric field distribution in SiC and Si devices containing a one-sided abrupt junction (e.g., Schottky barrier diodes; SBDs) designed to have the same blocking voltage. Under the OFF-state operation with a reverse bias applied, a depletion region extends toward a voltage-blocking layer, and junction breakdown occurs when the maximum electric field at the junction reaches the critical electric field ($F_{\rm BD}$). Since the area of the triangular-shaped electric field distribution corresponds to the blocking voltage, a thicker layer with a lower doping density (showing a milder slope in the plot) has to be prepared to obtain a higher $V_{\rm BD}$. This fact clearly shows the trade-off relationship between $R_{\rm ON}$ and $V_{\rm BD}$, that is, $R_{\rm ON}$ is significantly increased for power devices requiring a higher $V_{\rm BD}$. Figure 1.3(b) shows $R_{\rm ON}$–$V_{\rm BD}$ plots for Si and SiC power devices calculated with the formula [24],

$$R_{\rm ON} = \frac{4V_{\rm BD}^4}{\eta\varepsilon_{\rm s}\mu F_{\rm BD}^3}, \tag{1.1}$$

where η is the activation ratio of dopants (typically $\eta = 0.85$–1.00), and $\varepsilon_{\rm s}$ and μ are the dielectric constant and the mobility of the semiconductor, respectively. Since SiC has about ten times higher $F_{\rm BD}$ than that of Si, it is possible to make the drift layer thickness about ten times thinner and the doping density 100 times higher when designing a device with the same $V_{\rm BD}$, as indicated in Fig. 1.3(a). As a result, SiC power devices can achieve a significantly low $R_{\rm ON}$ (about 1/500 times lower than that for Si devices at a given $V_{\rm BD}$ [25, 26]), leading to a considerable static loss reduction.

Another important advantage of SiC power devices is fast switching by adopting a unipolar operation. Figure 1.4 indicates the major territories of unipolar and bipolar power devices for Si and SiC in terms of the rated blocking voltage [24]. Regarding the medium-

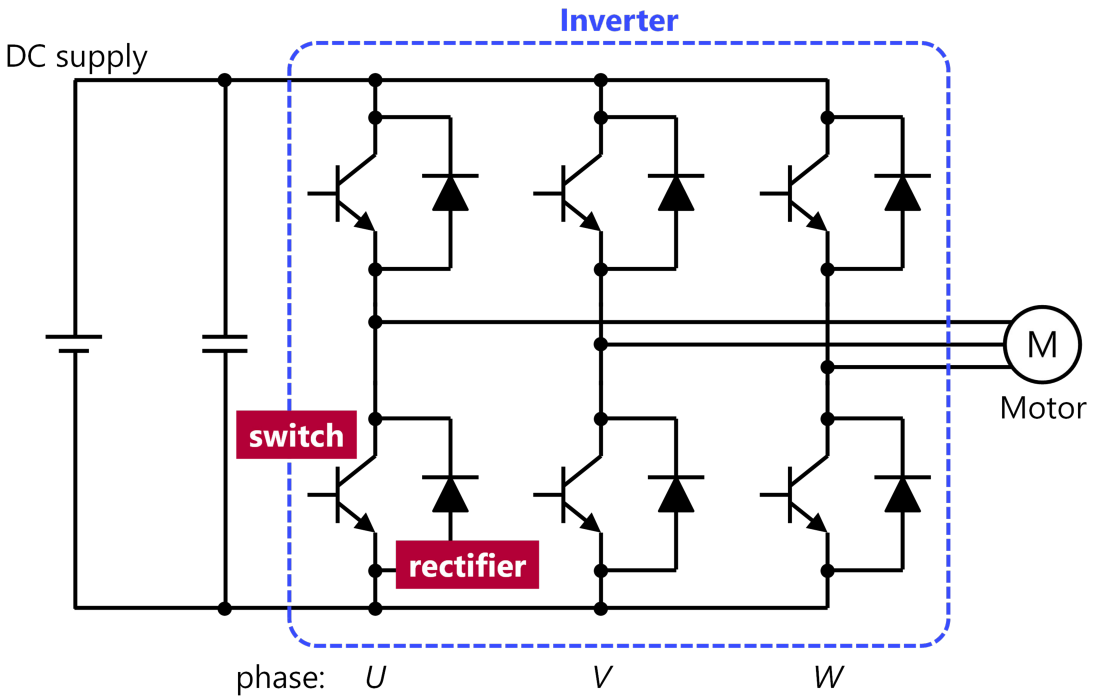

Figure 1.1: Typical DC–AC conversion circuit (inverter) for three-phase motor control.

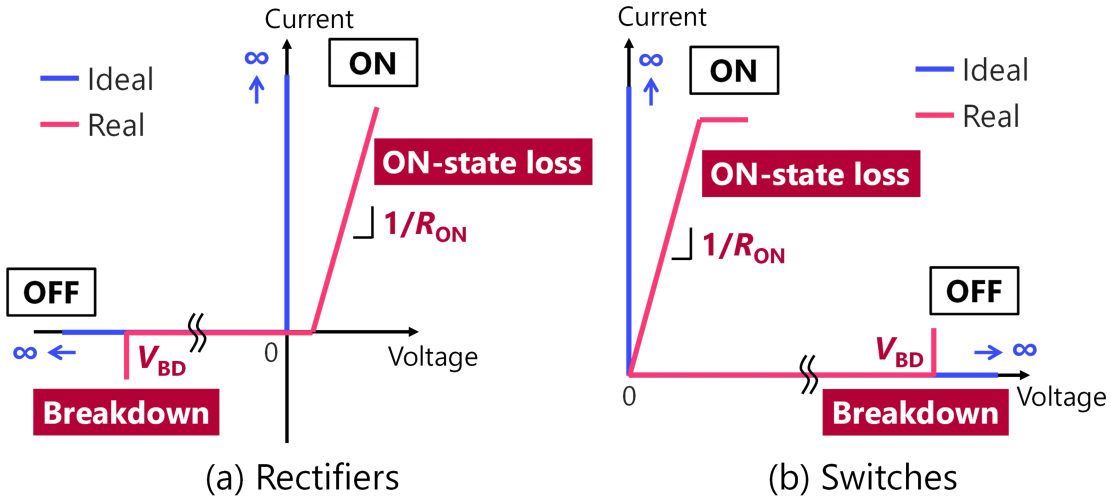

Figure 1.2: Current–voltage characteristics of (a) power diodes and (b) power switching devices in ideal and real cases.

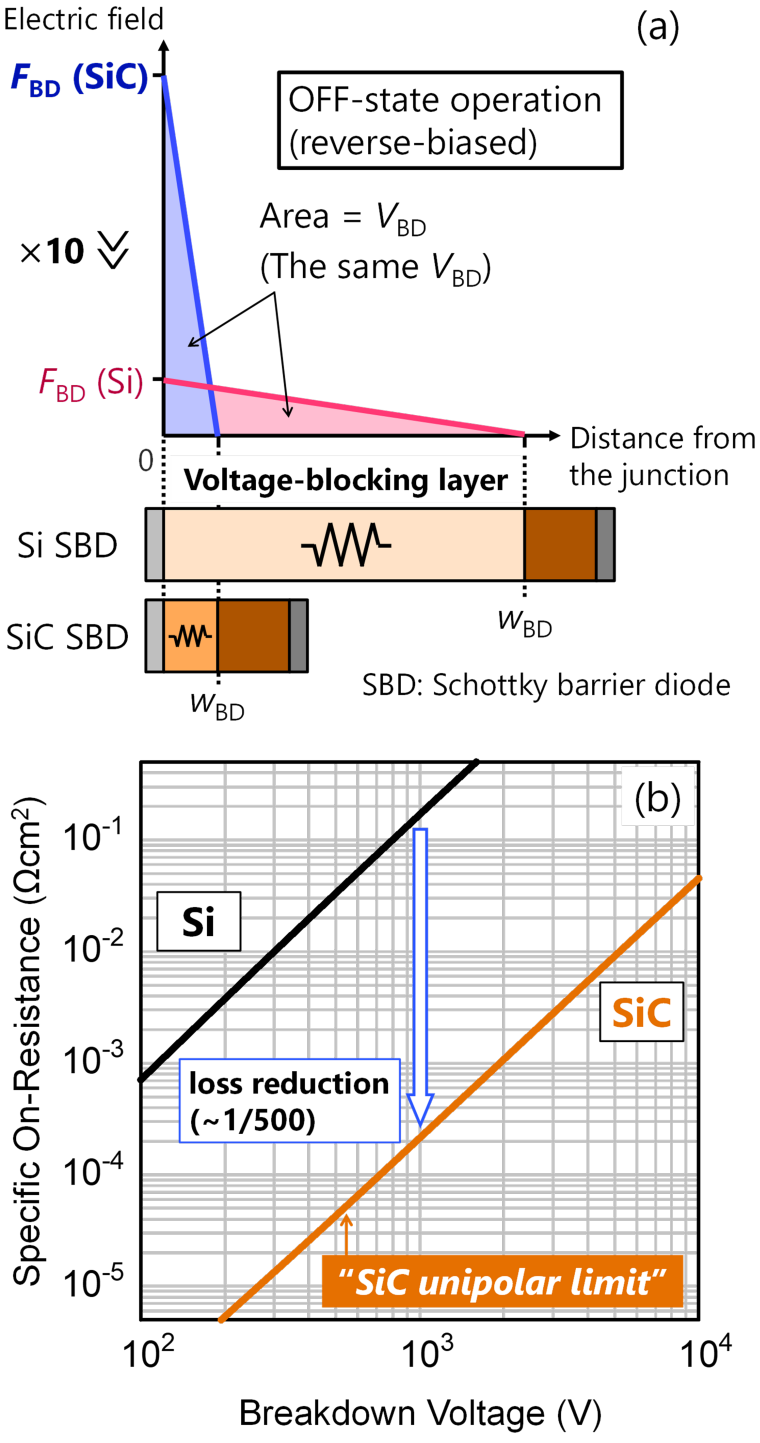

Figure 1.3: (a) Electric field distribution under a reverse-biased condition (OFF-state operation) in Si and SiC Schottky barrier diodes (SBDs) with the same blocking voltage. (b) Trade-off relationship between the specific on-resistance of the drift layer and breakdown voltage in Si and 4H-SiC(0001) unipolar devices having a non-punch-through (NPT) structure.

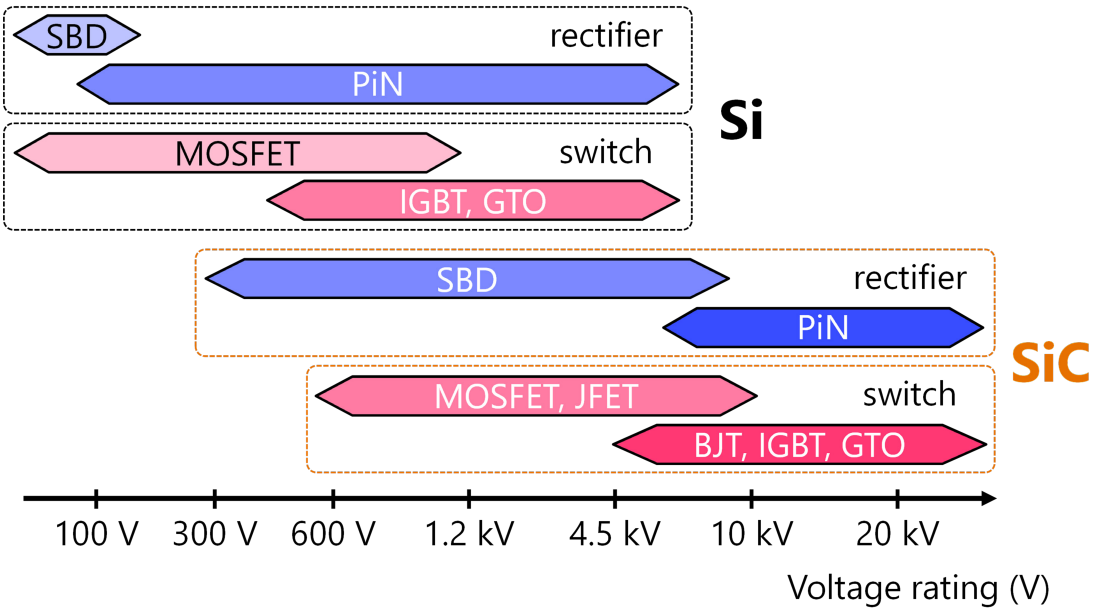

Figure 1.4: Major territories of unipolar and bipolar power devices for Si and SiC as a function of the rated blocking voltage [24].

to high-voltage applications (e.g., V_{BD} in several kV), Si-based bipolar devices such as PiN diodes and insulated gate bipolar transistors (IGBTs) have been employed because they can effectively reduce R_{ON} thanks to the conductivity modulation caused by minority carrier injection [27] and overcome the *unipolar limit* given by Eq. (1.1). However, it takes a long time to eject minority carriers from the voltage-blocking layer, and thus, these bipolar devices inherently exhibit a slower switching speed. On the other hand, SiC can ensure a sufficiently low R_{ON} in these V_{BD} ranges even with unipolar devices such as SBDs and metal-oxide-semiconductor field-effect transistors (MOSFETs), leading to considerable loss reduction during switching operation.

Because of these superiorities, SiC has received much attention as a semiconductor material suitable for high-voltage (several kV), low-loss, and fast-switching power devices [27–32]. Decades of intensive studies on crystal growth, material properties, and device processing of SiC have allowed mass production and commercialization of SiC unipolar power devices (SBDs and MOSFETs), achieving improved energy efficiency in real electronic systems [33–35]. Besides, bipolar operation in SiC PiN diodes, IGBTs, bipolar junction transistors (BJTs), and gate-turn-off (GTO) thyristors will be promising in ultra-high-voltage devices ($> 10\,\mathrm{kV}$), and rapid progress in crucial technologies for putting them into practical applications is ongoing [30, 32, 36, 37].

1.2.3 Applications in High-Temperature Electronics

Figure 1.5 plots the temperature dependence of the intrinsic carrier density (n_{i}) in Si and SiC calculated based on the formula [5],

$$n_{\mathrm{i}} = \sqrt{N_{\mathrm{C}} N_{\mathrm{V}}} \exp\left(-\frac{E_{\mathrm{g}}}{2k_{\mathrm{B}}T}\right), \tag{1.2}$$

where N_{C} and N_{V} are the effective densities of states in conduction and valence bands, respectively, E_{g} is the bandgap, k_{B} is the Boltzmann constant, and T is the absolute temperature. In LSI circuits containing a huge number of transistors, electrical isolation between a device and its neighbors is usually guaranteed by the rectification of p-n junctions. Since the reverse leakage current in p-n junctions is proportional to n_{i}, an increased n_{i} and leakage current at an elevated temperature lead to isolation failure and undesirable operation. Due to the relatively small bandgap of Si ($E_{\mathrm{g}} = 1.12\,\mathrm{eV}$), n_{i} becomes comparable to the intentional doping level ($\sim 10^{15}\,\mathrm{cm}^{-3}$) when the ambient temperature exceeds about 200°C, leading to an unacceptably large leakage current. Hence, the maximum operational temperature is limited to about 200°C in the currently available Si-based ICs consisting of CMOS devices. Although the operating temperature can be improved by adopting silicon-on-insulator (SOI) substrates, in which neighbor devices are isolated by trench etching of a thin Si layer ($< 1\,\mu\mathrm{m}$), the maximum operation temperature is still limited up to 250–300°C [38, 39]. Thanks to the wide bandgap of SiC ($E_{\mathrm{g}} = 3.26\,\mathrm{eV}$), on the other hand, n_{i}

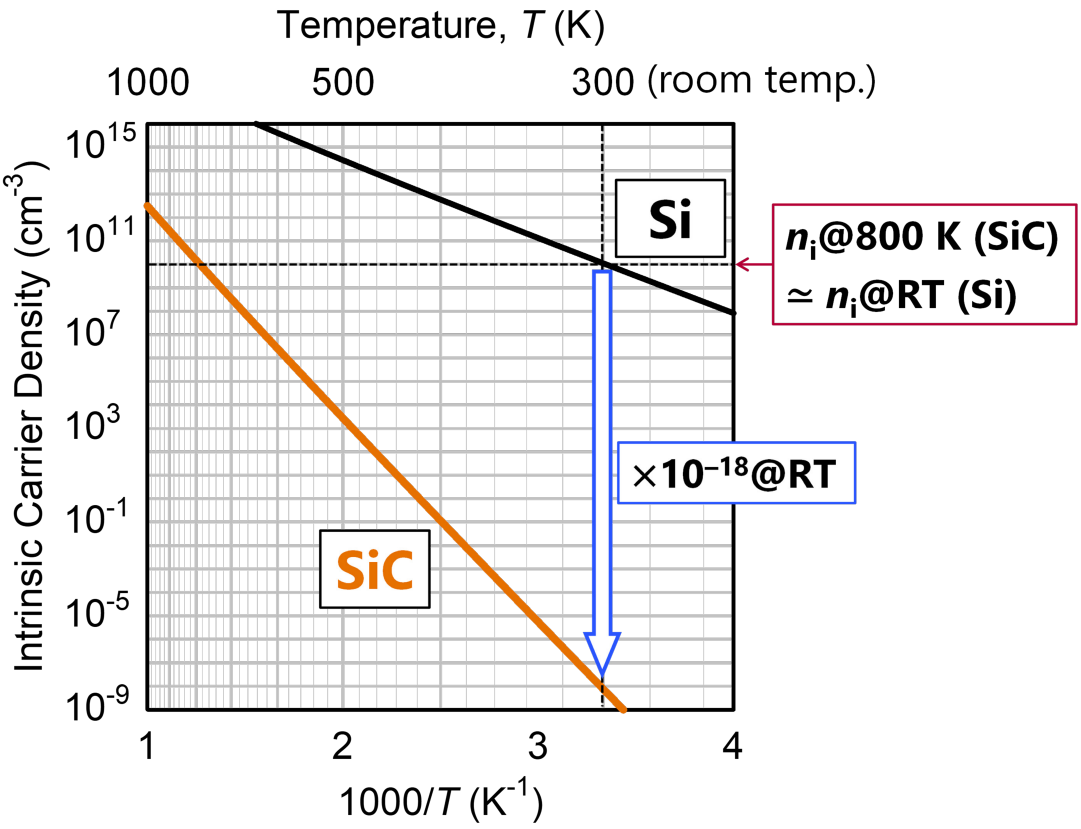

Figure 1.5: Intrinsic carrier density in Si and SiC as a function of the reciprocal temperature.

in SiC is extremely low like $10^{-8}\,\mathrm{cm}^{-3}$ at room temperature, which is 18 orders of magnitude lower than that in Si ($10^{10}\,\mathrm{cm}^{-3}$). This fact clearly shows the applicability of SiC for high-temperature operational IC applications.

Figure 1.6 describes the major high-temperature electronics applications plotted against the ambient temperature [3, 40, 41]. High-temperature operational ICs have a wide variety of potential applications, such as combustion furnaces, airplane turbine engines, and aerospace exploration, as well as deep-well drilling. Regarding SiC-based high-temperature electronics, ICs composed of SiC MOSFETs [42, 43], BJTs [44–46], and junction-field effect transistors (JFETs) [47–49] operational at a high temperature ($> 300°\mathrm{C}$) have been demonstrated. It is notable that because of the high atomic replacement threshold energy and radiation ionization energy [50, 51], SiC is an attractive material also in radiation-hardened device applications (e.g., aerospace, nuclear plant, and so on), for which there are several reports on radiation-robust device operation [52, 53]. Consequently, SiC will play a vital role in this new, rapidly developing field of high-temperature and harsh-environment electronics [40, 54–57].

1.3 Metal/SiC Junctions

A metal/semiconductor junction is one of the most fundamental building blocks in all semiconductor devices introduced above. There are two types of the junction; one is a Schottky contact, which exhibits rectifying I–V characteristics, and the other is an ohmic contact with a linear I–V relationship, as shown in Fig. 1.7. Energy band diagrams for these contacts near the metal/n-type semiconductor junction are also illustrated in Fig. 1.7. In an ideal situation, these two contacts are classified based on the difference between the work functions of metal (ϕ_m) and semiconductor (ϕ_s); in the case of an n-type semiconductor, Schottky contacts are formed when ϕ_m is higher than ϕ_s, whereas the relationship of $\phi_\mathrm{m} < \phi_\mathrm{s}$ leads to the ohmic contact formation. Note that the relationship between ϕ_m and ϕ_s to form each contact is just the opposite in the case of a p-type conductivity. A Schottky contact is a key component in SBDs and metal-semiconductor field effect transistors (MESFETs). Besides, any semiconductor device essentially requires a low-resistance and stable ohmic contact to be connected to an external circuit with a minimum voltage drop at the contact. The following section introduces the features and research status of the two types of metal/SiC junctions.

1.3.1 Schottky and Ohmic Contacts on SiC

Figure 1.8 depicts the energy band diagram of SiC and several metals. Because of the relatively low electron affinity ($\chi_\mathrm{s} = 3.8\,\mathrm{eV}$) [58] and wide bandgap of SiC ($E_\mathrm{g} = 3.26\,\mathrm{eV}$), Schottky contacts are basically formed when depositing electrode metals typically used in semiconductor devices that possess ϕ_m of 4–6 eV (e.g., Ti, Ni, W, Pt, and so on) [59].

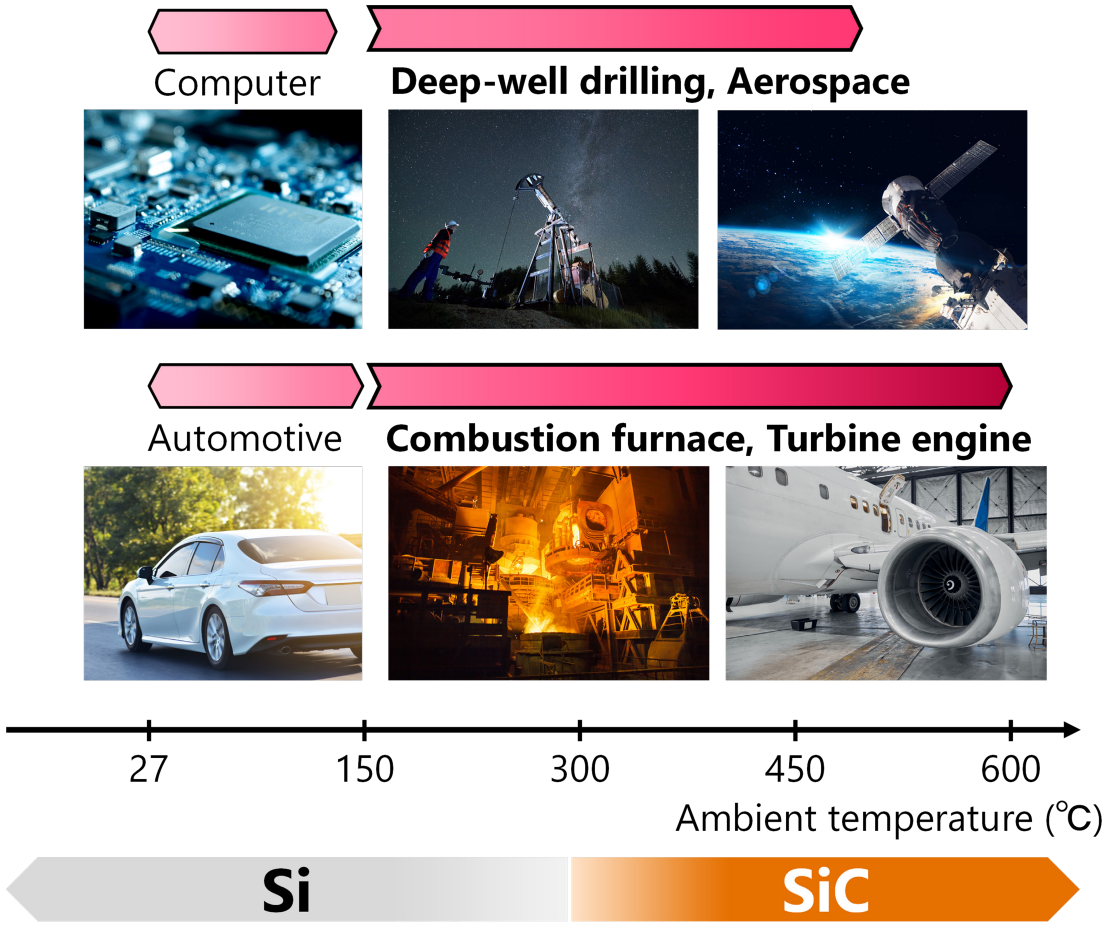

Figure 1.6: Major application fields of high-temperature operational ICs as a function of the ambient temperature (all the pictures were taken from Adobe Stock with the Standard License).

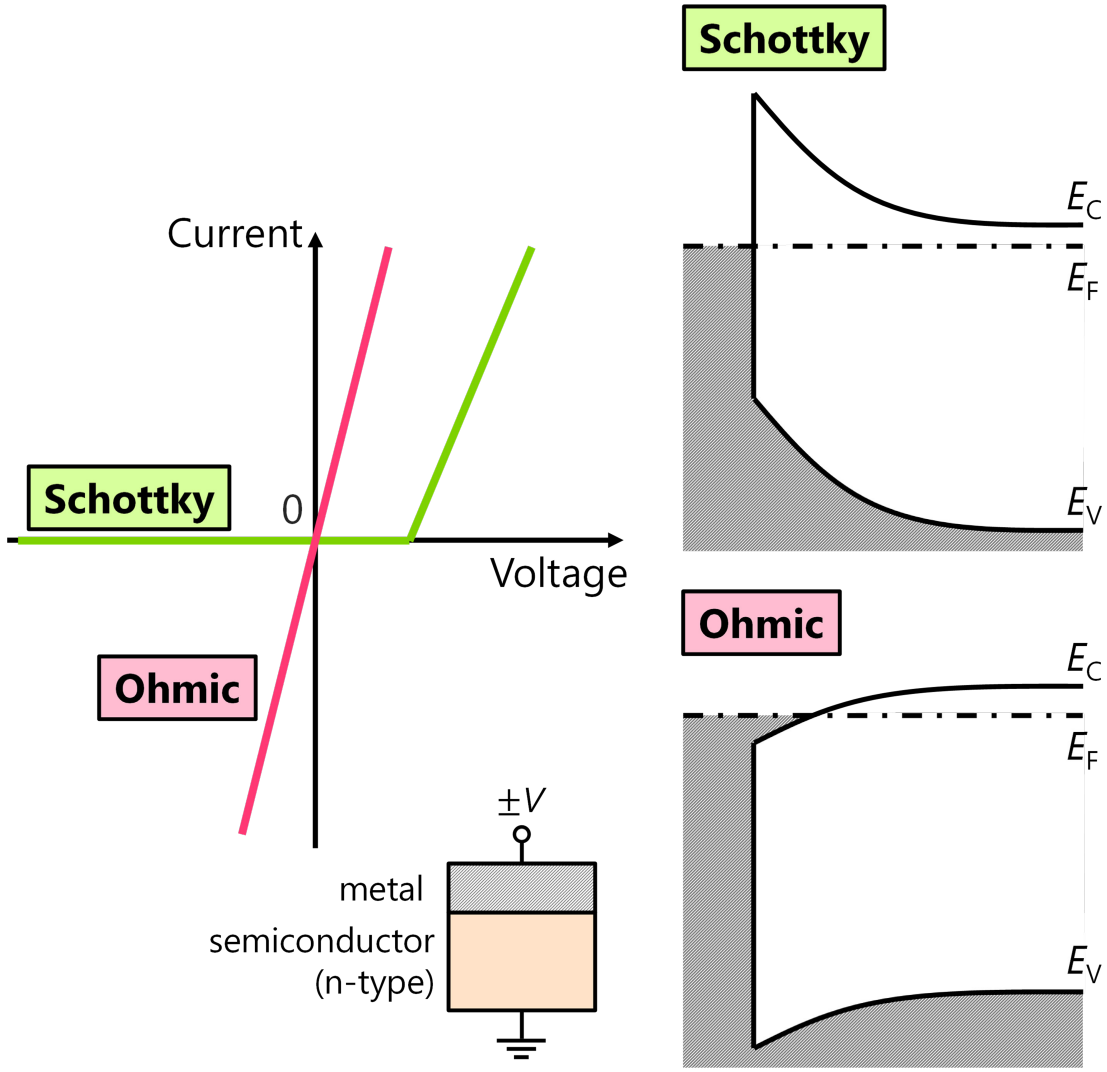

Figure 1.7: Typical current–voltage characteristics of Schottky and ohmic contacts and energy band diagrams representing each contact.

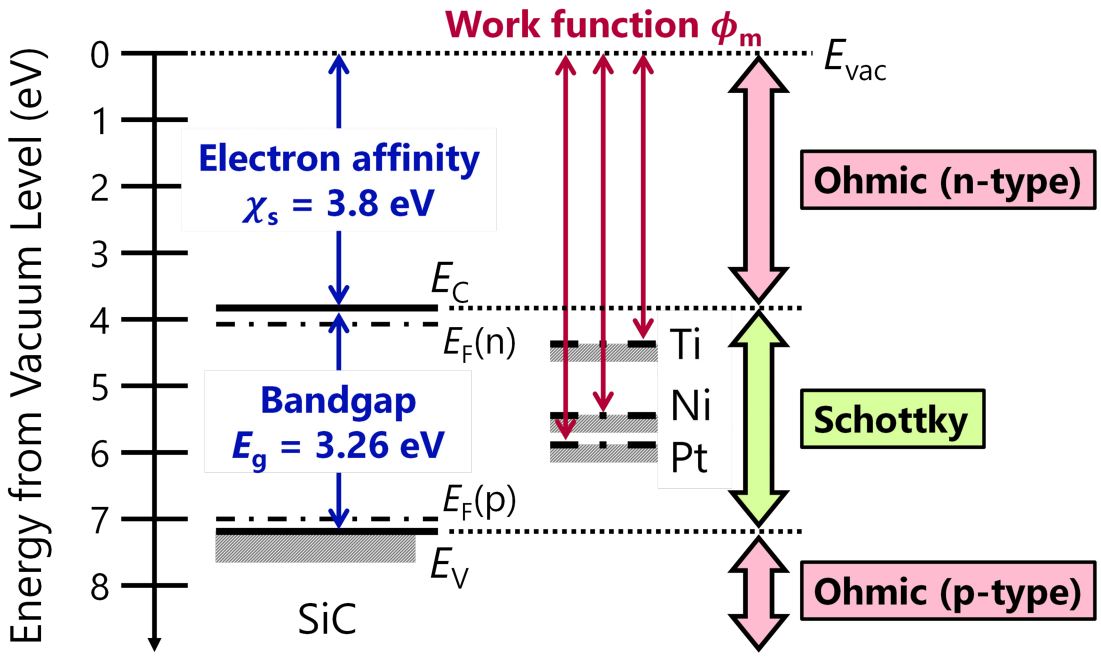

Figure 1.8: Energy band diagram of SiC and several metals typically used in semiconductor devices.

Therefore, it is relatively easy to obtain good Schottky contacts on SiC. On the other hand, the formation of ideal ohmic contacts is difficult, which is a common challenge that most WBG semiconductor materials face.

SiC Schottky Contacts

The invention of novel techniques for SiC bulk growth (*modified Lely method* or *seeded sublimation method*) in 1978–1981 [60, 61] and epitaxial growth (*step-controlled epitaxy*) in 1987 [62] accelerated the research and development of SiC devices. Following the pioneering research, the adoption of SiC to power electronics was proposed in 1989 [63], and SiC Schottky contacts began to be intensively studied in the early 1990s, aiming at high-voltage rectifiers. The successful fabrication and operation of a 400 V 6H-SiC SBD were reported in 1992 [64], and a 1 kV-class 6H-SiC SBD with a low R_{ON} and 400°C rectification was demonstrated in 1993 [65]. Then, in 1994–1995, the world-first high-voltage SiC SBD ($>$ 1 kV) with a further low R_{ON} by adopting 4H-polytype was demonstrated [28, 66], which is well beyond the Si SBD's territory and even superior to Si PiN diodes in terms of switching loss reduction. This demonstration was a significant milestone that triggered scientists and engineers in the field of power electronics to recognize the outstanding potential of 4H-SiC as a power semiconductor material.

On the other hand, SiC SBDs had a serious problem related to the unacceptably large leakage current [67, 68] that was much larger than that in conventional Si SBDs described by the thermionic emission (TE) transport including image force lowering [69]. Although the origin of this large leakage current had been unclear, the underlying physics to explain this phenomenon was clarified several years later. Since it is possible to apply a very high electric field (MV/cm order) to SiC, a Schottky barrier becomes very thin despite the low doping density in the voltage-blocking layer, enabling carriers to tunnel through the barrier [70, 71]. Finally, it turned out that the reverse leakage current in high-voltage SiC SBDs can be well described by the thermionic field emission (TFE) model [72, 73], which represents the tunneling process of thermally excited carriers [74, 75]. Interestingly, the reverse TFE current is commonly observed in power SBDs fabricated with other WBG semiconductors like GaN and Ga_2O_3 [76–78]. This discovery provided a guideline that the leakage current can be reduced by suppressing the interface electric field, leading to the proposal and demonstration of a junction barrier Schottky (JBS) structure [79, 80]. After the structure and process optimization, high-voltage SiC SBDs became commercially available in 2001, and now they are implemented in a wide variety of power conversion systems, achieving considerable loss reduction [6].

SiC Ohmic Contacts

A primary requirement for ohmic contacts is to ensure the bi-directional current flow with a sufficiently low contact resistivity (i.e., negligibly small voltage drop at the contact).

Here, a contact resistivity (ρ_c, unit: Ωcm^2), which is defined as the voltage drop under a given current density flowing, is an indicator that represents the quality of ohmic contacts. Regarding power devices, ρ_c of about $10^{-6}\,\Omega cm^2$ is usually required, and further low ρ_c of 10^{-7}–$10^{-8}\,\Omega cm^2$ is essential in IC applications. In the case of SiC, however, obtaining such a low ρ_c is inherently difficult because the preferable relationship between ϕ_m and ϕ_s for ideal ohmic contacts is hardly satisfied just by depositing typical electrode metals, as mentioned above. As a result, performing high-temperature sintering ($\sim 1000°C$) after the electrode metal deposition on heavily-doped SiC ($> 10^{19}\,cm^{-3}$) has become the standard process to obtain low-resistance SiC ohmic contacts [81–84].

The history of research on SiC ohmic contacts also dates back to the early 1990s, and the sintered (alloyed) ohmic contacts on SiC have been extensively studied so far, mainly from the standpoint of structural analyses. Ni-based contacts annealed at 900–1000°C are widely adopted as ohmic electrodes for n-type SiC because they can achieve a low ρ_c of about $10^{-6}\,\Omega cm^2$ [85–88]. Rutherford backscattering spectrometry (RBS) and Auger electron spectroscopy (AES) revealed that Ni and SiC react to form nickel silicide (mainly Ni_2Si) during the anneal, whereas nickel carbide is not formed and residual carbon atoms are accumulated near the interface [86]. As for p-type SiC, an electrode stack consisting of Al/Ti sintered at about 1000°C is commonly utilized for ohmic contact formation with ρ_c below $10^{-5}\,\Omega cm^2$ [89–91]. Transmission electron microscopy (TEM) observation showed the formation of Ti_3SiC_2 as the main phase resulting from the interfacial reaction caused by high-temperature sintering [92, 93].

In contrast to the relatively mature process and physical understanding of Schottky contacts formed on lightly-doped SiC, however, there remain several critical issues regarding SiC ohmic contacts that hinder further improvement in the device performance and cost reduction in the device fabrication, which are described in the next section.

1.3.2 Key Issues for Ohmic Contact Formation in SiC Devices

The first problem is a poor understanding of the mechanism of ohmic contact formation through the high-temperature process. Despite continuous efforts to reveal the formation mechanism based on the structural analyses of the alloyed metal/SiC interface, the correlation between interfacial reactions and electrical characteristics is still not quantitatively understood. Despite a high Schottky barrier ($> 1.5\,eV$) at non-sintered (non-alloyed) Ni/n-type SiC and Ti/p-type SiC interfaces, for instance, Ni- or Ti-based ohmic contacts on n- or p-type SiC, respectively, can achieve a low ρ_c and are practically utilized, as mentioned above. Regarding the Ni-based alloyed ohmic contacts on n-type SiC, although Ni_2Si formation already occurs at 600°C, ohmic behavior is not ensured with such a low-temperature treatment [82, 94, 95]. Besides, a non-sintered Ni_2Si/SiC interface formed by directly depositing the silicide shows Schottky characteristics [6]. A sputtered Ti_3SiC_2 film does not provide an ohmic characteristic for p-type SiC [96], as is the case for n-type SiC. Conse-

quently, it is still unclear what critically contributes to the ohmic contact formation in the high-temperature processes, and thus, there exist very few guidelines for the design and formation of low-resistance ohmic contacts on SiC.

The high-temperature sintering for the ohmic contact formation also causes several negative impacts on the performance and reliability of devices [97]. Figure 1.9 depicts a schematic illustration of a typical SiC trench MOSFET and summarizes several drawbacks related to the high-temperature process for ohmic contact formation. Severe surface roughening caused by interfacial reactions and segregation of melted metal at a high temperature [98] is a critical issue that makes wire bonding to the electrode difficult. It was pointed out that post-metallization annealing at a high temperature can degrade the quality of a SiO_2/SiC interface and MOSFET performance [99].

The ρ_c value obtained with the high-temperature treatment is insufficient from several points of view. With the currently available process, ρ_c is typically limited down to about $1 \times 10^{-6}\,\Omega\mathrm{cm}^2$, which is not sufficiently low when SiC devices are further down-sized to be employed in IC applications. Because of a severe unbalance of ρ_c between n- and p-type ohmic contacts (i.e., much higher ρ_c for p-type SiC), besides, an optimum contact material and process for simultaneous ohmic contacts on n- and p-type SiC that are useful to make the source and body regions in MOSFETs simultaneously grounded have not yet been established.

From these points of view, a novel fabrication process for SiC ohmic contacts that can achieve a very low ρ_c ($< 10^{-6}\,\Omega\mathrm{cm}^2$) with a low-temperature treatment ($<$ 500–600°C) is strongly demanded. Although several groups have made trials to achieve a low ρ_c without performing the high-temperature sintering [100–103], there exists no established low-temperature process for the ohmic contact formation, and thus, such processes have not yet been adopted in the production of SiC devices. In order to construct a design guideline for the low-temperature formation of ohmic contacts, understanding the fundamental electrical characteristics at metal/heavily-doped SiC non-alloyed interfaces is indispensable. Since a non-alloyed contact is equivalent to a "Schottky contact" in the case of SiC, as mentioned above, the main focus should be on the characterization of heavily-doped SiC Schottky contacts. Although intense research has been dedicated to SiC Schottky contacts until now, they have mainly dealt with metal/lightly-doped SiC structures because high-voltage SBDs are usually fabricated with a lightly-doped semiconductor. Therefore, no reports investigated the interface characteristics of Schottky (non-alloyed) contacts formed on heavily-doped SiC ($> 10^{19}\,\mathrm{cm}^{-3}$).

1.4 Purpose and Outline of This Thesis

Standing on the above background, in this study, the author put the purpose on proposing a design guideline for low-resistance non-alloyed ohmic contacts on n-type SiC based on a

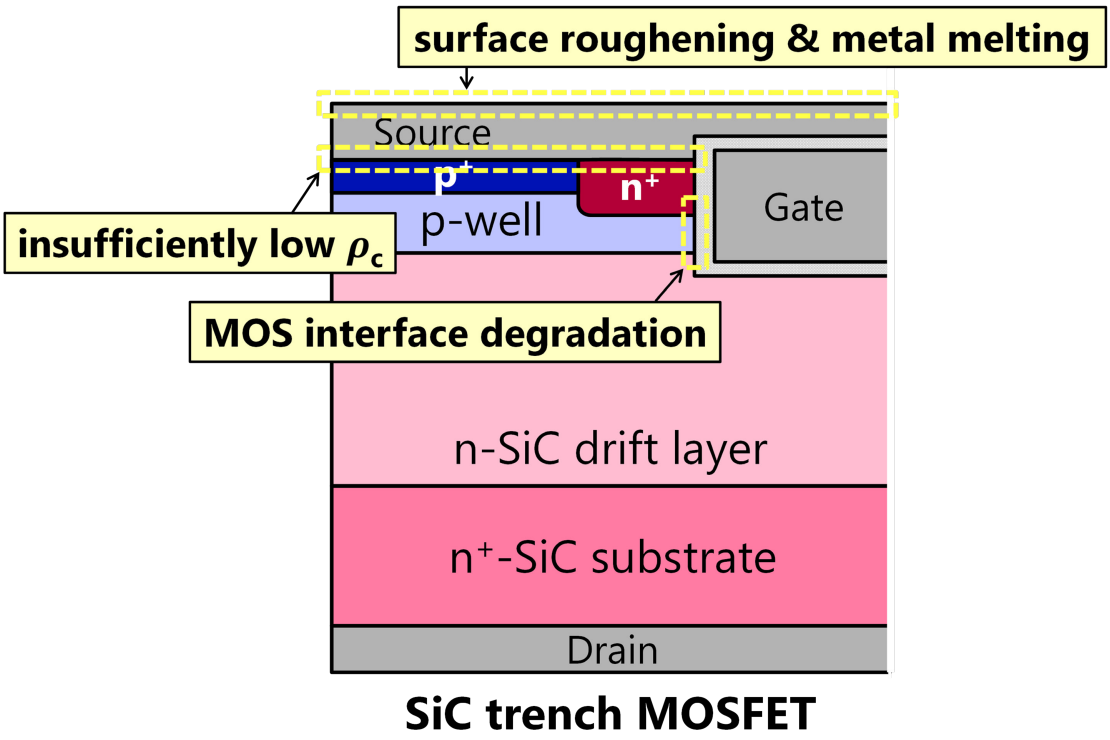

Figure 1.9: Schematic illustration of a SiC trench MOSFET and several drawbacks of ohmic contact formation process with high-temperature sintering.

physical understanding of metal/heavily-doped SiC Schottky interfaces.

In Chapter 2, the author fabricates vertical SBD structures using heavily-doped n-type SiC and systematically investigates the Schottky barrier height at metal/heavily-doped SiC interfaces, using three different techniques. The doping density dependence of the barrier height at metal/SiC interfaces is quantitatively discussed, and a change in the dominant carrier transport mechanism ascribed to electron tunneling in heavily-doped SiC SBDs is indicated. The relationship between the barrier height and metal work function is also investigated, employing various Schottky electrode metals.

In Chapter 3, the tunneling current in a Schottky structure formed on a heavily-doped n-type SiC epitaxial layer is numerically analyzed based on the direct tunneling (DT) model, which comprehensively describes the thermionic field emission (TFE) and field emission (FE) transport. By comparing the experimental and calculated I–V characteristics in a wide range of doping density and applied voltage, the dominant carrier transport mechanism in heavily-doped SiC SBDs is specified. A change in the dominant tunneling process (TFE or FE) depending on the electric field is also discussed in detail.

In Chapter 4, high-dose phosphorus ion (P^+) implantation is performed in the formation of heavily-doped n-type SiC Schottky structures, and differences in electrical characteristics, especially carrier transport mechanism, between the cases of epitaxial and ion-implanted layers are investigated. Through the careful analysis of the net donor density, Schottky barrier height, and I–V characteristics in heavily P^+-implanted SiC Schottky structures, the contribution of trap-assisted tunneling (TAT) is indicated. The deep level that dominantly influences the carrier transport at metal/P^+-implanted SiC interfaces is speculated by performing the numerical calculation of the TAT current with various trap levels assumed.

In Chapter 5, the contact resistivity at non-alloyed contacts formed on heavily phosphorus ion implanted n-type SiC is characterized as a function of the donor density and barrier height. The experimental characterization and numerical analysis of the contact resistivity present a physical model to predict the contact resistivity, in which the contributions of the DT and TAT transport are carefully considered. Furthermore, the author proposes a design guideline for low-resistance non-alloyed ohmic contacts on SiC, regarding the barrier height, doping density, and how to form the contact region.

Finally, the author summarizes this thesis and gives future prospects in Chapter 6.

References

[1] W. E. Newell, *1973 IEEE Power Electronics Specialists Conference* (1973), p. 6.

[2] A. F. Veneruso, *IEEE Circuits & Systems Magazine* **1**, 11 (1979).

[3] P. L. Dreike, D. M. Fleetwood, D. B. King, D. C. Sprauer, and T. E. Zipperian, *IEEE Trans. Compon. Packag. Manuf. Technol. Part A* **17**, 594 (1994).

[4] G. A. Slack, *J. Appl. Phys.* **35**, 3460 (1964).

[5] S. M. Sze, Y. Li, and K. K. Ng, *Physics of Semiconductor Devices* (John Wiley & Sons, 4th edition, 2021).

[6] T. Kimoto and J. A. Cooper, *Fundamentals of Silicon Carbide Technology: Growth, Characterization, Devices and Applications* (John Wiley & Sons, 2014).

[7] S. Adachi, *Properties of Group-IV, III-V and II-VI Semiconductors* (John Wiley & Sons, 2007).

[8] W. J. Choyke and R. P. Devaty, Optical properties of SiC: 1997–2002, *Silicon Carbide: Recent Major Advances* (eds. W. J. Choyke, H. Matsunami, and G. Pensl), (Springer, Berlin Heidelberg, 2004), p. 413.

[9] W. J. Schaffer, G. H. Negley, K. G. Irvine, and J. W. Palmour, *MRS Online Proceedings Library (OPL)* **339**, 595 (1994).

[10] R. Ishikawa, M. Hara, H. Tanaka, M. Kaneko, and T. Kimoto, *Appl. Phys. Express* **14**, 061005 (2021).

[11] R. Ishikawa, H. Tanaka, M. Kaneko, and T. Kimoto, *Phys. Status Solidi B* **260**, 2300275 (2023).

[12] H. Matsuura, M. Komeda, S. Kagamihara, H. Iwata, R. Ishihara, T. Hatakeyama, T. Watanabe, K. Kojima, T. Shinohe, and K. Arai, *J. Appl. Phys.* **96**, 2708 (2004).

[13] R. Ishikawa, H. Tanaka, M. Kaneko, and T. Kimoto, *International Conference on Silicon Carbide and Related Materials 2022* (Davos, 2022), Fr-2-A.3.

[14] I. A. Khan and J. A. Cooper, *IEEE Trans. Electron Devices* **47**, 269 (2000).

[15] A. O. Konstantinov, Q. Wahab, N. Nordell, and U. Lindefelt, *Appl. Phys. Lett.* **71**, 90 (1997).

[16] H. Niwa, J. Suda, and T. Kimoto, *IEEE Trans. Electron Devices* **62**, 3326 (2015).

[17] D. Stefanakis, X. Chi, T. Maeda, M. Kaneko, and T. Kimoto, *IEEE Trans. Electron Devices* **67**, 3740 (2020).

[18] H. Matsunami and T. Kimoto, *Mater. Sci. Eng. R Rep.* **20**, 125 (1997).

[19] M. A. Capano, R. Santhakumar, R. Venugopal, M. R. Melloch, and J. A. Cooper, *J. Electron. Mater.* **29**, 210 (2000).

[20] M. Laube, F. Schmid, G. Pensl, G. Wagner, M. Linnarsson, and M. Maier, *J. Appl. Phys.* **92**, 549 (2002).

[21] Y. Negoro, K. Katsumoto, T. Kimoto, and H. Matsunami, *J. Appl. Phys.* **96**, 224 (2004).

[22] J. M. Bluet, J. Pernot, J. Camassel, S. Contreras, J. L. Robert, J. F. Michaud, and T. Billon, *J. Appl. Phys.* **88**, 1971 (2000).

[23] Y. Negoro, T. Kimoto, H. Matsunami, F. Schmid, and G. Pensl, *J. Appl. Phys.* **96**, 4916 (2004).

[24] T. Kimoto, *Jpn. J. Appl. Phys.* **54**, 040103 (2015).

[25] T. Kimoto, *Jpn. J. Appl. Phys.* **58**, 018002 (2018).

[26] T. Kimoto, M. Kaneko, K. Tachiki, K. Ito, R. Ishikawa, X. Chi, D. Stefanakis, T. Kobayashi, and H. Tanaka, *Tech. Digest of 2021 IEEE International Electron Devices Meeting (IEDM)* (2021), p. 36.1.1.

[27] B. J. Baliga, *Fundamentals of Power Semiconductor Devices* (Springer, 2008).

[28] A. Itoh, T. Kimoto, and H. Matsunami, *IEEE Electron Device Lett.* **16**, 280 (1995).

[29] J. A. Cooper and A. Agarwal, *Proc. IEEE* **90**, 956 (2002).

[30] T. Kimoto and H. Watanabe, *Appl. Phys. Express* **13**, 120101 (2020).

[31] J. A. Cooper and D. T. Morisette, *IEEE Electron Device Lett.* **41**, 892 (2020).

[32] T. Kimoto, *Proc. Jpn. Acad. Ser. B* **98**, 161 (2022).

[33] T. Nakamura, Y. Nakano, M. Aketa, R. Nakamura, S. Mitani, H. Sakairi, and Y. Yokotsuji, *Tech. Digest of 2011 International Electron Devices Meeting (IEDM)* (2011), p. 26.5.1.

[34] K. Hamada, S. Hino, N. Miura, H. Watanabe, S. Nakata, E. Suekawa, Y. Ebiike, M. Imaizumi, I. Umezaki, and S. Yamakawa, *Jpn. J. Appl. Phys.* **54**, 04DP07 (2015).

[35] X. She, A. Q. Huang, Ó. Lucía, and B. Ozpineci, *IEEE Trans. Ind. Electron.* **64**, 8193 (2017).

[36] T. Tamaki, G. G. Walden, Y. Sui, and J. A. Cooper, *IEEE Trans. Electron Devices* **55**, 1920 (2008).

[37] T. Kimoto and Y. Yonezawa, *Mater. Sci. Semicond. Process.* **78**, 43 (2018).

[38] D. Flandre, *Mater. Sci. Eng. B* **29**, 7 (1995).

[39] M. A. Huque, S. K. Islam, L. M. Tolbert, and B. J. Blalock, *IEEE Trans. Power Electron.* **27**, 4153 (2012).

[40] P. G. Neudeck, R. S. Okojie, and L.-Y. Chen, *Proc. IEEE* **90**, 1065 (2002).

[41] R. W. Johnson, J. L. Evans, P. Jacobsen, J. R. Thompson, and M. Christopher, *IEEE Trans. Electron. Packag. Manuf.* **27**, 164 (2004).

[42] S.-H. Ryu, K. T. Kornegay, J. A. Cooper, and M. R. Melloch, *IEEE Trans. Electron Devices* **45**, 45 (1998).

[43] N. Kuhns, L. Caley, A. Rahman, S. Ahmed, J. Di, H. A. Mantooth, A. M. Francis, and J. Holmes, *IEEE Trans. Device Mater. Reliab.* **16**, 105 (2016).

[44] J.-Y. Lee, S. Singh, and J. A. Cooper, *IEEE Trans. Electron Devices* **55**, 1946 (2008).

[45] S. Singh and J. A. Cooper, *IEEE Trans. Electron Devices* **58**, 1084 (2011).

[46] L. Lanni, R. Ghandi, B. G. Malm, C.-M. Zetterling, and M. Östling, *IEEE Trans. Electron Devices* **59**, 1076 (2012).

[47] P. G. Neudeck, S. L. Garverick, D. J. Spry, L.-Y. Chen, G. M. Beheim, M. J. Krasowski, and M. Mehregany, *Phys. Stat. Sol. A* **206**, 2329 (2009).

[48] P. Neudeck, D. Spry, M. Krasowski, L. Chen, N. Prokop, L. Greer, and C. Chang, *Tech. Digest of 2020 IEEE International Electron Devices Meeting (IEDM)* (2020), p. 27.2.1.

[49] M. Kaneko, M. Nakajima, Q. Jin, and T. Kimoto, *IEEE Electron Device Lett.* **43**, 997 (2022).

[50] A. L. Barry, B. Lehmann, D. Fritsch, and D. Braunig, *IEEE Trans. Nucl. Sci.* **38**, 1111 (1991).

[51] C. A. Klein, *J. Appl. Phys.* **39**, 2029 (1968).

[52] S. Kuroki, H. Nagatsuma, M. d. Silva, S. Ishikawa, T. Maeda, H. Sezaki, T. Kikkawa, T. Makino, T. Ohshima, M. Östling, and C. M. Zetterling, *Mater. Sci. Forum* **858**, 864 (2016).

[53] S. S. Suvanam, S.-I. Kuroki, L. Lanni, R. Hadayati, T. Ohshima, T. Makino, A. Hallen, and C.-M. Zetterling, *IEEE Trans. Nucl. Sci.* **64**, 852 (2017).

[54] J. B. Casady and R. W. Johnson, *Solid State Electron.* **39**, 1409 (1996).

[55] N. G. Wright and A. B. Horsfall, *J. Phys. D: Appl. Phys.* **40**, 6345 (2007).

[56] M. Shakir, S. Hou, R. Hedayati, B. G. Malm, M. Östling, and C.-M. Zetterling, *Electronics* **8**, 496 (2019).

[57] F. La Via, D. Alquier, F. Giannazzo, T. Kimoto, P. Neudeck, H. Ou, A. Roncaglia, S. E. Saddow, and S. Tudisco, *Micromachines* **14**, 1200 (2023).

[58] V. V. Afanasev, M. Bassler, G. Pensl, and M. Schulz, *Phys. Stat. Sol. A* **162**, 321 (1997).

[59] H. B. Michaelson, *J. Appl. Phys.* **48**, 4729 (1977).

[60] Y. M. Tairov and V. F. Tsvetkov, *J. Cryst. Growth* **43**, 209 (1978).

[61] Y. M. Tairov and V. F. Tsvetkov, *J. Cryst. Growth* **52**, 146 (1981).

[62] N. Kuroda, K. Shibahara, W. Yoo, S. Nishino, and H. Matsunami, *Extended Abstracts of the 1987 Conference on Solid State Devices and Materials* (1987), p. 227.

[63] B. J. Baliga, *IEEE Electron Device Lett.* **10**, 455 (1989).

[64] M. Bhatnagar, P. K. McLarty, and B. J. Baliga, *IEEE Electron Device Lett.* **13**, 501 (1992).

[65] T. Kimoto, T. Urushidani, S. Kobayashi, and H. Matsunami, *IEEE Electron Device Lett.* **14**, 548 (1993).

[66] A. Itoh, T. Kimoto, and H. Matsunami, *1995 Intemational Symposium on Power Semiconductor Devices & ICs (ISPSD)* (1995), p. 101.

[67] A. Itoh, T. Kimoto, and H. Matsunami, *IEEE Electron Device Lett.* **17**, 139 (1996).

[68] K. J. Schoen, J. P. Henning, J. M. Woodall, J. A. Cooper, and M. R. Melloch, *IEEE Electron Device Lett.* **19**, 97 (1998).

[69] M. P. Lepselter and S. M. Sze, *Bell System Technical Journal* **47**, 195 (1968).

[70] J. Crofton and S. Sriram, *IEEE Trans. Electron Devices* **43**, 2305 (1996).

[71] K. J. Schoen, J. M. Woodall, J. A. Cooper, and M. R. Melloch, *IEEE Trans. Electron Devices* **45**, 1595 (1998).

[72] M. Treu, R. Rupp, H. Kapels, and W. Bartsch, *Mater. Sci. Forum* **353–356**, 679 (2001).

[73] T. Hatakeyama and T. Shinohe, *Mater. Sci. Forum* **389–393**, 1169 (2002).

[74] E. L. Murphy and R. H. Good, *Phys. Rev.* **102**, 1464 (1956).

[75] F. A. Padovani and R. Stratton, *Solid State Electron.* **9**, 695 (1966).

[76] J. Suda, K. Yamaji, Y. Hayashi, T. Kimoto, K. Shimoyama, H. Namita, and S. Nagao, *Appl. Phys. Express* **3**, 101003 (2010).

[77] M. Higashiwaki, K. Konishi, K. Sasaki, K. Goto, K. Nomura, Q. T. Thieu, R. Togashi, H. Murakami, Y. Kumagai, B. Monemar, A. Koukitu, A. Kuramata, and S. Yamakoshi, *Appl. Phys. Lett.* **108**, 133503 (2016).

[78] T. Maeda, M. Okigawa, Y. Kato, I. Takahashi, and T. Shinohe, *AIP Adv.* **10**, 125119 (2020).

[79] R. Held, N. Kaminski, and E. Niemann, *Mater. Sci. Forum* **264–268**, 1057 (1998).

[80] F. Dahlquist, C. M. Zetterling, M. Östling, and K. Rottner, *Mater. Sci. Forum* **264–268**, 1061 (1998).

[81] L. M. Porter and R. F. Davis, *Mater. Sci. Eng. B* **34**, 83 (1995).

[82] J. Crofton, L. M. Porter, and J. R. Williams, *Phys. Stat. Sol. B* **202**, 581 (1997).

[83] S. Tanimoto, H. Okushi, and K. Arai, Ohmic contacts for power devices on SiC, *Silicon Carbide: Recent Major Advances* (eds. W. J. Choyke, H. Matsunami, and G. Pensl), (Springer, Berlin Heidelberg, 2004), p. 651.

[84] F. Roccaforte, F. La Via, and V. Raineri, *Int. J. High Speed Electron. Syst.* **15**, 781 (2005).

[85] G. Kelner, S. Binari, M. Shur, and J. Palmour, *Electron. Lett.* **27**, 1038 (1991).

[86] J. Crofton, P. G. McMullin, J. R. Williams, and M. J. Bozack, *J. Appl. Phys.* **77**, 1317 (1995).

[87] F. Roccaforte, F. La Via, V. Raineri, L. Calcagno, and P. Musumeci, *Appl. Surf. Sci.* **184**, 295 (2001).

[88] S. Y. Han, K. H. Kim, J. K. Kim, H. W. Jang, K. H. Lee, N.-K. Kim, E. D. Kim, and J.-L. Lee, *Appl. Phys. Lett.* **79**, 1816 (2001).

[89] T. Nakata, K. Koga, Y. Matsushita, Y. Ueda, and T. Niina, Single crystal growth of 6H-SiC by a vacuum sublimation method, and blue LEDs, *Amorphous and Crystalline Silicon Carbide II*, (Springer, Berlin Heidelberg, 1989), p. 26.

[90] J. Crofton, P. A. Barnes, J. R. Williams, and J. A. Edmond, *Appl. Phys. Lett.* **62**, 384 (1993).

[91] B. J. Johnson and M. A. Capano, *Solid State Electron.* **47**, 1437 (2003).

[92] S. Tsukimoto, T. Sakai, and M. Murakami, *J. Appl. Phys.* **96**, 4976 (2004).

[93] S. Tsukimoto, K. Ito, Z. Wang, M. Saito, Y. Ikuhara, and M. Murakami, *Mater. Trans.* **50**, 1071 (2009).

[94] F. La Via, F. Roccaforte, V. Raineri, M. Mauceri, A. Ruggiero, P. Musumeci, L. Calcagno, A. Castaldini, and A. Cavallini, *Microelectron. Eng.* **70**, 519 (2003).

[95] L. Calcagno, A. Ruggiero, F. Roccaforte, and F. La Via, *J. Appl. Phys.* **98**, 023713 (2005).

[96] K. Buchholt, R. Ghandi, M. Domeij, C.-M. Zetterling, J. Lu, P. Eklund, L. Hultman, and A. L. Spetz, *Appl. Phys. Lett.* **98**, 042108 (2011).

[97] S. Tanimoto and H. Ohashi, *Phys. Stat. Sol. A* **206**, 2417 (2009).

[98] S. E. Mohney, B. A. Hull, J. Y. Lin, and J. Crofton, *Solid State Electron.* **46**, 689 (2002).

[99] K. Ito, T. Kobayashi, and T. Kimoto, *Jpn. J. Appl. Phys.* **58**, 078001 (2019).

[100] S. Tanimoto, J. Senzaki, Y. Hayami, H. Hoshi, and H. Okushi, *Extended Abstract of the Symposium on Future Electron Devices*, Vol. 172 (2000), p. 107.

[101] F. A. Mohammad, Y. Cao, and L. M. Porter, *J. Electron. Mater.* **36**, 312 (2007).

[102] H. Shimizu, A. Shima, Y. Shimamoto, and N. Iwamuro, *Jpn. J. Appl. Phys.* **56**, 04CR15 (2017).

[103] T. Doi, S. Shibayama, M. Sakashita, K. Kojima, M. Shimizu, and O. Nakatsuka, *Appl. Phys. Express* **15**, 015501 (2022).

Chapter 2

Barrier Height at Schottky Contacts on Heavily-Doped *n*-Type SiC

2.1 Introduction

A Schottky barrier height is one of the most important properties at a metal/semiconductor interface, which determines a contact resistivity at ohmic contacts, as well as a turn-on voltage and reverse leakage current in Schottky barrier diodes (SBDs). So far, the barrier height at Schottky contacts formed on lightly-doped SiC has extensively been investigated with various electrode metals and for different crystal faces [1–6]. This is because SBDs for power device applications are usually fabricated using SiC with a low doping density, as mentioned in Chap. 1. A noteworthy property for SiC Schottky contacts is found in the barrier height versus metal work function plot shown in Fig. 2.1 [7]. The slope of the plot is nearly equal to unity [8, 9], that is, nearly close to the *Schottky-Mott limit* [10–12], indicating that the interface is free from Fermi-level pinning and allowing the wide-range controllability of the barrier height. Such an exceptional interface property is advantageous in the design and fabrication of SiC SBDs, which has never been seen in Schottky structures on other semiconductor materials [13, 14].

In contrast to the extensive research on the barrier height in lightly-doped SiC SBDs, there exist no reports that precisely characterize the barrier height at Schottky contacts formed on heavily-doped SiC. This is partly because previous studies on metal/heavily-doped SiC junctions have mainly dealt with alloyed interfaces annealed at a high temperature ($\sim$1000°C). In this chapter, the barrier heights in n-type SiC SBDs with various doping densities are investigated in detail via three different techniques, internal photoemission (IPE), capacitance–voltage (C–V), and current–voltage (I–V) measurements. Based on the obtained results, doping density dependence of the barrier height at the metal/SiC interface is quantitatively discussed. Employing various metals as Schottky electrodes, besides, the barrier height is investigated as a function of the metal work function in a wide range of the doping density.

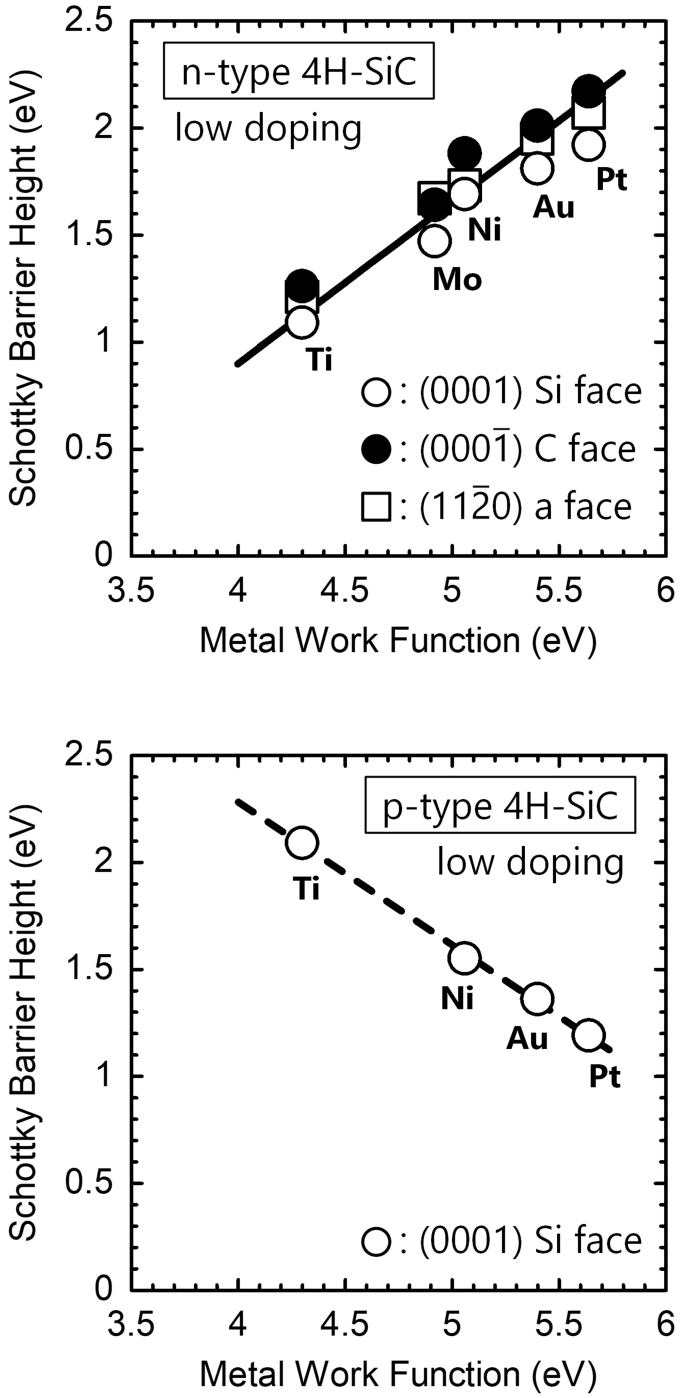

Figure 2.1: Reported barrier height as a function of the metal work function in n- and p-type SiC Schottky structures with various electrode metals and on various crystal faces [7].

2.2 Experiment

A schematic of the fabricated n-type SiC SBDs is depicted in Fig. 2.2. The starting material was an n-type 4H-SiC(0001) substrate with a nitrogen (N)-doped n-type epitaxial layer having various net donor densities ($N_\mathrm{d} = 6.8 \times 10^{15}$–$1.8 \times 10^{19}\,\mathrm{cm}^{-3}$). Note that the values of N_d were confirmed by C–V measurement. The bottom ohmic electrode was formed through Ni deposition onto the backside of the substrates, followed by high-temperature sintering (950°C, 2 min). Circular-shaped Schottky electrodes with a 300–500 μm-diameter were formed on the epilayers by depositing Ni via resistive heating evaporation. Finally, Schottky electrodes were annealed in a vacuum at 300°C [7].

For the fabricated SBDs, the barrier height at zero bias (ϕ_B) was carefully investigated with three different methods: IPE, C–V, and I–V measurements. A detailed explanation of the barrier height extraction procedure for each technique is given in the next section.

2.3 Barrier Height Determination

2.3.1 Internal Photoemission Measurement

IPE measurement is a powerful way to characterize the barrier height with high accuracy [15]. Schematics of the IPE experiment for SBDs and band diagram near a Schottky interface under light irradiation are depicted in Fig. 2.3. The basic concept of this technique is to excite electrons in the metal through light illumination and measure photocurrent ascribed to electrons gaining a higher energy than the barrier height. An apertured backside contact or a transparent Schottky electrode (~ 10 nm) is usually employed to allow the light to reach a Schottky junction. The yield (Y) of IPE at a Schottky contact is proportional to $(h\nu - \phi_\mathrm{B})^2$ under the light illumination with the photon energy of $h\nu$. Therefore, the barrier height is determined from the intercept on the horizontal axis in the $Y^{1/2}$ versus $h\nu$ plot, so-called Fowler plot [16].

In this study, a Xe lamp combined with a monochromator was used as a light source. To obtain the photon number per unit area and time (photon flux), the light intensity of the Xe lamp was measured at various wavelengths (λ) and was normalized by the spot area and photon energy, as shown in Fig. 2.4(a). The sharp peaks at $\lambda = 820$ and 880 nm are bright-line spectra of the Xe lamp. The wavelength of the light was varied from 400–900 nm, corresponding to the photon energy of 1.38–3.10 eV. By using sub-bandgap light ($h\nu < E_\mathrm{g}$), the light irradiated from the front side of SBDs passes through the SiC layer and is reflected by the backside ohmic electrode, reaching the Schottky interface via multiple reflections [17], as illustrated in Fig. 2.4(b). Since the fabricated SBDs have a thick Schottky electrode (> 100 nm) and a backside contact covering the substrate, the multiple reflection-based irradiation method is utilized for the IPE measurement in this study. The photocurrent measurement was performed with no applied bias voltage, and the IPE yield was obtained as

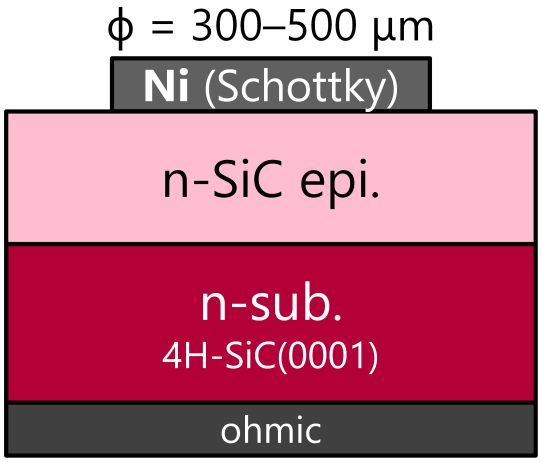

Figure 2.2: Schematic image of the Ni/SiC SBD fabricated on an n-type SiC epitaxial layer.

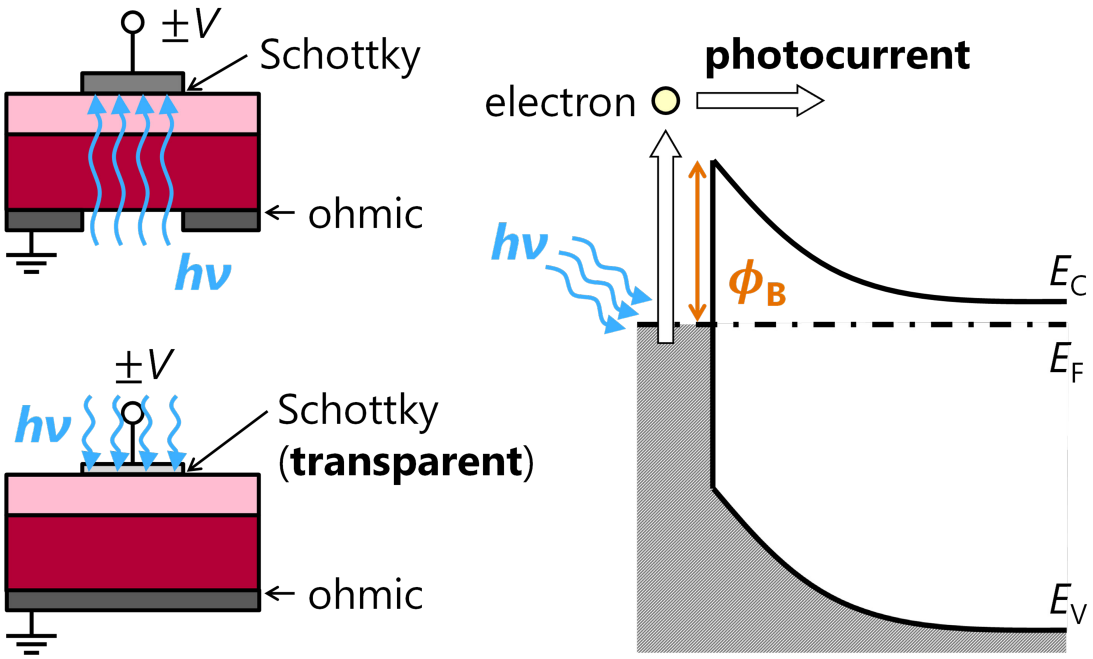

Figure 2.3: Schematic illustration of an SBD under light illumination for the IPE measurement and band diagram near the Schottky interface with an IPE process.

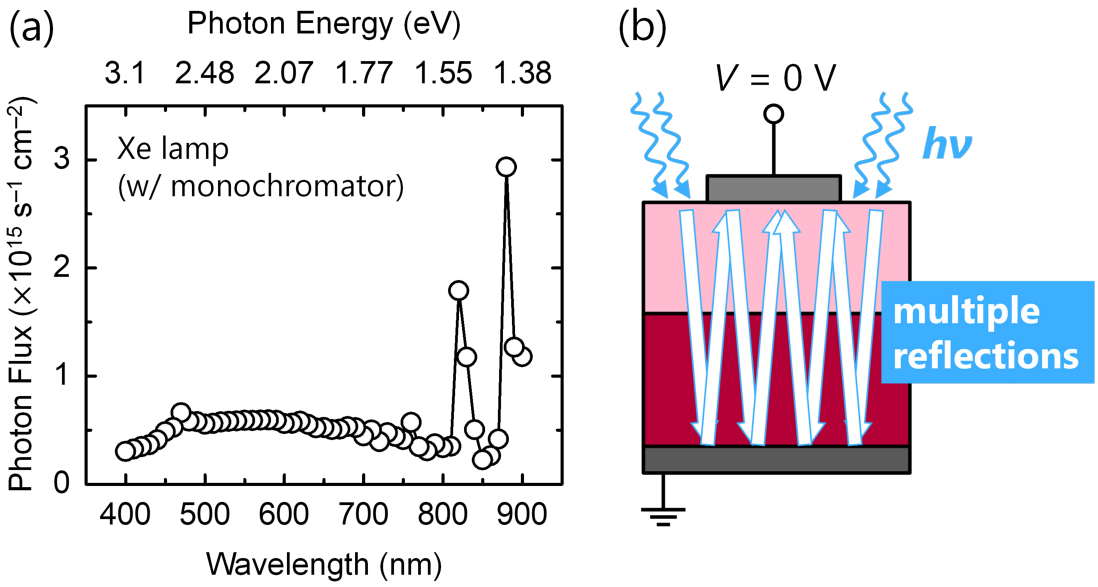

Figure 2.4: (a) Photon flux of the light source (Xe lamp) measured at various wavelengths. (b) Schematic of light illumination to Schottky contact via multiple reflections.

the photocurrent divided by the photon flux. It is confirmed that the measured photocurrent was linearly dependent on the area of the Schottky electrode, resulting from the uniform illumination beneath the contact.

Figure 2.5 shows the Fowler plots of the Ni/SiC SBDs with various N_{d}. The plot shifts to the lower energy side with increasing N_{d}, indicating barrier height lowering at the heavily-doped SiC Schottky contacts. The barrier heights extracted from the Fowler plots are 1.65 and 1.39 eV for the most lightly-doped ($7 \times 10^{15}\,\mathrm{cm}^{-3}$) and heavily-doped ($2 \times 10^{19}\,\mathrm{cm}^{-3}$) SiC SBDs, respectively.

2.3.2 Capacitance–Voltage Measurement

C–V measurement is a useful technique for characterizing electrical properties at a junction and in bulk. The depletion layer width (w) in SBDs with an applied voltage of V is given by [18]

$$w = \sqrt{\frac{2\varepsilon_{\mathrm{s}}(V_{\mathrm{d}} - V)}{eN_{\mathrm{d}}}}, \tag{2.1}$$

where e is the elementary charge, ε_{s} is the dielectric constant ($10.32\varepsilon_0$ in SiC along the c-axis [7]), and V_{d} is the built-in potential at the Schottky contact, respectively. By taking a depletion region as a parallel plate capacitor, the static capacitance (C) of the SBD is derived as [18]

$$C = \varepsilon_{\mathrm{s}}\frac{A}{w} = A\sqrt{\frac{\varepsilon_{\mathrm{s}}eN_{\mathrm{d}}}{2(V_{\mathrm{d}} - V)}}, \tag{2.2}$$

where A is the area of the Schottky contact. Based on Eq. (2.2), a $1/C^2$–V plot shows a linear relationship, and N_{d} and V_{d} can be extracted from the slope and intercept on the horizontal axis, respectively.

Considering the band diagram near a Schottky interface depicted in Fig. 2.6, the barrier height at zero bias is expressed as [18]

$$\phi_{\mathrm{B}} = eV_{\mathrm{d}} + \Delta E_{\mathrm{Fs}} + k_{\mathrm{B}}T - \Delta\phi, \tag{2.3}$$

where k_{B} is the Boltzmann constant, T is the absolute temperature, ΔE_{Fs} is the energy difference between the conduction band edge (E_{C}) and Fermi level in the semiconductor (E_{Fs}), and $\Delta\phi$ is the barrier lowering by the image force effect, respectively. Therefore, the ϕ_{B} determination further requires ΔE_{Fs} and $\Delta\phi$, which can be calculated with N_{d} and V_{d} obtained from C–V measurement.

Basically, E_{Fs} is mutually dependent on the carrier density in the semiconductor. For a non-degenerate semiconductor with a relatively low carrier density (doping density), E_{Fs} and carrier density can analytically and individually be calculated based on the Boltzmann approximation. In the case of high doping density, on the other hand, the Boltzmann approximation is no longer valid, and these valuables have to be self-consistently calculated

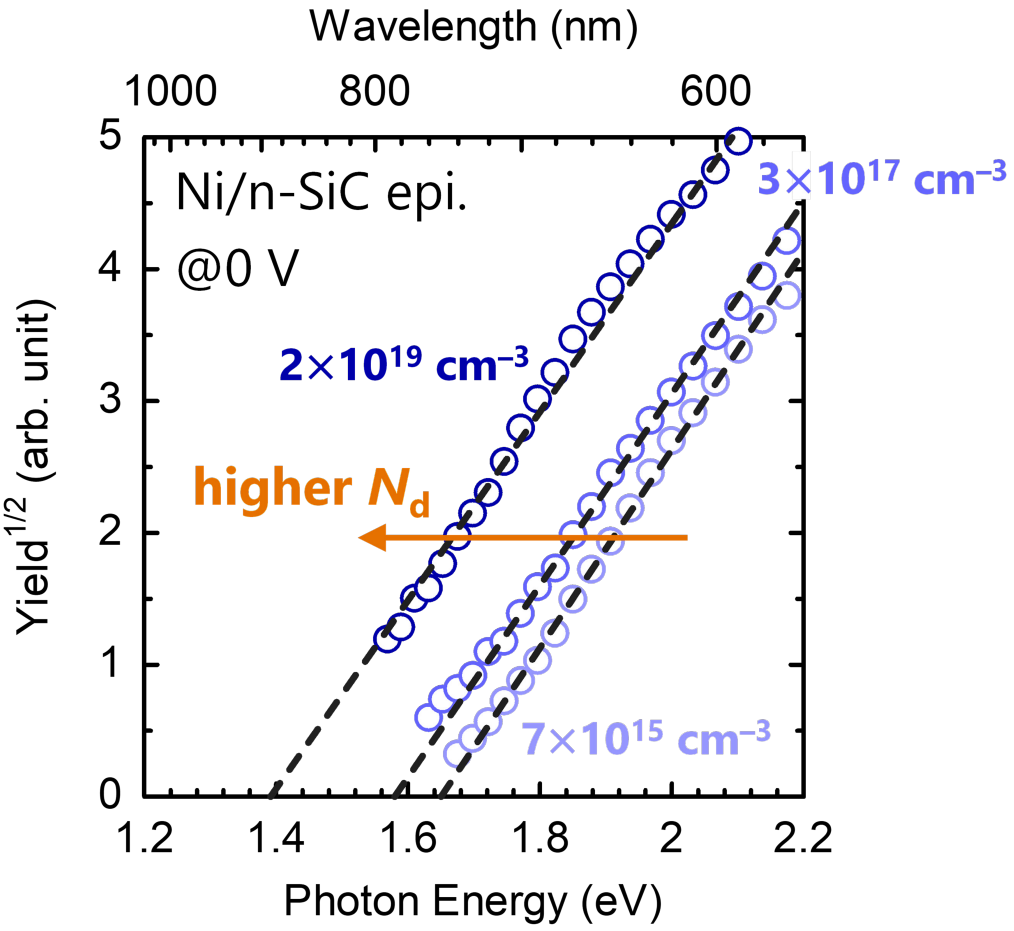

Figure 2.5: Square root of the photocurrent yield (arbitrary unit) as a function of the photon energy, so-called Fowler plot, for the Ni/SiC SBDs ($N_\mathrm{d} = 7 \times 10^{15}$, 3×10^{17}, and $2 \times 10^{19}\,\mathrm{cm}^{-3}$).

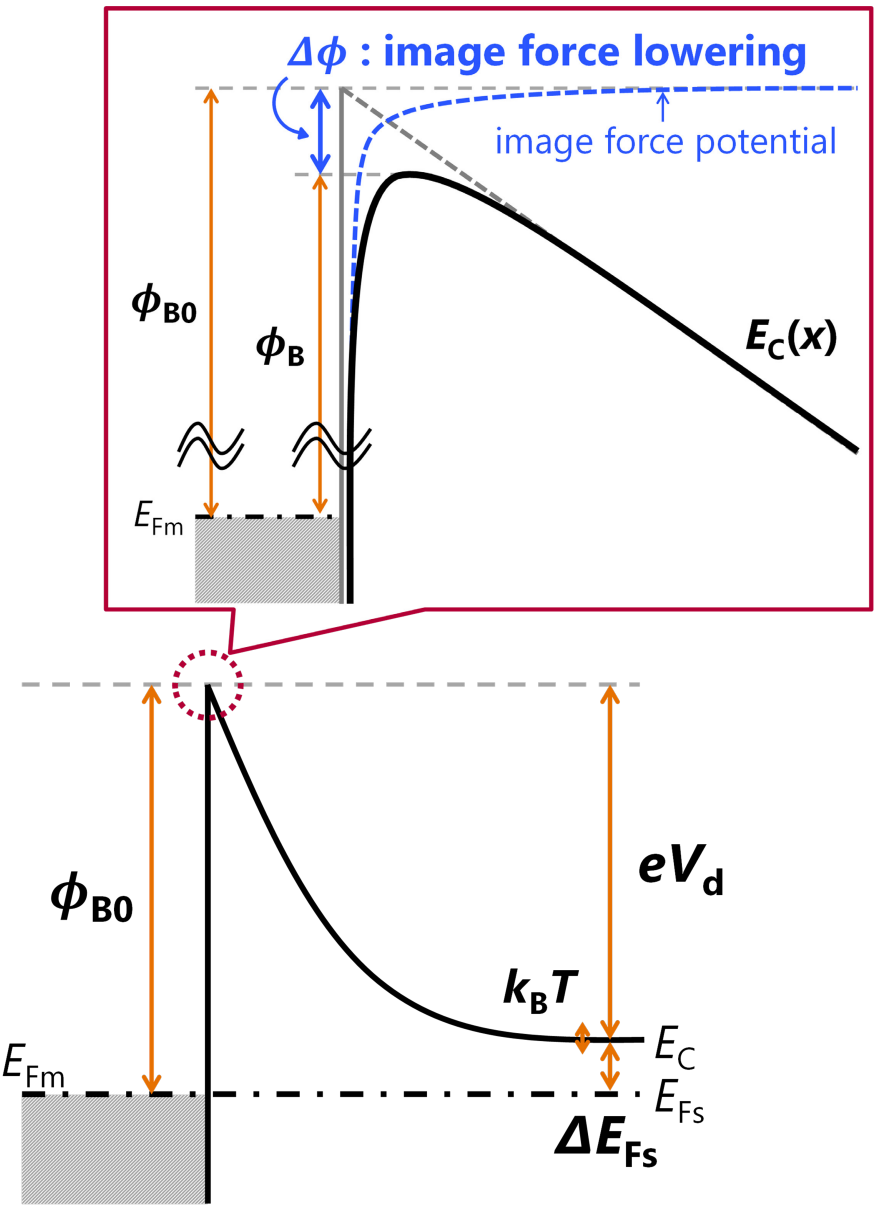

Figure 2.6: Band diagram near a Schottky interface representing the barrier height and its components.

based on a numerical approach with the Fermi-Dirac statistics. In this study, E_{Fs} was numerically calculated because N_{d} was varied in a quite wide range. A detailed description of the Fermi level calculation is found in Appendix A. The barrier lowering by image force effect ($\Delta\phi$) is expressed as [18]

$$\Delta\phi = \sqrt{\frac{eF_{\max}}{4\pi\varepsilon_{\mathrm{s}}}}, \tag{2.4}$$

where $F_{\max}$ is the maximum electric field at the Schottky interface, given by [18]

$$F_{\max} = \sqrt{\frac{2eN_{\mathrm{d}}(V_{\mathrm{d}} - V)}{\varepsilon_{\mathrm{s}}}}. \tag{2.5}$$

Based on these equations, the barrier height can be determined using V_{d} and N_{d} obtained from C–V measurement.

Figure 2.7 shows the $1/C^2$–V plots for the Ni/SiC SBDs with various N_{d}. The $1/C^2$–V curves show good linearity for each N_{d}. The extracted V_{d} increases with increasing N_{d}: 1.53 V for $7 \times 10^{15}\,\mathrm{cm}^{-3}$ to 1.66 V for $2 \times 10^{19}\,\mathrm{cm}^{-3}$. As opposed to the increase in V_{d}, ΔE_{Fs} decreases with increasing N_{d} like 0.20 eV for $7 \times 10^{15}\,\mathrm{cm}^{-3}$ and 0.01 eV for $2 \times 10^{19}\,\mathrm{cm}^{-3}$, respectively. As a result, the zero-field barrier height, defined as

$$\phi_{\mathrm{B0}} = eV_{\mathrm{d}} + \Delta E_{\mathrm{Fs}} + k_{\mathrm{B}}T, \tag{2.6}$$

is turned out to be almost constant regardless of N_{d} ($\phi_{\mathrm{B0}} \simeq 1.7\,\mathrm{eV}$). On the other hand, as seen in Eqs. (2.4) and (2.5), the barrier height drop due to the image force effect strongly depends on N_{d}: 0.03 eV for $7 \times 10^{15}\,\mathrm{cm}^{-3}$ and 0.21 eV for $2 \times 10^{19}\,\mathrm{cm}^{-3}$. Consequently, the barrier height at zero bias (ϕ_{B}) determined by Eq. (2.3) decreases with increasing N_{d} from 1.74 eV ($7 \times 10^{15}\,\mathrm{cm}^{-3}$) to 1.49 eV ($2 \times 10^{19}\,\mathrm{cm}^{-3}$).

2.3.3 Current–Voltage Measurement — Thermionic Emission

The I–V relationship of an SBD is often expressed as [18]

$$J = J_0 \left\{ \exp\left(\frac{eV}{nk_{\mathrm{B}}T}\right) - 1 \right\}, \tag{2.7}$$

where J is the current density, J_0 is the saturation current density, and n is the ideality factor, respectively. In the case that the carrier transport in an SBD is dominated by the most well-known mechanism of the thermionic emission (TE), which is the conduction of electrons having higher energy than the barrier height, n equals unity, and J_0 is expressed as

$$J_0 = \frac{4M_{\mathrm{C}}\pi e m^*_{\mathrm{e},\perp} k_{\mathrm{B}}T^2}{h^3} \exp\left(-\frac{\phi_{\mathrm{B}}}{k_{\mathrm{B}}T}\right) = A^*T^2 \exp\left(-\frac{\phi_{\mathrm{B}}}{k_{\mathrm{B}}T}\right), \tag{2.8}$$

where h is the Planck constant, M_{C} is the number of equivalent conduction band minima, $m^*_{\mathrm{e},\perp}$ is the effective mass perpendicular to the direction in which the carriers travel, and A^* is the effective Richardson constant, respectively. A^* is calculated to be $151\,\mathrm{A/cm^2K^2}$

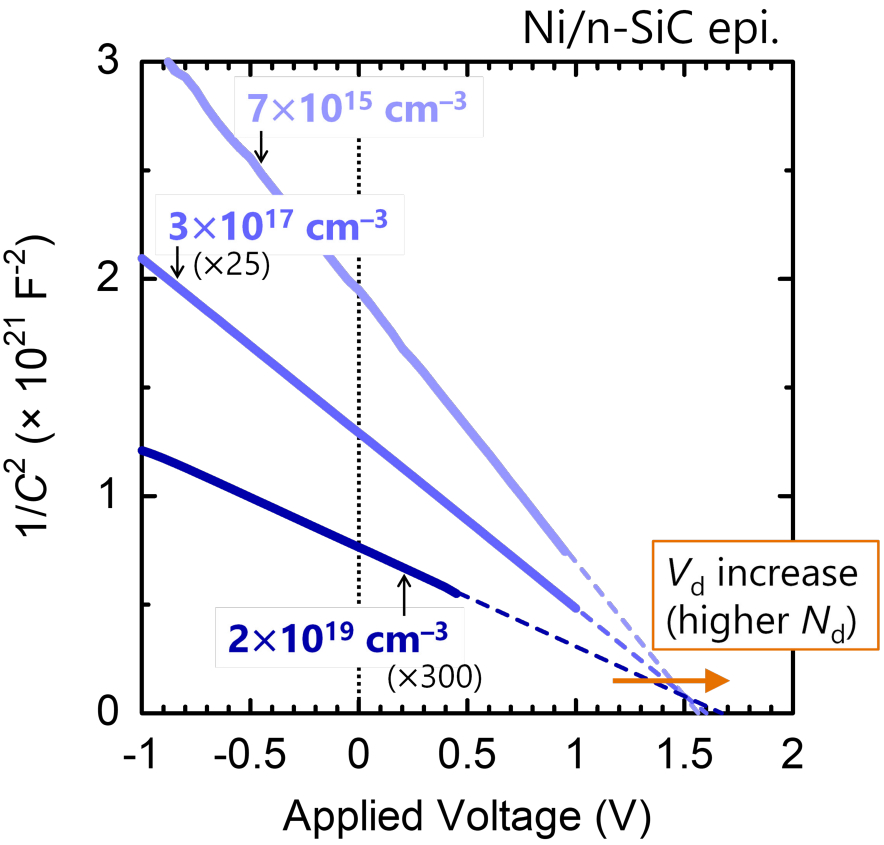

Figure 2.7: $1/C^2$–V plots of the Ni/SiC SBDs with various donor densities ($N_\mathrm{d} = 7\times10^{15}$, 3×10^{17}, and $2 \times 10^{19}\,\mathrm{cm}^{-3}$). The $1/C^2$ values are magnified by multiplying a constant indicated in the figure for $N_\mathrm{d} = 3 \times 10^{17}$ and $2 \times 10^{19}\,\mathrm{cm}^{-3}$.

with $M_c = 3$ [4] and $m^*_{e,\perp} = 0.42m_0$ [19, 20] (m_0: electron rest mass). Based on Eq. (2.8), ϕ_B is determined with J_0 extracted from the intercept of J–V plots under a forward bias where n corresponds to unity.

Figure 2.8 shows the forward J–V relationships of the Ni/SiC SBDs with various N_d. A larger current is observed in the lower voltage range ($< 1\,V$) with increasing N_d, leading to a larger J_0. Through the conventional TE-based analysis based on Eq. (2.8), in which n and J_0 are treated as parameters to reproduce the experimental data (indicated by the dashed lines in Fig. 2.8), ϕ_B is determined to be 1.68 eV for the lightly-doped SiC SBDs ($N_d = 7 \times 10^{15}\,cm^{-3}$) and is extracted as 0.79 eV for the heavily-doped SiC SBDs ($N_d = 2 \times 10^{19}\,cm^{-3}$), respectively.

2.3.4 Consistency Among Three Different Techniques

Figure 2.9 plots the N_d dependence of the barrier height at zero bias (ϕ_B) in the Ni/SiC SBDs obtained by IPE, C–V, and I–V measurements. For the IPE and C–V measurements, the obtained ϕ_B values agree well with each other in a wide range of N_d. However, ϕ_B determined from the TE-based analysis of the forward I–V characteristics sharply decreases with increasing N_d, and the ϕ_B values largely deviate from those obtained from the other techniques, especially at a higher N_d. This result suggests that the TE model no longer describes the carrier transport in the heavily-doped SiC SBDs. Thus, the ideality factor n was extracted from the forward I–V curves to roughly presume the dominant conduction mechanism. As shown in Fig. 2.10, n increases for a higher N_d, and $n = 2.01$ is obtained for $N_d = 2 \times 10^{19}\,cm^{-3}$, which is much larger than $n = 1.00$ for $N_d = 7 \times 10^{15}\,cm^{-3}$. The deviation of n from unity implies the contribution of another carrier transport mechanism except for TE.

Then, the depletion layer width w and the electric field at the Schottky interface F_{max} in the heavily-doped SiC Schottky structure are focused on. Figure 2.11 shows the N_d dependence of w and F_{max} at zero bias in the fabricated Ni/n-SiC SBDs. The symbols represent the values calculated using the experimental N_d and V_d from the C–V measurement, and the solid lines are fitting curves ($w \propto N_d^{-1/2}$ and $F_{max} \propto N_d^{1/2}$). As seen in Fig. 2.11, w significantly decreases with increasing N_d, and F_{max} exhibits a sharp increase at a higher N_d: w is 500 nm, and F_{max} is less than 0.1 MV/cm at zero bias for $N_d = 7 \times 10^{15}\,cm^{-3}$, while w is 10 nm, and F_{max} reaches 3.2 MV/cm for $N_d = 2 \times 10^{19}\,cm^{-3}$ even at zero bias. It is notable that, for a lightly-doped SiC SBD ($N_d = 1 \times 10^{16}\,cm^{-3}$) with a high reverse voltage applied ($V \sim -1000\,V$), F_{max} is calculated to be about 2 MV/cm, under which electron tunneling described by the thermionic field emission (TFE) model occurs, as introduced in Chap. 1 [21, 22]. Therefore, TFE transport is plausibly dominant in the forward-biased heavily-doped SiC SBDs.

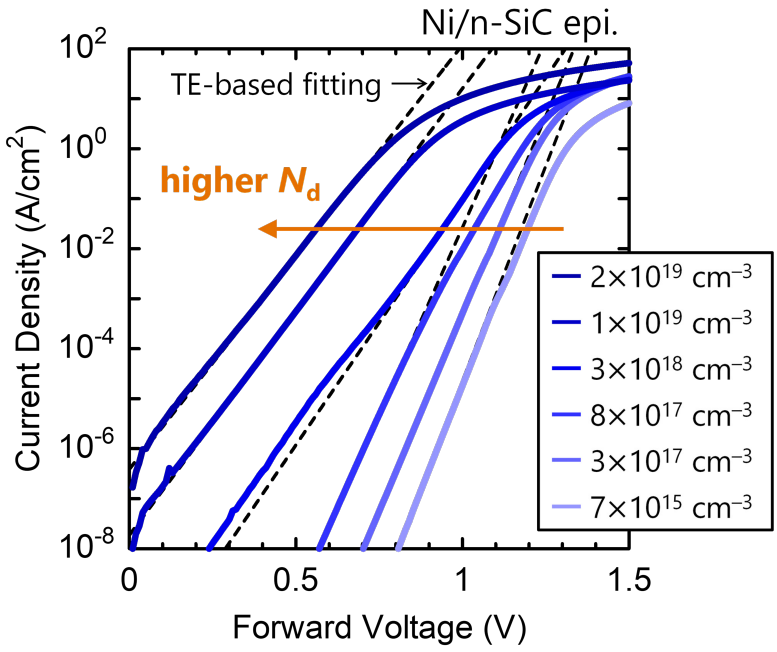

Figure 2.8: Forward I–V characteristics of the Ni/SiC SBDs with various donor densities ($N_\mathrm{d} = 7 \times 10^{15}$–$2 \times 10^{19}\,\mathrm{cm}^{-3}$).

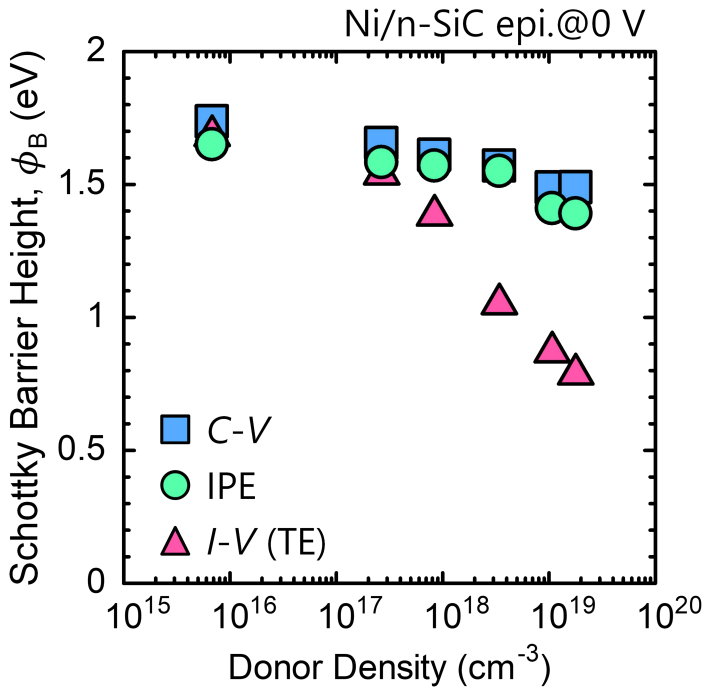

Figure 2.9: Donor density dependence of the barrier height at zero bias (ϕ_B) in the Ni/SiC SBDs extracted from C–V, IPE, and I–V measurements. For the heavily-doped SiC SBDs ($N_\mathrm{d} > 8 \times 10^{17}\,\mathrm{cm}^{-3}$), the ϕ_B values obtained by the TE-based analysis of the forward I–V characteristics largely deviate from those determined by C–V and IPE measurements.

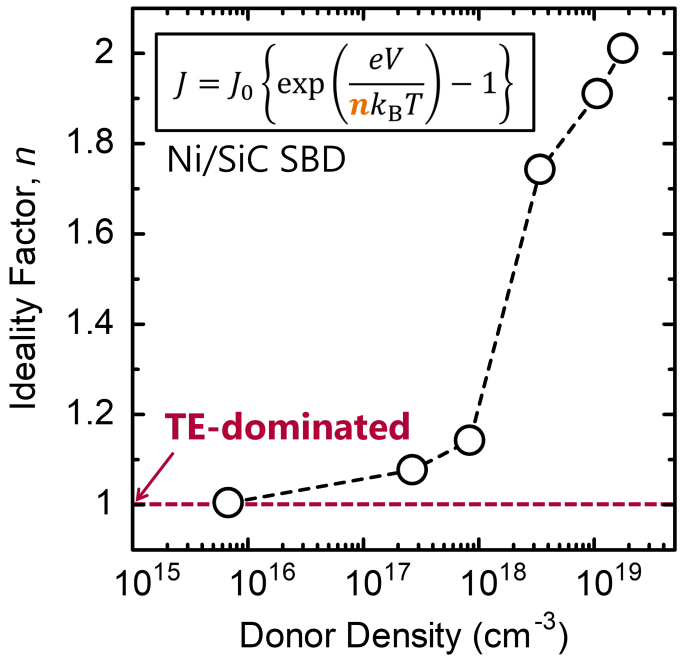

Figure 2.10: Donor density dependence of the ideality factor extracted from the forward I–V characteristics of the Ni/SiC SBDs.

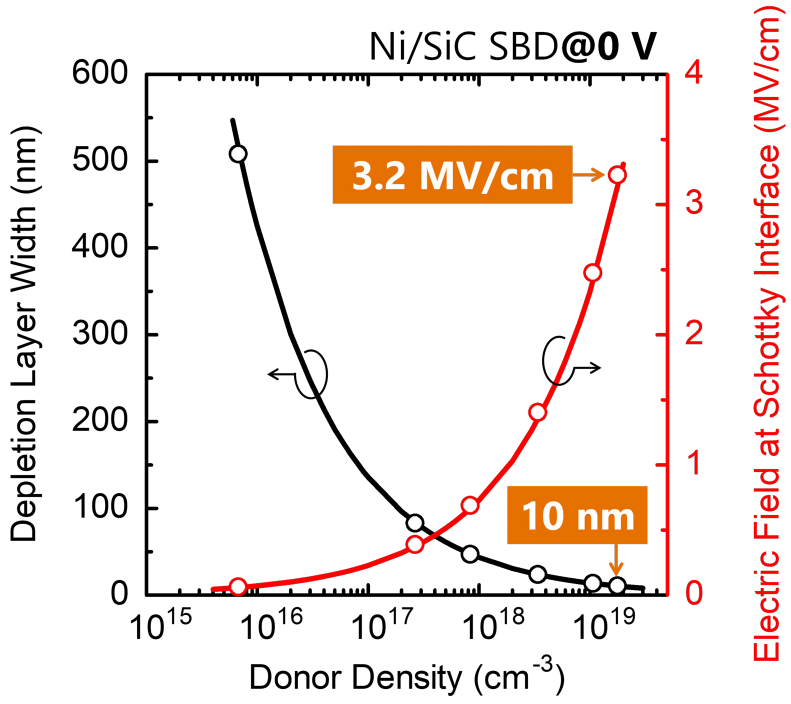

Figure 2.11: Donor density dependence of the depletion layer width and electric field at the Schottky interface at zero bias in the Ni/SiC SBDs.

2.3.5 Current–Voltage Measurement — Thermionic Field Emission

The forward TFE current is given by [23]

$$J_{\mathrm{TFE,F}} = J_{0,\mathrm{TFE}}(V) \exp\left(\frac{eV}{E_0}\right), \tag{2.9}$$

$$J_{0,\mathrm{TFE}} = \frac{A^* T \sqrt{\pi E_{00}(\phi_{\mathrm{B}} - \Delta E_{\mathrm{Fs}} - eV)}}{k_{\mathrm{B}} \cosh(E_{00}/k_{\mathrm{B}}T)} \exp\left(-\frac{\Delta E_{\mathrm{Fs}}}{k_{\mathrm{B}}T} - \frac{\phi_{\mathrm{B}} - \Delta E_{\mathrm{Fs}}}{E_0}\right), \tag{2.10}$$

$$E_{00} = \frac{e\hbar}{2}\sqrt{\frac{N_{\mathrm{d}}}{m^* \varepsilon_{\mathrm{s}}}}, \quad E_0 = E_{00} \coth\left(\frac{E_{00}}{k_{\mathrm{B}}T}\right), \tag{2.11}$$

where $\hbar$ is the Dirac constant and m^* is the effective mass along the tunneling direction, respectively. For the heavily-doped SiC SBDs ($> 10^{17}\,\mathrm{cm}^{-3}$), ϕ_{B} was extracted through a fitting analysis to the experimental forward I–V curves with the above formulas. In the calculation, m^* was set to be $0.33m_0$, corresponding to the effective mass at E_{C} along the c-axis [19], and the voltage drop due to the series resistance, which was extracted from the experimental I–V curves, was included when plotting the calculated I–V characteristics.

Figure 2.12 shows the calculated and experimental I–V characteristics of the heavily-doped SiC SBDs ($N_{\mathrm{d}} = 3\times10^{17}$ and $2\times10^{19}\,\mathrm{cm}^{-3}$). The calculation of the TFE current gives good agreement with the experimental results for each N_{d}. Based on the TFE-based analysis, ϕ_{B} is determined as 1.63 eV for $3\times10^{17}\,\mathrm{cm}^{-3}$ and 1.52 eV for $2\times10^{19}\,\mathrm{cm}^{-3}$, respectively. These values are consistent with those obtained by the IPE and C–V measurements.

2.4 Barrier Height vs. Donor Density

Figure 2.13 again plots the N_{d} dependence of the barrier height at zero bias (ϕ_{B}) in the Ni/SiC SBDs determined by IPE measurement, C–V measurement, and TFE-based analysis of the forward I–V characteristics. By adopting the analysis of TFE current, ϕ_{B} is consistently determined from the three different methods in a wide N_{d} range, as seen in Fig. 2.13. As mentioned in Sect. 2.3.2, the zero-field barrier height (ϕ_{B0}) expressed by Eq. (2.6) is constantly obtained regardless of N_{d} from the C–V measurement. Since the barrier heights extracted from IPE and I–V measurements intrinsically include the image force lowering, the barrier height values were calculated by taking the sum of the experimental ϕ_{B}(IPE or I–V) and $\Delta\phi$ calculated with Eq. (2.4), which were also confirmed to be almost constant independent of N_{d}. Therefore, it is expected from Eq. (2.3) that the ϕ_{B} drop according to the N_{d} increase is likely explained by the image force effect. The red dashed line in Fig. 2.13 indicates the barrier height calculated considering the N_{d} dependence of the image force lowering given by Eqs. (2.4) and (2.5),

$$\phi_{\mathrm{B}}(N_{\mathrm{d}}) = \phi_{\mathrm{B0}}[\mathrm{Const.}] - \Delta\phi(N_{\mathrm{d}}). \tag{2.12}$$

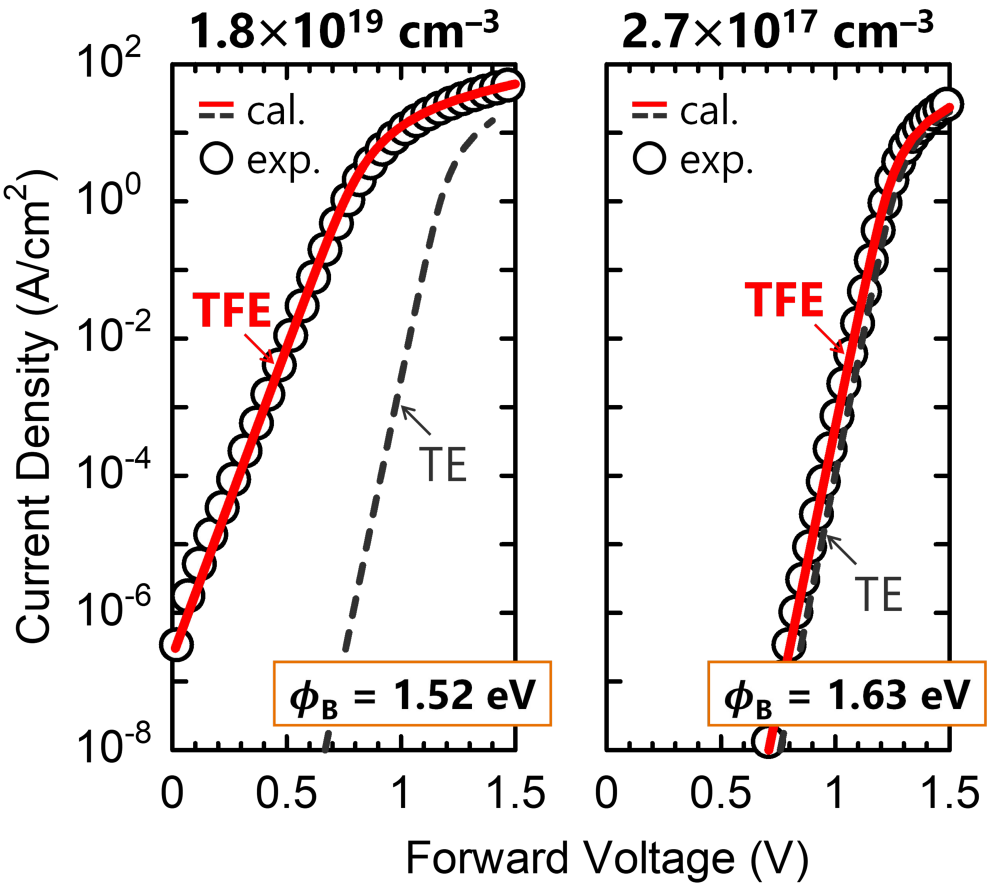

Figure 2.12: Forward I–V characteristics of the Ni/SiC SBDs ($N_\mathrm{d} = 1.8 \times 10^{19}$ and $2.7 \times 10^{17}\,\mathrm{cm}^{-3}$) obtained from the experiment and calculation based on the TE and TFE models.

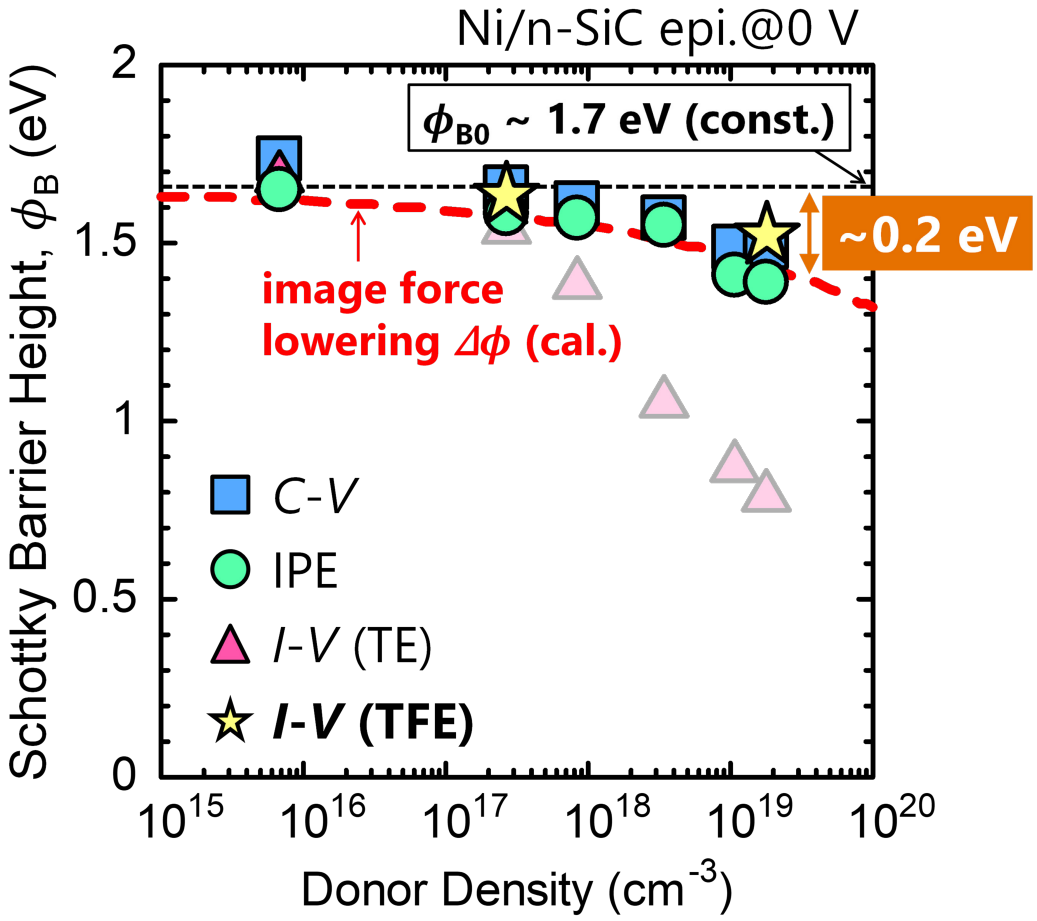

Figure 2.13: Barrier height at zero bias (ϕ_B) versus donor density in the Ni/SiC SBDs determined by the IPE measurement, C–V measurement, and TFE-based analysis of the forward I–V characteristics. By adopting the analysis of TFE current, ϕ_B is consistently obtained from the three different methods in a wide N_d range. Besides, the ϕ_B values are also in good agreement with the calculated barrier height described by $\phi_{B0} - \Delta\phi$, where ϕ_{B0} is the zero-field barrier height (constant), and $\Delta\phi$ is the image force lowering, respectively.

Here, the constant ϕ_{B0}[Const.] is set to be 1.7 eV based on the experimental results from C–V measurement. As seen in Fig. 2.13, the barrier height drop experimentally observed in the heavily-doped SiC SBDs agrees well with the calculated image force lowering. Consequently, it is clarified that the significant barrier height lowering in a heavily-doped SiC SBD is quantitatively explained by the image force effect.

2.5 Barrier Height vs. Metal Work Function

To better understand interface properties in metal/heavily-doped SiC Schottky structures, this section discusses the metal work function (ϕ_m) dependence of the barrier height in heavily-doped SiC SBDs. In this study, Ti and Mg were chosen as Schottky electrodes in addition to Ni, and SBDs were fabricated with epitaxially grown n-type SiC having various N_d (10^{17}–$10^{19}\,cm^{-3}$). The fabrication procedure is almost the same as described in Sect. 2.2, while the bottom electrode was formed just by depositing Al, and no thermal treatment was conducted after the Schottky electrode formation. The barrier height extraction was performed by C–V and I–V measurements.

Figure 2.14 shows the N_d dependence of ϕ_B obtained by C–V measurement on the Ni/, Ti/, and Mg/SiC SBDs. Note that C–V measurement was hardly conducted for the Mg/SiC SBDs with N_d above mid-$10^{18}\,cm^{-3}$ due to a significant tunneling current. As seen in Fig. 2.14, the barrier height is clearly dependent on the Schottky electrode metal. In each case, the ϕ_{B0} value is almost constant regardless of N_d: $\phi_{B0} \simeq 1.6$ eV for the Ni electrodes, 1.1 eV for Ti, and 0.7 eV for Mg, respectively. Furthermore, the barrier height drop due to the image force effect is commonly observed. It should be noted that the $\Delta\phi$ value is dependent on the electrode metal, reflecting the difference in V_d and F_{max}. Thus, when discussing the barrier height in heavily-doped SiC SBDs as a function of the metal work function, "the zero-field barrier height (ϕ_{B0}) at the same N_d" or "the barrier height containing the image force effect (ϕ_B) under the same F_{max}" has to be used for a fair and accurate analysis excluding the $\Delta\phi$ difference.

Figure 2.15 presents ϕ_{B0} versus ϕ_m plots in the n-type SiC SBDs with N_d = 2–5 × $10^{17}\,cm^{-3}$, 4–6 × $10^{18}\,cm^{-3}$, and 1 × $10^{19}\,cm^{-3}$. Note that the ϕ_{B0} values given in the plot for the Mg/SiC SBDs ($N_d = 4\times10^{18}$ and $1\times10^{19}\,cm^{-3}$) are obtained from the analysis of the tunneling current. The ϕ_m value of each electrode metal was characterized by performing ultraviolet photoelectron spectroscopy (UPS) measurement on the deposited metal film, which gives an electronic structure in the valence band through investigating the kinetic energy of electrons emitted by the ultraviolet light illumination [15]. It is found that the barrier heights in the SiC Schottky structure can be controlled in a wide range (ϕ_{B0} = 0.7–1.6 eV) by employing a Schottky electrode with a different ϕ_m. As expected from the N_d-independent ϕ_{B0}, the slope of the ϕ_{B0}–ϕ_m plot, so-called *S value*, is independent of N_d. The S value of 0.52–0.58 is obtained, which is much higher than that observed in Schottky

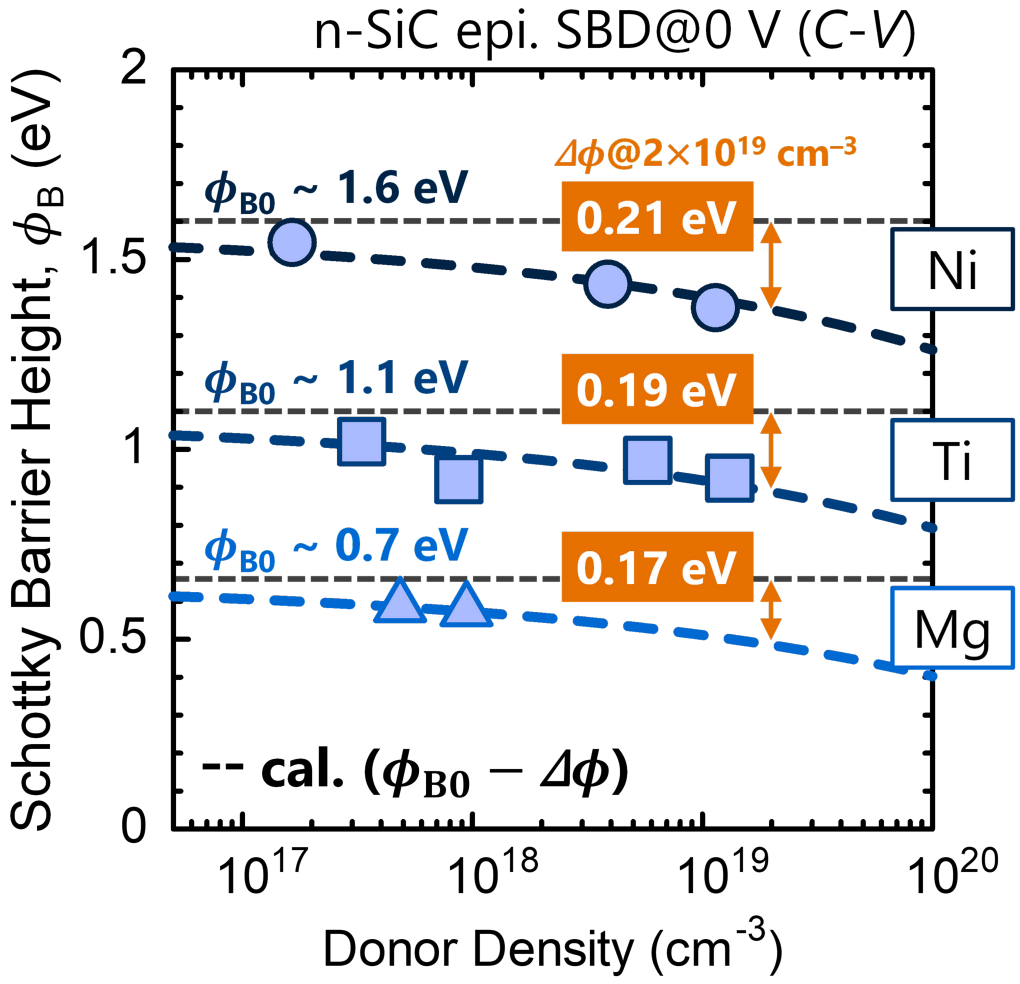

Figure 2.14: Donor density dependence of the barrier height at zero bias (ϕ_B) in the Ni/, Ti/, and Mg/SiC SBDs extracted from C–V measurement. The barrier height drop ($\Delta\phi$) in the heavily-doped SiC SBDs is well described by the image force lowering for each Schottky electrode metal. The $\Delta\phi$ values depend on the kind of electrode metal, which results from the difference in the built-in potential (i.e., the difference in the maximum electric field at the Schottky interface).

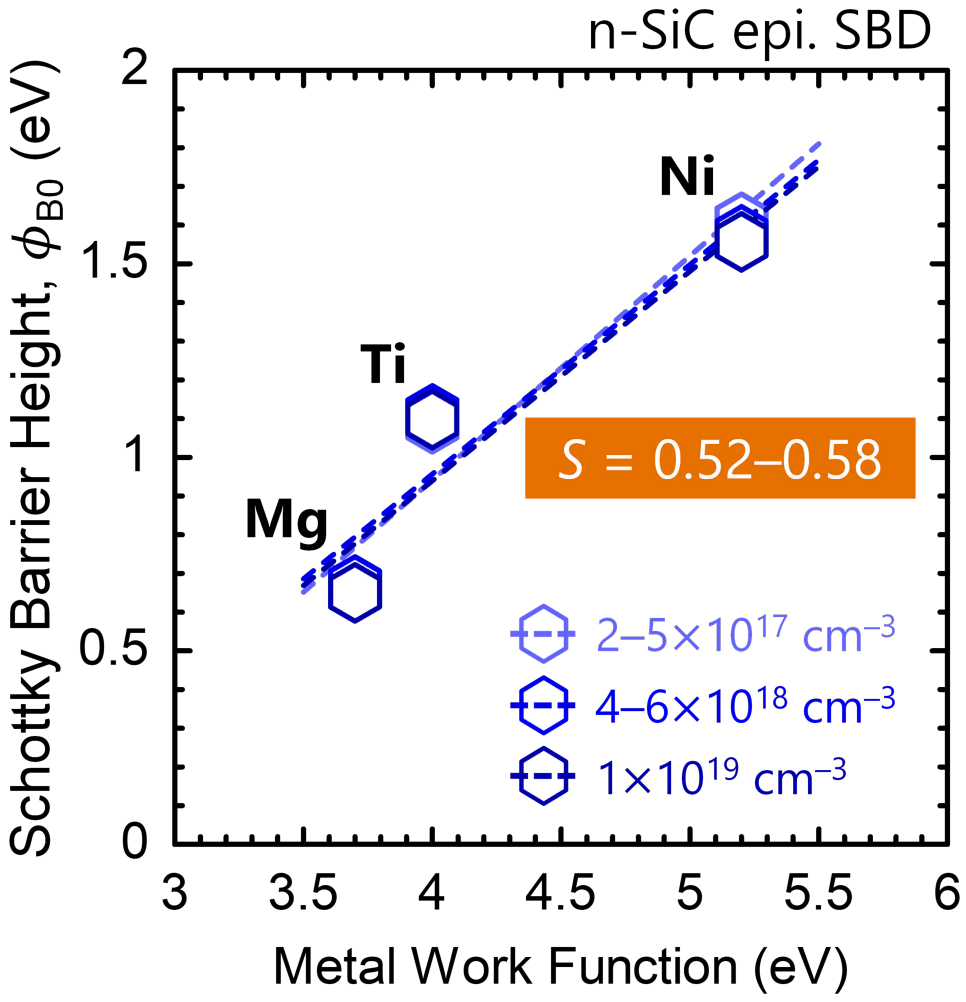

Figure 2.15: Zero-field barrier height (ϕ_{B0}) versus metal work function (ϕ_m) in the Schottky structures formed on n-type SiC epitaxial layers with various N_d. The slope of the ϕ_{B0}–ϕ_m plot, so-called *S value*, is about 0.5–0.6, almost independent of N_d.

contacts on other semiconductor materials such as Si, gallium arsenide (GaAs), and so on (typically 0.1–0.2) [24]. This result indicates that the image force lowering is the only factor that changes the barrier height when increasing the doping density. Besides, SiC Schottky contacts are nearly free from the Fermi-level pinning irrespective of the doping density of SiC, even though the S value is still smaller than the ideal case of unity. The wide-range controllability of the barrier height helps the physics-based design and formation of non-alloyed SiC ohmic contacts.

2.6 Discussion

The author again emphasizes the significance of the image force effect in metal/heavily-doped semiconductor systems. The image force lowering is so minor that it is often neglected in the barrier height determination procedure. Although it does not matter when a doping density is low enough, the barrier height is significantly affected by this effect in the case of a Schottky structure formed on a heavily-doped semiconductor in which a very high electric field ($\sim$ MV/cm) exists even at zero bias, as discussed above. Therefore, the *zero-field barrier height* (ϕ_{B0}) and *barrier height including the image force effect* (ϕ_{B}) must be defined and discussed separately for the accurate analysis of Schottky barriers at metal/heavily-doped semiconductor interfaces.

The ϕ_{B0} versus ϕ_{m} plot presented in Sect. 2.5 gives valuable insights into the design and formation of SiC ohmic contacts. As is the case of lightly-doped SiC SBDs reported previously, the barrier height at metal/heavily-doped SiC Schottky interfaces is also controllable in a wide range by employing a Schottky metal with a different ϕ_{m}, that is, a lower ϕ_{m} leads to a lower barrier height. On the other hand, it is known that, in the case of the alloyed ohmic contacts formed on heavily-doped n-type SiC, Ni-based electrodes show a better contact resistivity than Ti, despite the lower ϕ_{m} of Ti than Ni [25–27]. This fact implies the necessity of the detailed characterization of the barrier height and contact resistivity at metal/heavily-doped SiC interfaces, starting with the no-sintering case and then elevating the annealing temperature, for the comprehensive understanding of the contact resistivity reduction through the high-temperature process.

From another perspective, how the barrier height at SiC Schottky contacts changes with a further high doping density is both scientifically and practically crucial. The bandgap narrowing caused by high doping is a potential effect that can cause a barrier height change. Persson *et al.* calculated the energetic band structure and doping-induced bandgap modulation in n- and p-type SiC [28]. Figure 2.16 plots the energy shift of the conduction band minimum in n-type SiC against the ionized donor density [28]. Since the E_{C} shift leads not only to a change in the carrier density (i.e., E_{Fs}) but also to the work function of SiC, it is not easy to take this effect into account quantitatively in the barrier height determination. On the other hand, a minor impact by the bandgap narrowing on the barrier height is

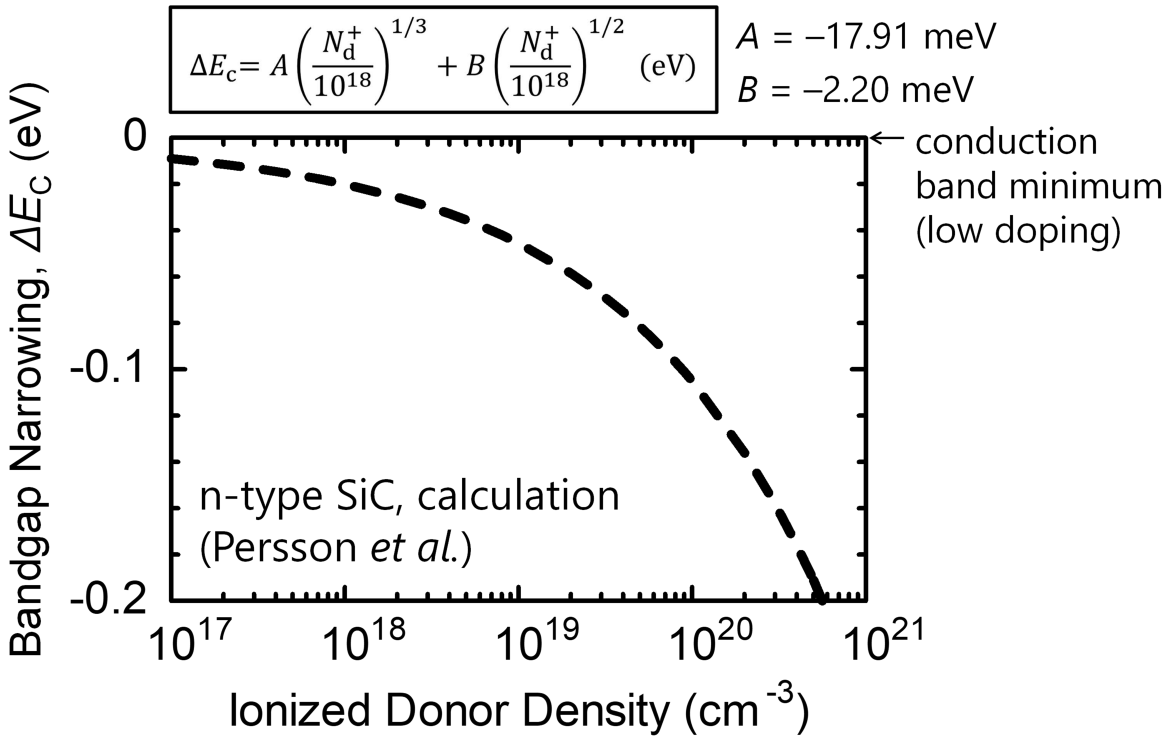

Figure 2.16: Doping-induced energy shift of the conduction band minimum in n-type SiC (bandgap narrowing) calculated by an analytical formula, whose parameters were obtained by energetic band structure calculation, reported by Persson *et al.* [28].

expected even with a higher donor density ($N_\mathrm{d} > 2 \times 10^{19}\,\mathrm{cm}^{-3}$) because the energy shift is only about 0.1 eV even with a high ionized donor density (carrier density) of $1 \times 10^{20}\,\mathrm{cm}^{-3}$, as shown in Fig. 2.16. Note that the carrier density in n-type SiC is calculated as about $3 \times 10^{19}\,\mathrm{cm}^{-3}$ when $N_\mathrm{d} = 1 \times 10^{20}\,\mathrm{cm}^{-3}$, and the ionization ratio of the donor decreases with further increasing N_d, as shown in Appendix A. Although no significant changes in the barrier height are expected, an experimental study on the bandgap narrowing, which has never been conducted, is essential for a deeper understanding of the barrier height in heavily-doped SiC Schottky structures. Since accurate determination of the bandgap modulation in several tens of meV from barrier height characterization is challenging, another approach is required to experimentally specify the bandgap narrowing, such as investigating the doping density dependence of the carrier injection in p-n junctions and performing optical absorption measurements on heavily-doped SiC samples.

2.7 Summary

In this chapter, the author fabricated vertical SBD structures and systematically characterized the Schottky barrier height at metal/heavily-doped SiC interfaces in terms of the dependency on the donor density of SiC and the work function of the Schottky electrode. By performing the analysis of forward I–V characteristics in heavily-doped SiC SBDs ($N_\mathrm{d} > 10^{17}\,\mathrm{cm}^{-3}$) based on the TFE transport, which is caused by the high electric field ($\sim$ MV/cm) due to the high doping, the barrier heights were consistently determined with three different techniques, IPE, C–V, and I–V measurements. The barrier height at zero bias (ϕ_B) decreased with increasing N_d, and the amount of ϕ_B drop in the Ni/SiC SBDs was about 0.2 eV between $N_\mathrm{d} = 7 \times 10^{15}$ and $1 \times 10^{19}\,\mathrm{cm}^{-3}$, which quantitatively agreed with the calculated image force lowering ($\Delta\phi = 0.18\,\mathrm{eV}$). The zero-field barrier height (ϕ_B0), defined as the barrier height without including the image force effect, was almost constant, independent of N_d. With employing various Schottky electrode metals ($\phi_\mathrm{m} = 3.7$–$5.2\,\mathrm{eV}$), the barrier height at metal/heavily-doped SiC Schottky interfaces is controllable in a wide-range ($\phi_\mathrm{B0} = 0.7$–$1.6\,\mathrm{eV}$), as is the case for lightly-doped SiC Schottky structures.

These fundamental barrier properties at metal/heavily-doped SiC Schottky interfaces help to clarify the formation mechanism of alloyed ohmic contacts and design and fabricate non-alloyed ohmic contacts.

References

[1] J. R. Waldrop, *J. Appl. Phys.* **75**, 4548 (1994).

[2] A. Itoh, T. Kimoto, and H. Matsunami, *IEEE Electron Device Lett.* **16**, 280 (1995).

[3] L. M. Porter and R. F. Davis, *Mater. Sci. Eng. B* **34**, 83 (1995).

[4] A. Itoh and H. Matsunami, *Phys. Stat. Sol. A* **162**, 389 (1997).

[5] S. K. Lee, C. M. Zetterling, and M. Östling, *J. Electron. Mater.* **30**, 242 (2001).

[6] O. Shigiltchoff, S. Bai, R. P. Devaty, W. J. Choyke, T. Kimoto, D. Hobgood, P. G. Neudeck, and L. M. Porter, *Mater. Sci. Forum* **433–436**, 705 (2003).

[7] T. Kimoto and J. A. Cooper, *Fundamentals of Silicon Carbide Technology: Growth, Characterization, Devices and Applications* (John Wiley & Sons, 2014).

[8] S. Hara, *Surf. Sci.* **494**, L805 (2001).

[9] T. Teraji and S. Hara, *Phys. Rev. B* **70**, 035312 (2004).

[10] N. F. Mott, *Proc. R. Soc. Lond. A* **171**, 27 (1939).

[11] W. Schottky, *Zeitschrift für Physik* **118**, 539 (1942).

[12] J. Bardeen, *Phys. Rev.* **71**, 717 (1947).

[13] A. M. Cowley and S. M. Sze, *J. Appl. Phys.* **36**, 3212 (1965).

[14] V. Heine, *Phys. Rev.* **138**, A1689 (1965).

[15] D. K. Schroder, *Semiconductor Material and Device Characterization* (John Wiley & Sons, 3rd edition, 2005).

[16] R. H. Fowler, *Phys. Rev.* **38**, 45 (1931).

[17] T. Maeda, M. Okada, M. Ueno, Y. Yamamoto, T. Kimoto, M. Horita, and J. Suda, *Appl. Phys. Express* **10**, 051002 (2017).

[18] S. M. Sze, Y. Li, and K. K. Ng, *Physics of Semiconductor Devices* (John Wiley & Sons, 4th edition, 2021).

[19] D. Volm, B. K. Meyer, D. M. Hofmann, W. M. Chen, N. T. Son, C. Persson, U. Lindefelt, O. Kordina, E. Sörman, A. O. Konstantinov, B. Monemar, and E. Janzén, *Phys. Rev. B* **53**, 15409 (1996).

[20] C. Persson and U. Lindefelt, *J. Appl. Phys.* **82**, 5496 (1997).

[21] M. Treu, R. Rupp, H. Kapels, and W. Bartsch, *Mater. Sci. Forum* **353–356**, 679 (2001).

[22] T. Hatakeyama and T. Shinohe, *Mater. Sci. Forum* **389–393**, 1169 (2002).

[23] F. A. Padovani and R. Stratton, *Solid State Electron.* **9**, 695 (1966).

[24] L. J. Brillson, *Surf. Sci. Rep.* **2**, 123 (1982).

[25] J. Crofton, L. M. Porter, and J. R. Williams, *Phys. Stat. Sol. B* **202**, 581 (1997).

[26] S. Tanimoto, H. Okushi, and K. Arai, Ohmic contacts for power devices on SiC, *Silicon Carbide: Recent Major Advances* (eds. W. J. Choyke, H. Matsunami, and G. Pensl), (Springer, Berlin Heidelberg, 2004), p. 651.

[27] F. Roccaforte, F. La Via, and V. Raineri, *Int. J. High Speed Electron. Syst.* **15**, 781 (2005).

[28] C. Persson, U. Lindefelt, and B. E. Sernelius, *J. Appl. Phys.* **86**, 4419 (1999).

Chapter 3

Direct Tunneling Through Schottky Contacts on Heavily-Doped n-Type SiC

3.1 Introduction

In Chap. 2, several unique high-field phenomena in heavily-doped SiC Schottky structures were found: significant barrier height lowering due to the image force effect and forward tunneling current described by the thermionic field emission (TFE) instead of thermionic emission (TE). Since Chap. 2 extensively discussed the Schottky barrier height at metal/heavily-doped SiC interfaces, this chapter then focuses on further detailed analysis of tunneling current in heavily-doped SiC Schottky structures. Considering reverse-biased heavily-doped SiC Schottky barrier diodes (SBDs), for instance, the electric field should become much higher than that under a forward bias condition. Thus, the tunneling current explained by the field emission (FE), which is the tunneling process without thermal excitation of carriers [1, 2], is likely observed under a reverse bias.

Although it is generally understood that tunneling of carriers is responsible for the ohmic behavior at metal/semiconductor contacts containing a Schottky barrier, discussions on the mechanism of ohmic-like conduction are performed qualitatively in many cases. Therefore, systematic experiments and quantitative analyses have not been conducted regarding the tunneling current at metal/heavily-doped SiC junctions. A profound knowledge of the tunneling phenomena at heavily-doped SiC Schottky contacts is crucial in establishing the design guideline for non-alloyed ohmic contacts with a low contact resistivity (ρ_{c}). Besides, understanding the interface carrier transport helps clarify the formation mechanism of alloyed (sintered) ohmic contacts on SiC.

In this chapter, vertical SiC SBDs are fabricated using heavily-doped n-type SiC epitaxial layers with various net donor densities (N_{d}), and their forward and reverse current–voltage (I–V) characteristics are analyzed by numerical calculation of the tunneling current, which

includes both the TFE and FE transport. Based on the calculation, changes in the dominant tunneling process depending on the electric field are discussed in detail.

3.2 Theory of Direct Tunneling

3.2.1 Numerical Formula

The fundamental formula for the direct tunneling (DT) current from a metal to a semiconductor is given as [3]

$$J_{\mathrm{DT}} = \frac{A^* T}{k_{\mathrm{B}}} \int P_{\mathrm{DT}}(E) \ln \left[\frac{\exp\{-(E - E_{\mathrm{Fm}})/k_{\mathrm{B}}T\} + 1}{\exp\{-(E - E_{\mathrm{Fs}})/k_{\mathrm{B}}T\} + 1} \right] \mathrm{d}E, \tag{3.1}$$

where A^* is the effective Richardson constant ($151\,\mathrm{A/cm^2K^2}$ as calculated in Chap. 2), T is the absolute temperature, k_{B} is the Boltzmann constant, E is the electron energy along the tunneling direction, and E_{Fm} and E_{Fs} are the Fermi levels in the metal and semiconductor, respectively. Note that J_{DT} in the opposite direction (semiconductor to metal) is given just by flipping E_{Fm} and E_{Fs}. $P_{\mathrm{DT}}(E)$ is the tunneling probability and is derived by the WKB approximation as [4]

$$P_{\mathrm{DT}}(E) = \exp \left[-\frac{2\sqrt{2m^*}}{\hbar} \int_{x_{\mathrm{in}}}^{x_{\mathrm{out}}} \sqrt{U(x) - E}\mathrm{d}x \right], \tag{3.2}$$

where $\hbar$ is the Dirac constant, m^* is the effective mass along the tunneling direction, $U(x)$ is the energy potential in the depletion region in the semiconductor, and x_{in} and x_{out} are the positions of the incident and transmitted electrons, respectively.

3.2.2 Thermionic Field Emission and Field Emission

As mentioned above, the DT process is often classified into two mechanisms, TFE and FE, which describe the tunneling phenomenon with thermal carriers and cold carriers, respectively, as depicted in Fig. 3.1(a) and (b). As schematically illustrated in Fig. 3.1(c), the integrand in Eq. (3.1), defined as $J(E)$, has a peak value at a certain energy. This is because $P_{\mathrm{DT}}(E)$ exponentially increases with higher energy, while the latter factor, which comes from the Fermi-Dirac distribution function (i.e., the energy distribution of carriers), exponentially decreases. The energy giving a peak value of the integrand (defined as E_{peak}) allows us to judge the dominant tunneling process at metal/semiconductor interfaces [2]. In other words, TFE and FE are distinguished by investigating whether E_{peak} is higher than or similar to the conduction band edge (E_{C}) in the semiconductor (forward bias) or E_{Fm} (reverse bias), even though the numerical formula Eq. (3.1) does not specify which of TFE or FE is predominant. Based on this concept, analytical formulas to calculate the TFE and FE current have been derived from Eq. (3.1), assuming a reasonable E_{peak},

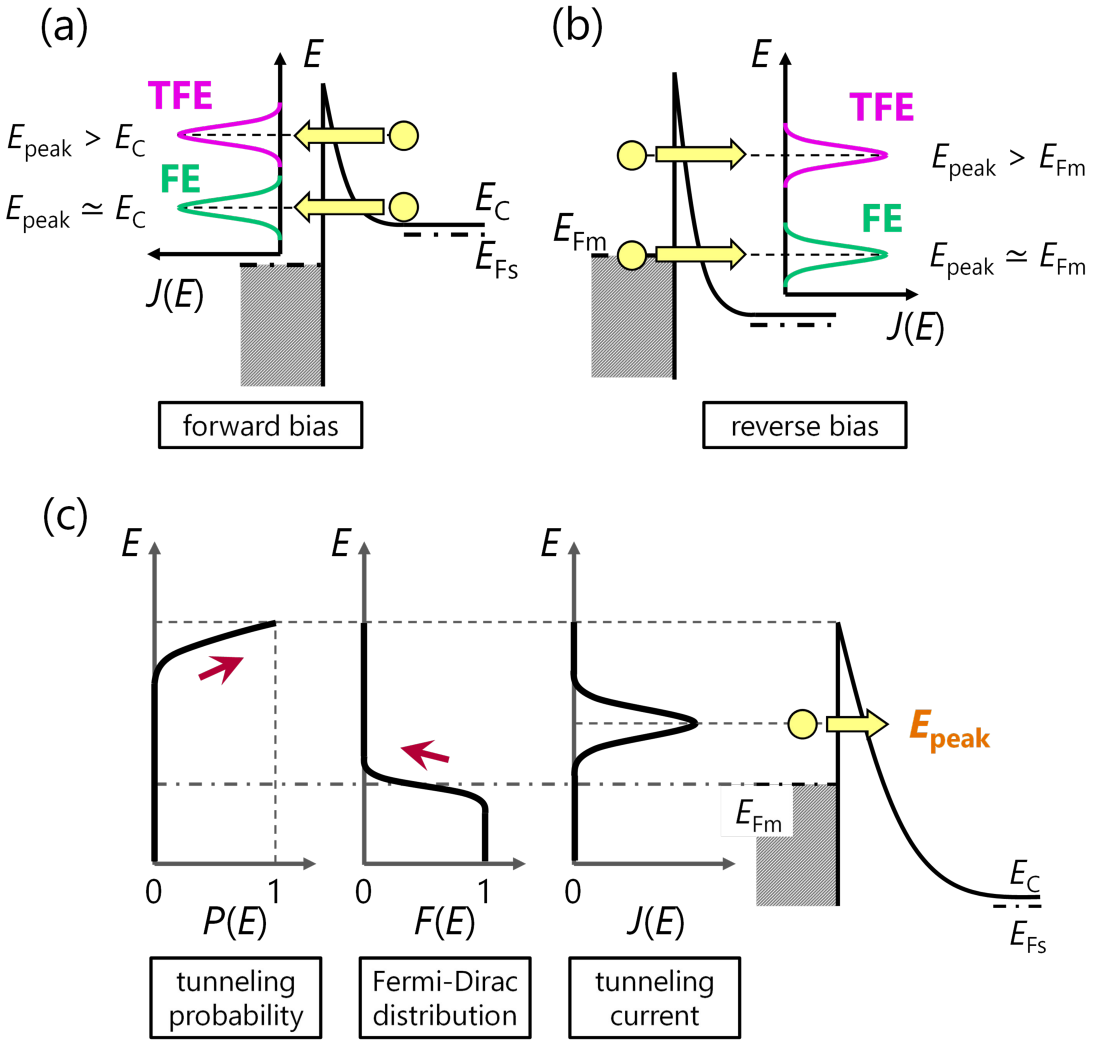

Figure 3.1: Classification of thermionic field emission (TFE) and field emission (FE) under (a) forward and (b) reverse biases. (c) Schematic illustration of tunneling probability, Fermi-Dirac distribution function, and tunneling current as a function of the electron energy.

and how the dominant tunneling process changes depending on the temperature, electric field, and barrier height has been discussed in detail [1, 2, 5]. Although these analytical models are beneficial, one has to be aware that they are not applicable when the dominant tunneling process changes from TFE to FE in a finite voltage range because the TFE-FE transition usually occurs continuously. Besides, several analytical models deal with a uniform distribution of the electric field in a depletion region, which is valid only for the case of lightly-doped semiconductors or gate oxides in MOS structures. With a high doping density, however, the electric field rapidly decreases as the position becomes far from the Schottky interface. Consequently, when varying the doping density in a vast range, applied voltage bias, and Schottky barrier height, the conventional analytical formulas are not applicable to metal/heavily-doped SiC systems, and it is necessary to perform the numerical calculation based on Eq. (3.1) to analyze the DT current accurately.

3.3 Experiment and Calculation

Nitrogen (N)-doped n-type SiC epitaxial layers with various N_d (10^{17}–$10^{19}\,\mathrm{cm}^{-3}$) on n-type 4H-SiC(0001) substrates were prepared for the SBD fabrication. The N_d values were determined by C–V measurement on each SBD. Ni, Ti, and Mg were chosen as Schottky electrodes, which were deposited on the epitaxial layers via resistive heating evaporation. The forward and reverse I–V characteristics of the fabricated SBDs were measured at room temperature and analyzed based on Eq. (3.1).

Figure 3.2 depicts the band diagram near an n-type SiC Schottky interface for the DT current calculation. The energy potential to calculate $P_\mathrm{DT}(E)$ was defined as the sum of the parabolic and image force potentials,

$$U(x) = \frac{e^2 N_\mathrm{d}}{2\varepsilon_\mathrm{s}} x^2 - \frac{e^2 N_\mathrm{d} w}{\varepsilon_\mathrm{s}} x - \frac{e^2}{16\pi\varepsilon_\mathrm{s} x}, \tag{3.3}$$

where e is the elementary charge, ε_s is the dielectric constant of SiC along the c-axis ($10.32\varepsilon_0$) [6], and w is the depletion layer width, respectively. The effective mass at E_C along the c-axis in SiC ($0.33m_0$ where m_0 is the electron rest mass) [7] was chosen as m^* in Eq. (3.2) because the tunneling direction corresponds to the c-axis. In the calculation, the zero-field barrier height (ϕ_B0), defined without including the image force lowering, was varied as a parameter to calculate the DT current. Although ϕ_B0 is not explicitly included in Eqs. (3.1)–(3.3), several valuables in these equations are obtained from ϕ_B0, like

$$E_\mathrm{Fm} = -\phi_\mathrm{B0}, \tag{3.4}$$

$$E_\mathrm{Fs} = -\phi_\mathrm{B0} + eV, \tag{3.5}$$

$$eV_\mathrm{d} = \phi_\mathrm{B0} - \Delta E_\mathrm{Fs} - k_\mathrm{B}T. \tag{3.6}$$

Here, since the calculation dealt with a very wide range of N_d, ΔE_Fs was numerically calculated based on the Fermi-Dirac statistics instead of the Boltzmann approximation, as

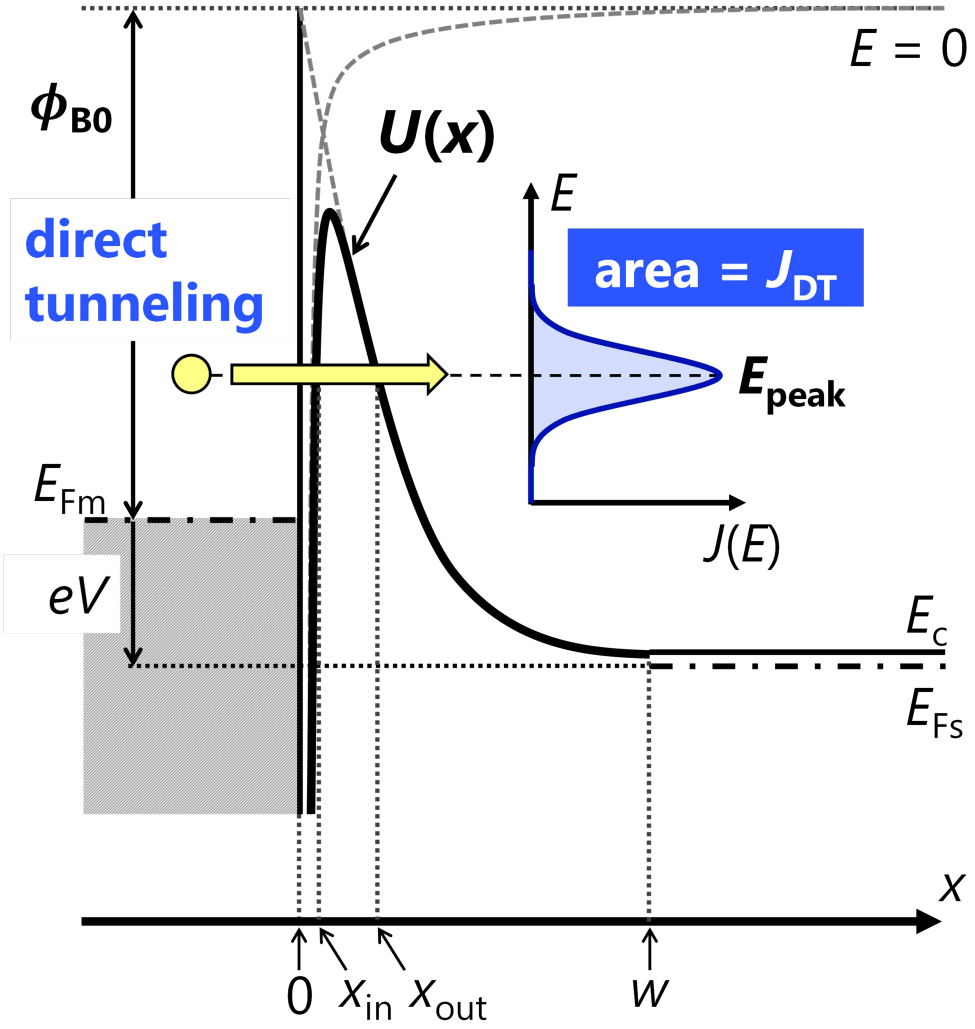

Figure 3.2: Band diagram near a metal/n-type SiC Schottky interface for the calculation of direct tunneling (DT) current.

is the case in Chap. 2. The calculation algorithm for the DT current as a function of V is as follows:

1. The energy potential, $U(x)$, is determined at a given voltage V applied to the Schottky junction.

2. The minimum and maximum energies for the integration are calculated ($E_{\rm C}$ and $\phi_{\rm B0} - \Delta\phi$, respectively, where $\Delta\phi$ is the barrier height drop due to the image force effect [8]). Note that $\Delta\phi$ was obtained by investigating the peak value of $U(x)$, which was confirmed to be almost the same as the value calculated based on Eq. (2.4).

3. The obtained energy range is divided by a large number (e.g., $N = 1000$) to calculate the Riemann integral.

4. $x_{\rm in}$, $x_{\rm out}$, and then $P_{\rm DT}(E)$ are calculated for each energy.

5. The integrand of Eq. (3.1), $J(E)$, is calculated.

6. $J_{\rm DT}$ at the given V is obtained by performing the Riemann integral (i.e., taking the sum of $J(E){\rm d}E$ for the entire energy range).

7. The above procedures are repeated by varying V. Note that the voltage drop due to the series resistance ($R_{\rm series}$) was added to V (i.e., $V + R_{\rm series}J_{\rm DT}$) when plotting the calculated DT current.

3.4 Current–Voltage Characteristics

Figure 3.3 shows the forward and reverse I–V curves of the heavily-doped SiC SBDs ($N_{\rm d} = 3\times10^{17}$–$1\times10^{19}\,{\rm cm}^{-3}$) with Ti as a Schottky electrode obtained from the experiment (square symbols) and the DT current calculation (solid lines). For each $N_{\rm d}$, the calculated DT current agrees well with the experimental data in a wide range of the current density (10^{-5}–$1\,{\rm A/cm}^2$) under both forward and reverse biases. Figure 3.4 plots the experimental and calculated I–V characteristics of the n-type SiC SBDs with a similar $N_{\rm d}$ (4–$6\times10^{18}\,{\rm cm}^{-3}$) fabricated by employing different Schottky electrodes of Ni, Ti, and Mg. The DT current calculation shows good agreement with the experimental I–V curves even when another Schottky electrode metal is employed. As expected from the work function ($\phi_{\rm m}$) difference, the Mg/SiC SBDs exhibit the largest current with almost identical $N_{\rm d}$ because of their lowest barrier height, while the smallest current is observed in the Ni/SiC SBDs with the highest barrier height. Through the numerical calculation, $\phi_{\rm B0}$ values were obtained to be about 1.6 eV (Ni), 1.0 eV (Ti), and 0.7 eV (Mg), almost independent of $N_{\rm d}$, which were consistent with those extracted from the C–V characteristics. Figure 3.5 plots the barrier height at zero bias including the image force effect ($\phi_{\rm B}$) as a function of $N_{\rm d}$ for the Ni/, Ti/, and Mg/SiC SBDs. As shown in Fig. 3.5, C–V measurement and the DT current analyses

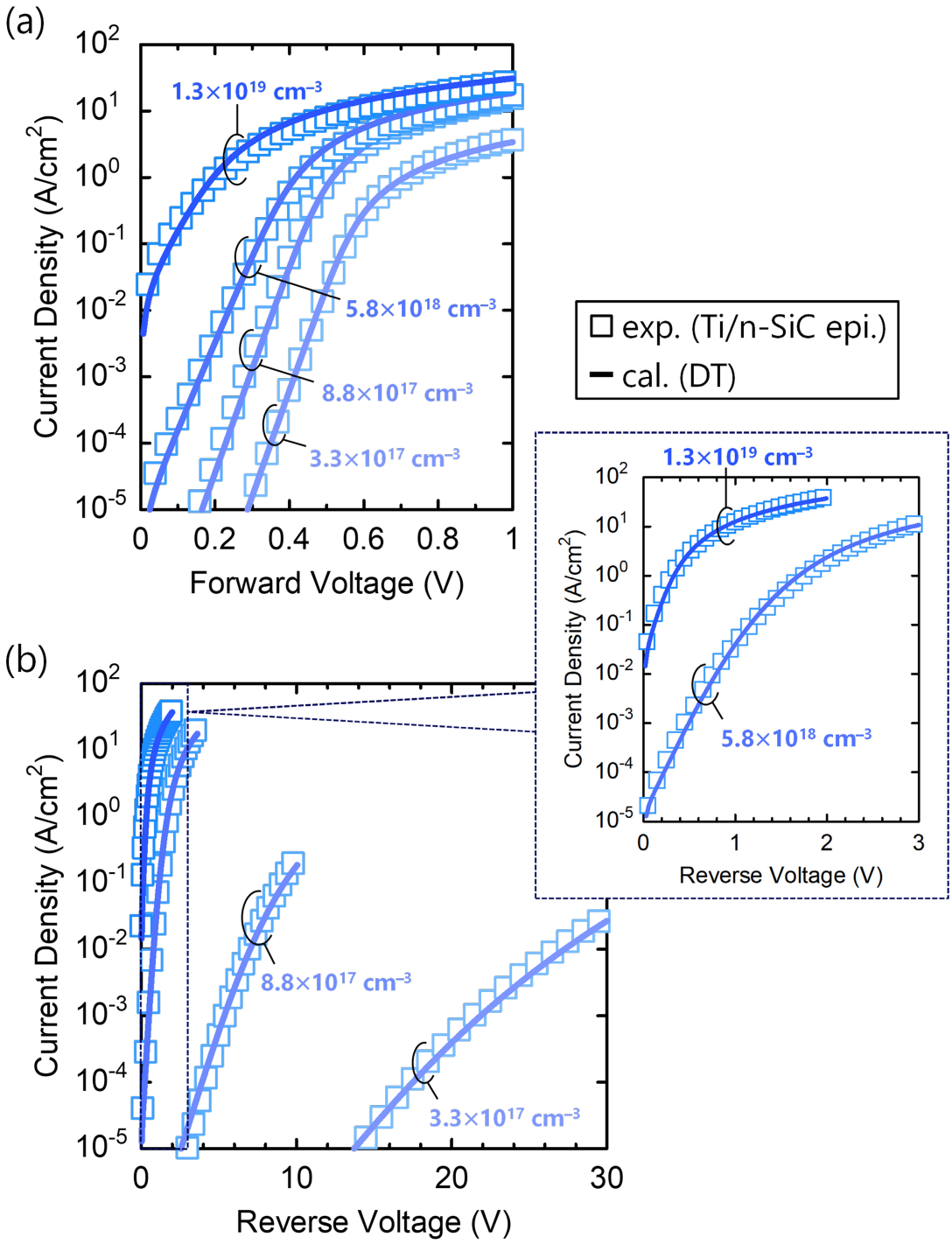

Figure 3.3: (a) Forward and (b) reverse I–V characteristics of the Ti/SiC SBDs fabricated on n-type SiC epitaxial layers with various N_d (3×10^{17}–$1 \times 10^{19}\,\mathrm{cm}^{-3}$). The calculated DT current well reproduces the experimental I–V curves in a vast range of N_d under both forward and reverse biases.

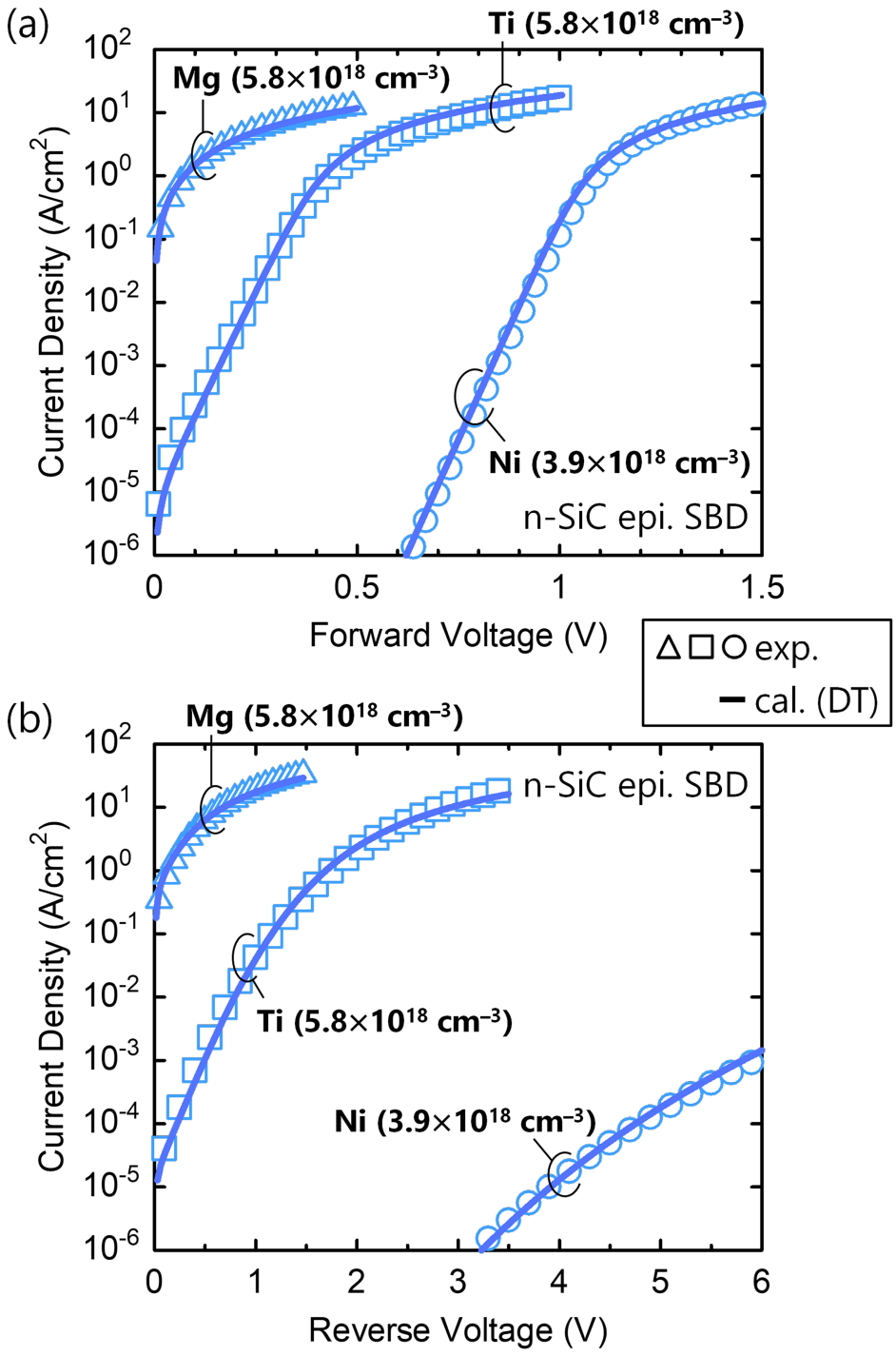

Figure 3.4: (a) Forward and (b) reverse I–V characteristics of the Ni, Ti, and Mg Schottky structures formed on heavily-doped n-type SiC epitaxial layers with a similar N_{d} (4–6 $\times$ $10^{18}\,\mathrm{cm}^{-3}$).

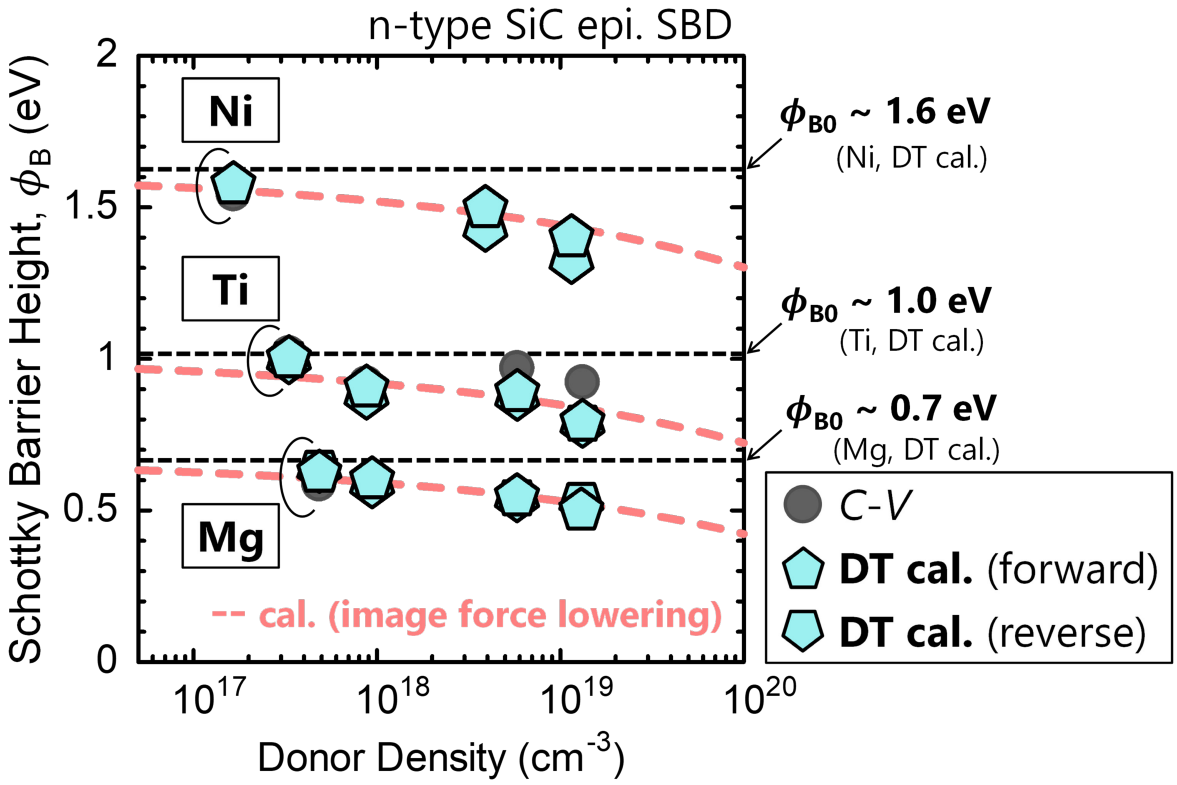

Figure 3.5: Donor density dependence of the barrier height at zero bias (ϕ_B) of the Ni/, Ti/, and Mg/SiC SBDs obtained from C–V measurement and numerical analysis of the forward and reverse DT current.

for the forward and reverse I–V characteristics give consistent ϕ_{B}, and the ϕ_{B} drop with increasing N_{d} is well described by the image force lowering, as indicated by the dashed lines. These results ensure the validity of the analysis based on the numerical calculation of the DT current.

3.5 Transition From Thermionic Field Emission to Field Emission

It is generally understood that the dominant carrier transport mechanism (TE, TFE, and FE) is almost uniquely determined with a given condition for the barrier height, temperature, and "electric field" [1, 5]. This concept is often relied on to predict the leakage current in SBDs. For instance, the reverse I–V characteristics in wide-bandgap (WBG) semiconductor-based power SBDs are described by the TFE model, as mentioned above. Hence, the TFE current and its dependency on the electric field, including the TE-TFE transition, have been analyzed for SBDs fabricated with lightly-doped WBG semiconductors [5, 9]. These analyses provide a practical design criterion for WBG semiconductor-based power SBDs (junction barrier Schottky diodes), which is how low the interface electric field should be suppressed to avoid a considerable leakage current [10].

This section focuses on the dominant carrier transport mechanism in heavily-doped SiC SBDs, in which a much higher electric field exists than lightly-doped SiC SBDs, and mainly discusses the electric field-dependent TFE-FE transition.

3.5.1 Critical Electric Field

As explained in Sect. 3.2, the numerical formula of the DT current includes both the TFE and FE transport, and they are distinguished by investigating E_{peak}, which is the energy giving a peak value of $J(E)$. The peak value of $J(E)$ is explored to find E_{peak} at each V from the calculated DT current, and $E_{\mathrm{peak}} - E_{\mathrm{C}}$ (forward bias) or $E_{\mathrm{peak}} - E_{\mathrm{Fm}}$ (reverse bias) in the Ti/heavily-doped SiC SBDs ($N_{\mathrm{d}} = 6 \times 10^{18}$ and $1 \times 10^{19}\,\mathrm{cm}^{-3}$) is plotted against V as triangular symbols in Fig. 3.6. Figure 3.6 also shows the corresponding I–V curves from the experiment (square symbols) and calculation (solid lines). In the case of the forward I–V characteristics, E_{peak} is kept higher than E_{C} in the entire voltage range measured, indicating that the TFE model describes the carrier transport in forward-biased heavily-doped SiC SBDs. This result supports the validity of adopting the analytical formula of the TFE transport to the barrier height extraction from forward I–V characteristics in heavily-doped SiC SBDs, described in Chap. 2. Under a reverse bias, on the other hand, E_{peak} rapidly decreases with a larger applied voltage and approaches E_{Fm}, reflecting the transition of the dominant tunneling process from the TFE to FE caused by a higher electric field.

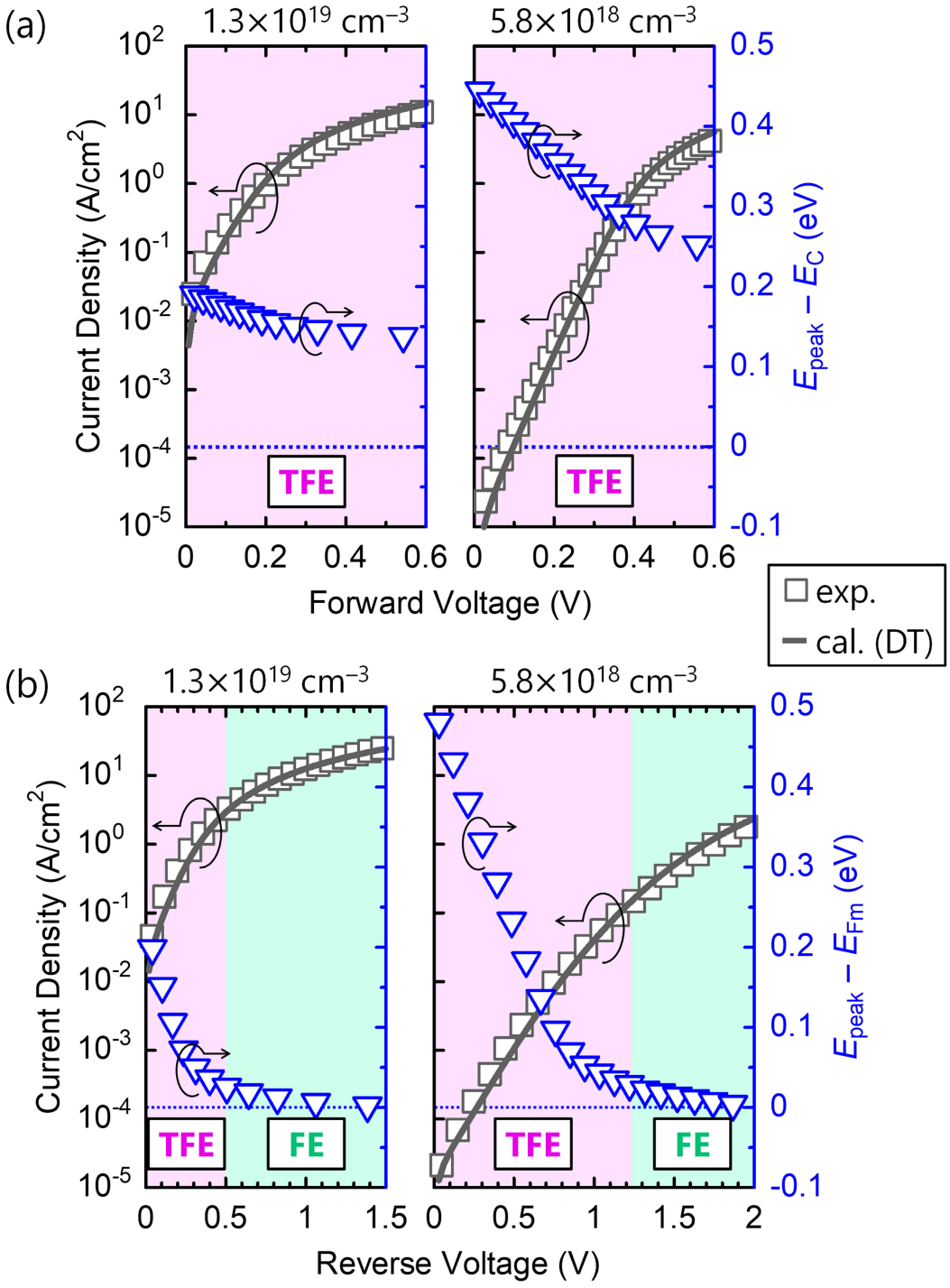

Figure 3.6: Energy where the electron tunneling most frequently occurs (defined as E_{peak}) as a function of the applied voltage in the Ti/SiC SBDs ($N_{\mathrm{d}} = 1 \times 10^{19}$ and $6 \times 10^{18}\,\mathrm{cm}^{-3}$) under (a) forward and (b) reverse biases. The corresponding I–V characteristics (experiment and DT calculation) are also shown.

The critical electric field for the TFE-FE transition is then discussed. In this study, the boundary energy for $E_{\rm peak}$ to judge the dominant contribution of FE is defined as $E_{\rm Fm} + k_{\rm B}T$ ($E_{\rm Fm} + 26\,{\rm meV}$ at room temperature). Since the analysis of the electric field dependence of the tunneling current has conventionally been performed using the maximum electric field at a Schottky interface ($F_{\rm max}$) [10, 11], the author first extracted $F_{\rm max}$ at the TFE-FE transition. As a result, the critical $F_{\rm max}$ is dependent on $N_{\rm d}$ and obtained to be $2.5\,{\rm MV/cm}$ for $N_{\rm d} = 1 \times 10^{19}\,{\rm cm^{-3}}$ and $2.1\,{\rm MV/cm}$ for $N_{\rm d} = 6 \times 10^{18}\,{\rm cm^{-3}}$, respectively. The $N_{\rm d}$-dependent critical electric field seems inconsistent with the fact that the dominant tunneling process is almost uniquely determined by the electric field. Therefore, the author carefully considers which "electric field" should be used in discussing the TFE-FE transition in the case of high doping densities.

Figure 3.7 depicts the energy potential and the electric field distribution in the depletion region of the heavily-doped SiC SBDs ($N_{\rm d} = 1 \times 10^{19}$ and $6 \times 10^{18}\,{\rm cm^{-3}}$) under the reverse bias at the TFE-FE boundary ($E_{\rm peak} \simeq E_{\rm Fm}$). As $N_{\rm d}$ becomes high, the electric field distribution exhibits a steeper slope, and the electric field value rapidly decreases within a short distance. Hence, especially in the case of a high $N_{\rm d}$, electrons having a different energy should feel a very different electric field, sensitively depending on their energy. In this sense, it is expected that the electric field at the energy of $E_{\rm peak}$ (defined as $F_{\rm peak}$) can precisely express the "electric field for most electrons." In fact, the electric field at the energy of $E_{\rm Fm}$, where electron tunneling mainly occurs at the TFE-FE transition, is found to be almost identical regardless of $N_{\rm d}$, as depicted in Fig. 3.7. Therefore, the author tries to analyze the TFE-FE transition in heavily-doped SiC Schottky structures based on $F_{\rm peak}$ instead of $F_{\rm max}$.

Figure 3.8 compares the correlation between $E_{\rm peak} - E_{\rm Fm}$ and (a) $F_{\rm max}$ or (b) $F_{\rm peak}$ in the Ti/heavily-doped SiC SBDs ($N_{\rm d} = 4 \times 10^{17}$–$1 \times 10^{19}\,{\rm cm^{-3}}$) under a reverse bias condition. Although the critical electric field for the TFE-FE transition (i.e., $E_{\rm peak} \simeq E_{\rm Fm}$) is not uniquely determined among different doping densities when using $F_{\rm max}$, the $F_{\rm peak}$ value at the TFE-FE transition is almost identically obtained in a wide $N_{\rm d}$ range. In the case of the Ti/n-type SiC Schottky structure with $\phi_{\rm B0} \simeq 1.0\,{\rm eV}$, as a result, it is determined that the dominant tunneling process changes from TFE to FE when $F_{\rm peak}$ at the energy of $E_{\rm Fm}$ exceeds about $1.5\,{\rm MV/cm}$, as seen in Fig. 3.8(b). Note that $F_{\rm peak}$-based analysis gives a unique critical condition for the TFE-FE transition regardless of the Schottky electrode. Figure 3.9 extracts the critical electric field for the TFE-FE transition (i.e., $F_{\rm peak}$ at $E_{\rm Fm}$) as a function of $\phi_{\rm B0}$. It is confirmed that the TFE-FE transition occurs under a lower $F_{\rm peak}$ when a Schottky electrode with a lower $\phi_{\rm B0}$ is employed. Consequently, a new concept is established to discuss the dominant tunneling mechanism and transition between TFE and FE models regarding the electric field dependence for Schottky contacts formed on heavily-doped semiconductors.

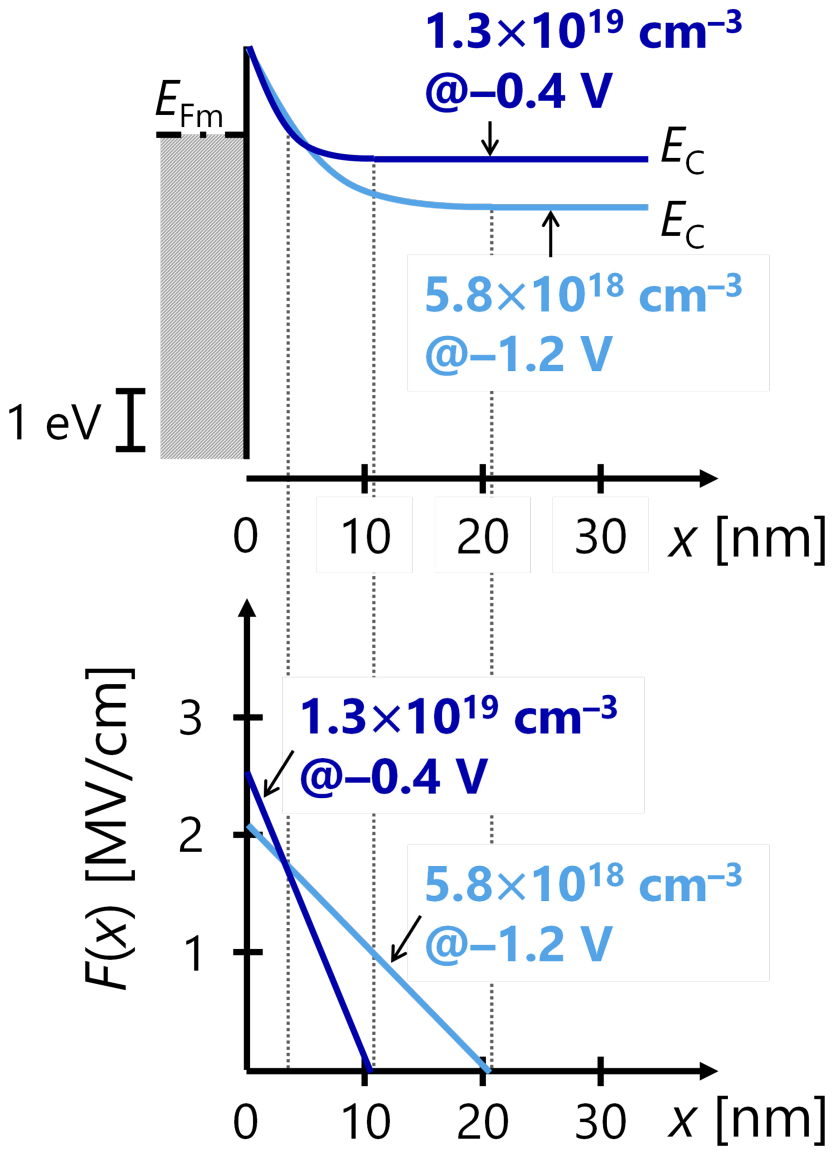

Figure 3.7: Energy band diagram and electric field distribution in the depletion region near the Ti/SiC Schottky interface ($N_{\mathrm{d}} = 1 \times 10^{19}$ and $6 \times 10^{18}\,\mathrm{cm}^{-3}$) under the reverse bias condition of the TFE-FE transition.

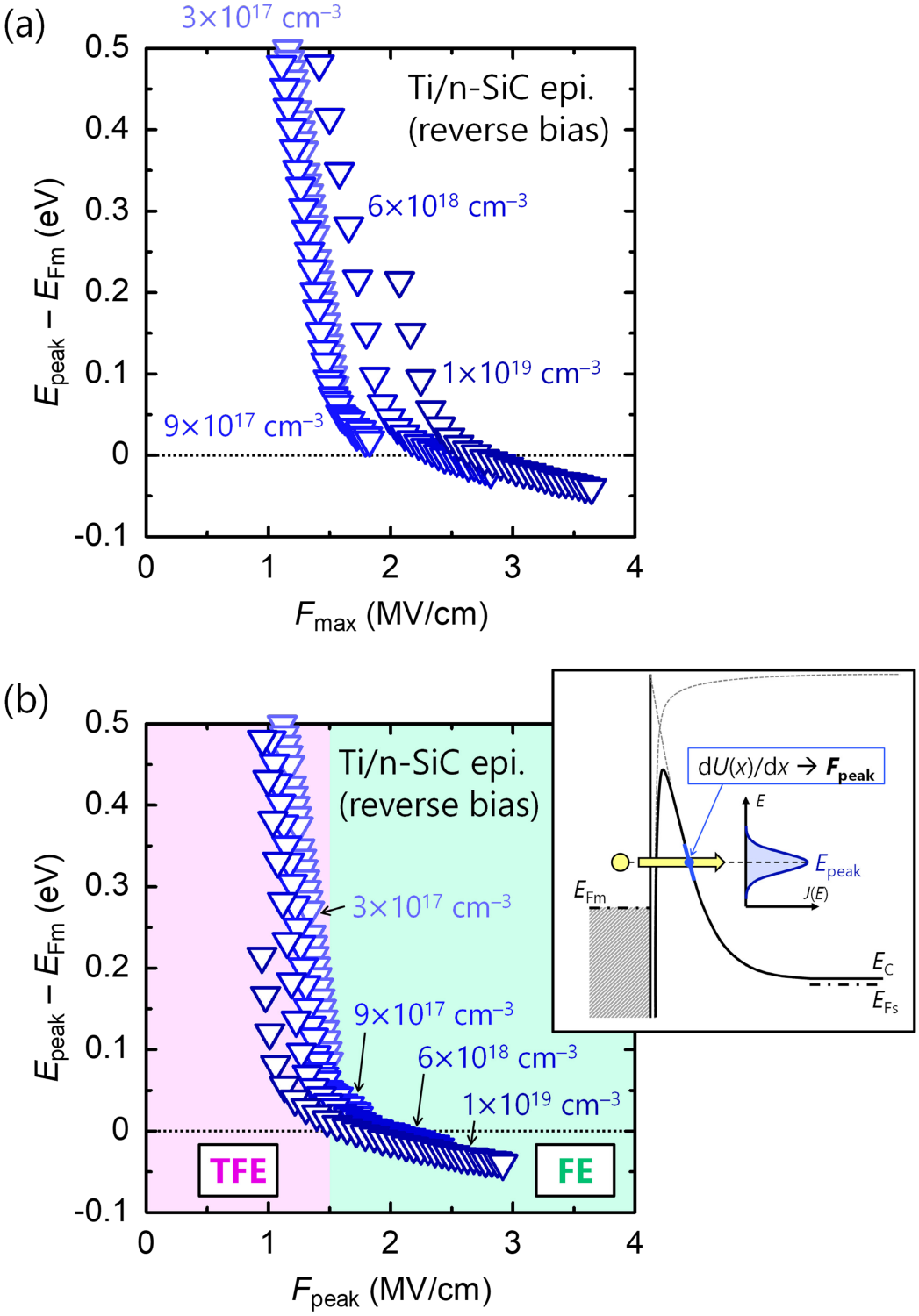

Figure 3.8: Correlation between E_{peak} and (a) the maximum electric field at the Schottky interface (F_{max}) and (b) the electric field at the energy of E_{peak} (defined as F_{peak}) in the reverse-biased Ti/n-type SiC SBDs with various N_{d} (3×10^{17}–$1 \times 10^{19}\,\mathrm{cm}^{-3}$).

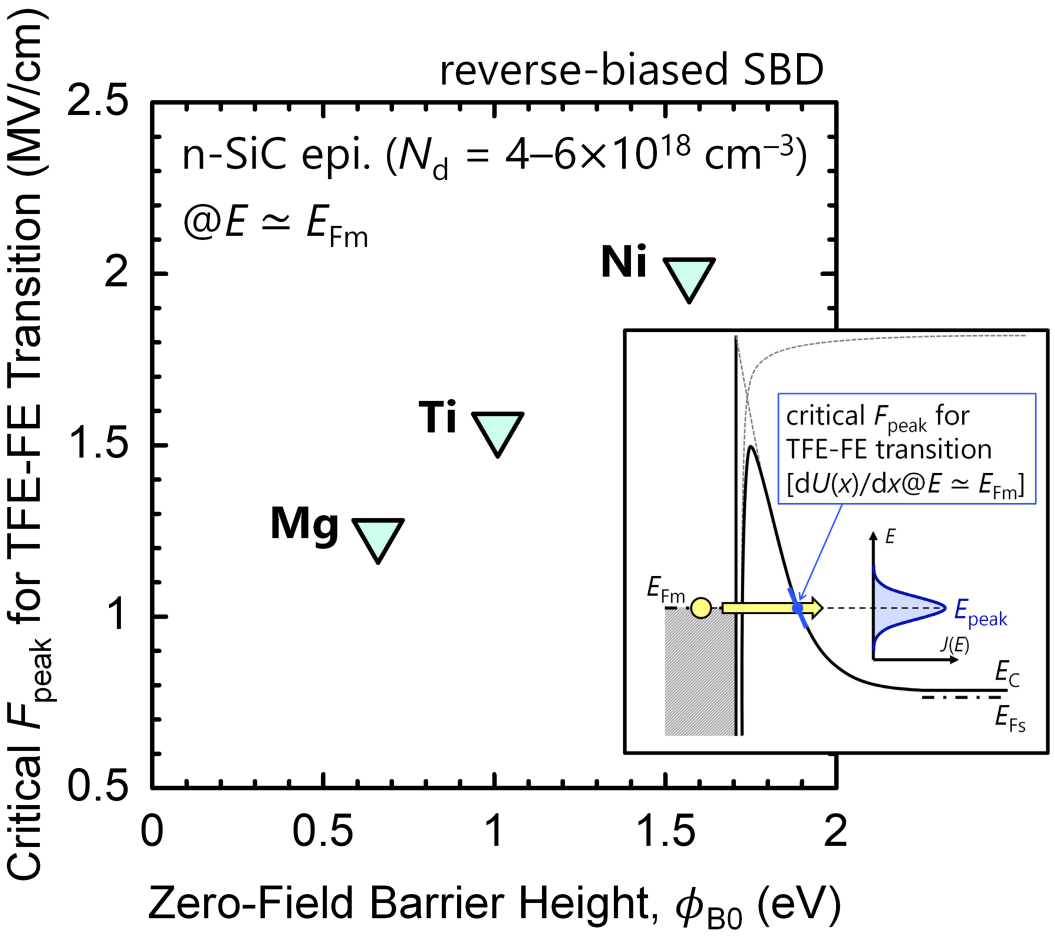

Figure 3.9: Critical electric field (F_{peak}) for the TFE-FE transition (i.e., $E_{\mathrm{peak}} \simeq E_{\mathrm{Fm}}$) versus the zero-field barrier height (ϕ_{B0}) for the reverse-biased n-type SiC SBDs.

3.5.2 Critical Barrier Thickness

The former section correlated the TFE-FE transition with the "electric field" in the same manner conventionally adopted for lightly-doped semiconductors. More fundamentally, on the other hand, tunneling phenomena should be discussed based on the barrier thickness (or the tunneling distance) that directly determines the tunneling probability. In the case of low doping density, for which the electric field distribution in the depletion region can be regarded as constant ($F_{\max}$) and energy potential can be approximated as triangular-shaped near the Schottky interface, there is a one-to-one relationship between the barrier thickness and $F_{\max}$. This assumption is no longer valid for heavily-doped semiconductors, and the barrier thickness has to be obtained directly from the energy potential, $U(x)$, which is the essential reason for the inapplicability of the $F_{\max}$-based analysis.

Since the dominant tunneling process changes from TFE to FE when a sufficiently thin barrier thickness at E_{Fm} is ensured, the TFE-FE transition is expected to be uniquely related to the barrier thickness at $E_{\mathrm{peak}} \simeq E_{\mathrm{Fm}}$. Furthermore, it is even predicted that the critical barrier thickness can be determined irrespective of the barrier height, which is different from the electric-field-based discussion. Figure 3.10(a) plots the E_{peak} values against the barrier thickness for electrons having the energy of E_{peak}. The barrier thickness at the TFE-FE transition (i.e., the barrier thickness at $E_{\mathrm{peak}} \simeq E_{\mathrm{Fm}}$) is obtained to be about 5 nm for the Ti/n-type SiC Schottky structure, almost regardless of N_{d}. Besides, although there is a weak ϕ_{B0} dependence, the critical barrier thickness at E_{Fm} for the TFE-FE transition is nearly identically determined to be about 4–7 nm for each ϕ_{B0}, as shown in Fig. 3.10(b). Since the barrier thickness can be easily obtained from $U(x)$ under a given bias condition, the critical value presented above is more helpful in identifying the dominant DT process. Considering the thermal effect on the carrier distribution, the critical condition varies strongly depending on the temperature, which has to be carefully studied in the future.

3.6 Discussion

The author first emphasizes the necessity of the numerical analysis for the carrier transport characteristics in heavily-doped SiC Schottky structures, especially under a reverse bias condition. Figure 3.11 shows the reverse I–V characteristics of the Ti/heavily-doped SiC SBDs ($N_{\mathrm{d}} = 6\times10^{18}\,\mathrm{cm}^{-3}$). The symbols give the experimental data, and the pink and green solid lines are calculated from analytical formulas for the TFE and FE models, respectively, which are expressed as [2],

$$J_{\mathrm{TFE,R}} = \frac{A^{*}T}{k_{\mathrm{B}}}\sqrt{\pi E_{00}\left\{eV_{\mathrm{R}} + \frac{\phi_{\mathrm{B}}}{\cosh^{2}(E_{00}/k_{\mathrm{B}}T)}\right\}}\exp\left(-\frac{\phi_{\mathrm{B}}}{E_{0}}\right)\exp\left(\frac{eV_{\mathrm{R}}}{E'}\right), \tag{3.7}$$

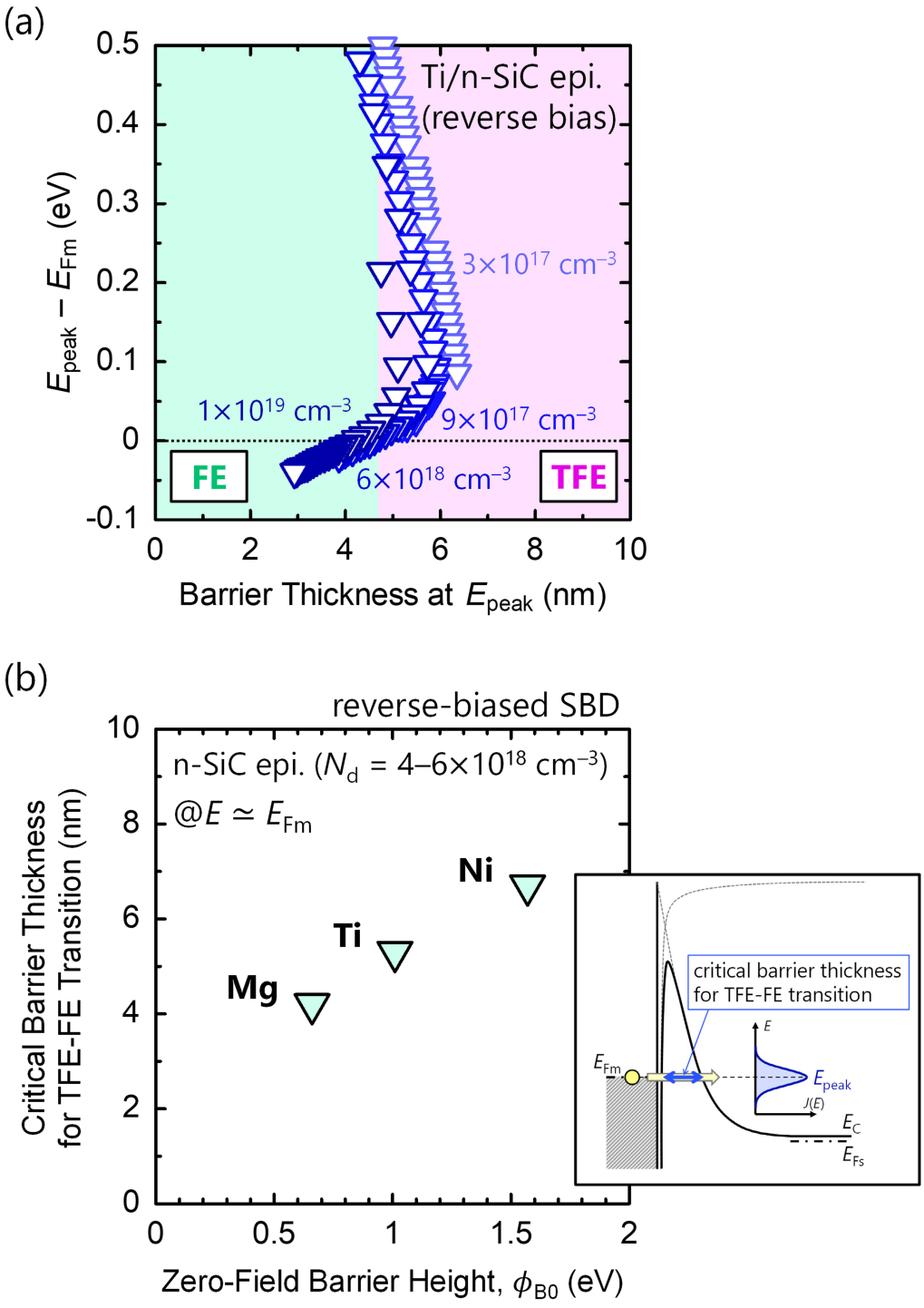

Figure 3.10: (a) Correlation between E_{peak} and barrier thickness at the energy of E_{peak} in the reverse-biased Ti/n-type SiC SBDs with various N_{d} (3×10^{17}–$1 \times 10^{19}\,\mathrm{cm}^{-3}$). (b) Critical barrier thickness for the TFE-FE transition (i.e., barrier thickness at E_{Fm}) as a function of the zero-field barrier height (ϕ_{B0}) in the reverse-biased n-type SiC SBDs.

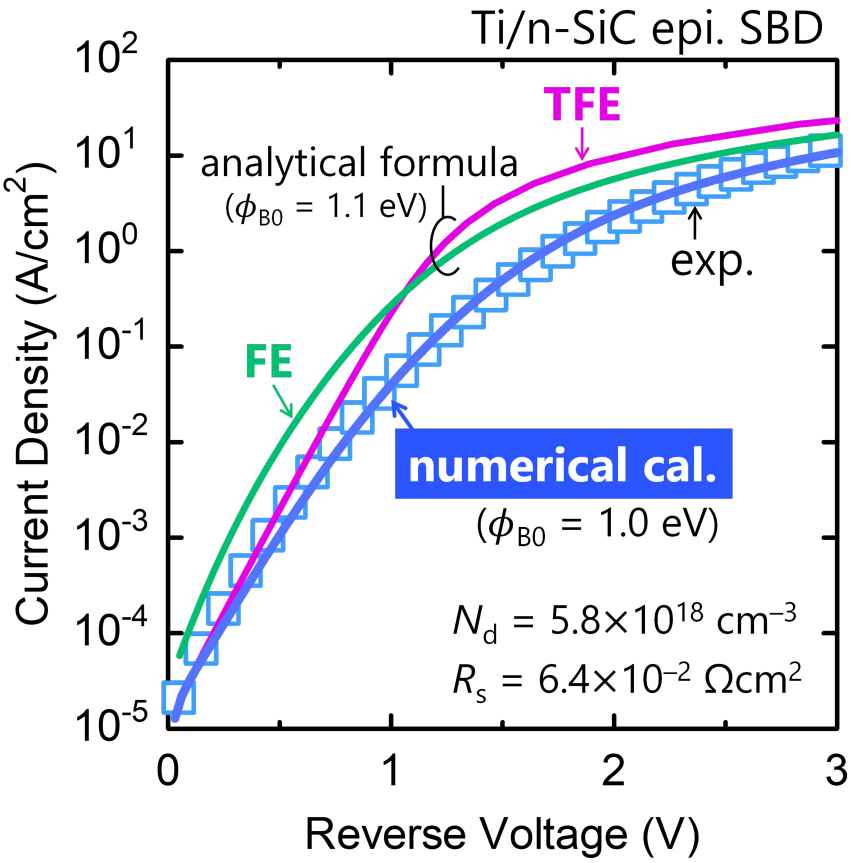

Figure 3.11: Reverse I–V characteristics of the Ti/SiC SBDs ($N_d = 6 \times 10^{18}\,\mathrm{cm}^{-3}$) obtained from the experiment, TFE- and FE-based calculations with the analytical model, and numerical calculation of the DT current.

$$J_{\mathrm{FE,R}} = A^* \left(\frac{E_{00}}{k_{\mathrm{B}}}\right)^2 \left(\frac{\phi_{\mathrm{B}} + eV_{\mathrm{R}}}{\phi_{\mathrm{B}}}\right) \exp\left(-\frac{2\phi_{\mathrm{B}}^{3/2}}{3E_{00}\sqrt{\phi_{\mathrm{B}} + eV_{\mathrm{R}}}}\right), \tag{3.8}$$

$$E_{00} = \frac{e\hbar}{2}\sqrt{\frac{N_{\mathrm{d}}}{m^*\varepsilon_{\mathrm{s}}}}, \quad E_0 = E_{00}\coth\left(\frac{E_{00}}{k_{\mathrm{B}}T}\right), \quad E' = \frac{E_{00}}{(E_{00}/k_{\mathrm{B}}T) - \tanh(E_{00}/k_{\mathrm{B}}T)}, \tag{3.9}$$

where V_{R} is the reverse bias voltage and ϕ_{B} is the barrier height including the image force effect ($\phi_{\mathrm{B0}} - \Delta\phi$), respectively. The blue solid line shows the numerical calculation result. As seen in Fig. 3.11, it is difficult to reproduce the experimental I–V characteristics in a reverse-biased heavily-doped SiC SBD by the calculation assuming only one type of tunneling process (TFE or FE). This is due to a continuous change in the dominant tunneling process, which is very sensitive to the following factors: doping density, barrier height, applied voltage, electric field, and measurement temperature. This aspect is significant when calculating ρ_{c} at ohmic contacts with the analytical models of TFE and FE transport [12]. In other words, in the ρ_{c} analysis at ohmic contacts, one has to pay attention to whether TFE or FE is valid near 0 V under a given condition (e.g., doping density and barrier height) and judge which models of TFE and FE should be adopted. Therefore, in order to avoid ambiguity in choosing an appropriate tunneling model, it is preferable to conduct the numerical calculation and extract ρ_{c} from the calculated J_{DT}–V characteristics.

The author also introduces a unique tunneling phenomenon at metal/heavily-doped p-type SiC Schottky interfaces ascribed to the complicated valence band structure in SiC, recently reported by Kitawaki *et al.* [13]. Figure 3.12(a) shows the computed E–k dispersion in the valence band of SiC along ⟨0001⟩ [14], where E is the hole energy and k is the wavenumber, respectively. The valence band in SiC comprises three different bands: two almost degenerated topmost bands (heavy- and light-hole bands) with the effective mass of $1.6m_0$ and a split-off band located at the energy about 60 meV higher than the two bands. Notably, the effective mass of the split-off band holes is very light along the c-axis ($0.21m_0$), which is about one-eighth of that near the valence band edge (E_{V}). Since the effective mass of a carrier exponentially contributes to the tunneling probability, as seen in Eq. (3.2), tunneling from or to the split-off band can become predominant rather than the topmost bands, as depicted in Fig. 3.12(b). The symbols in Fig. 3.13 show the experimental (a) forward and (b) reverse I–V characteristics of the vertical Ni/p-type SiC SBDs fabricated on aluminum-doped SiC epitaxial layers (net acceptor density: 4×10^{18} and $3\times10^{19}\,\mathrm{cm}^{-3}$) grown on p-type 4H-SiC(0001) substrates [13]. Considering only the topmost bands (black lines), the calculated DT current largely deviates from the experimental data for each case. On the other hand, by taking account of all the bands, including the split-off band, the experimental forward and reverse I–V curves are well reproduced by the DT current calculation (orange solid lines). As a result, it turned out that tunneling of the holes in the split-off band with the light effective mass ($0.21m_0$) is the dominant conduction mechanism in heavily-doped p-type SiC Schottky structures. Although a high Schottky barrier is generally formed on p-type SiC due to its large work function, the contribution of

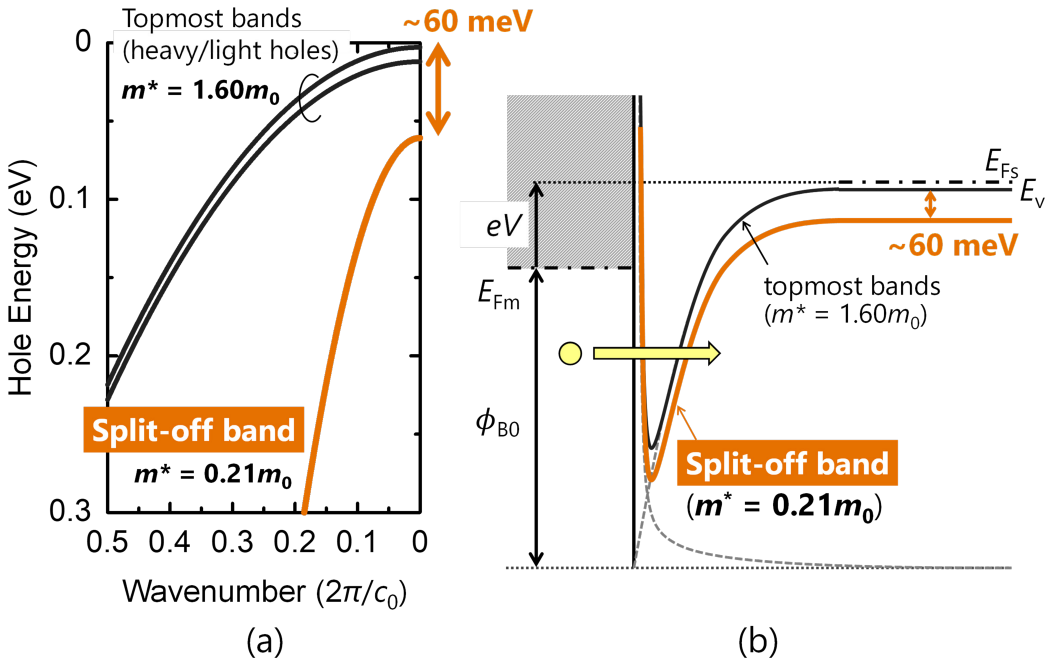

Figure 3.12: (a) Calculated E–k dispersion of the valence band of SiC along $\langle 0001 \rangle$ [14]. (b) Schematic illustration of the hole tunneling to the split-off band having a light effective mass ($0.21m_0$).

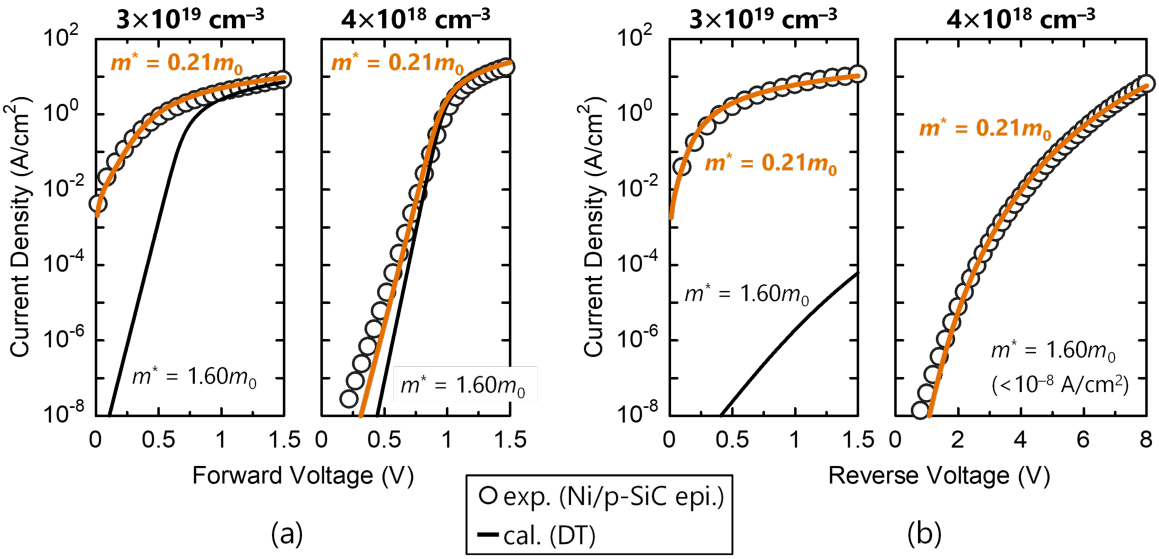

Figure 3.13: (a) Forward and (b) reverse I–V characteristics of the Ni/p-SiC SBDs fabricated on heavily-doped p-type SiC epitaxial layers (4×10^{18} and $3 \times 10^{19}\,\mathrm{cm}^{-3}$) [13]. The calculated DT current, including the split-off band holes with $m^* = 0.21m_0$ (orange lines), reproduces the experimental data (symbols) well, while the calculation only with the topmost band holes with $m^* = 1.60m_0$ (black lines) does not.

the split-off band, which makes the tunneling current larger than that expected only from E_V, can be an advantageous property toward the ρ_c reduction at p-type SiC ohmic contacts.

The author finally comments on the significance of investigating the temperature dependence of the DT current. Section 3.5 extensively discussed a change in the dominant tunneling process (TFE or FE) depending on the electric field or the barrier thickness that correlates with the tunneling probability. Since the ambient temperature directly determines the energy distribution of carriers, which is the other fundamental component in tunneling phenomena, clarifying temperature-dependent changes in the critical conditions for the TFE-FE transition is also crucial, as several times mentioned above. Regarding practical ohmic contacts, the temperature dependence of ρ_c, which is strongly influenced by the carrier transport mechanism, is a vital electrical characteristic to discuss the barrier height at the interface and investigate the thermal stability of the ohmic contact. Especially for p-type SiC Schottky structures, the decreased number of thermal holes in the split-off band should critically affect the tunneling current, which is both a scientifically and practically significant research subject. Therefore, through systematic experiment and numerical calculation, it is indispensable to perform full modeling of the DT phenomenon concerning the dependency on the electric field, barrier height, and temperature.

3.7 Summary

In this chapter, the DT phenomena, including both the TFE and FE, in Schottky structures formed on heavily-doped SiC epitaxial layers were analyzed in detail with various N_d, ϕ_{B0}, and applied voltage conditions. The forward and reverse I–V characteristics of the heavily-doped SiC SBDs ($N_d > 10^{17}\,\mathrm{cm}^{-3}$) were well reproduced with the numerical calculation of the DT current, which could not be reproduced for all the cases when adopting the analytical formulas of TFE or FE, indicating the transition of the dominant tunneling process in the heavily-doped SiC SBDs. Investigation of the energy where the electron tunneling most frequently occurs (defined as E_{peak}) revealed which of the TFE or FE is predominant under a given condition, that is, the carrier transport is dominated by TFE in forward-biased heavily-doped SiC SBDs ($N_d > 10^{17}\,\mathrm{cm}^{-3}$), while, under a reverse bias, a higher electric field in heavily-doped SiC SBDs (N_d above mid-$10^{18}\,\mathrm{cm}^{-3}$) leads to TFE-FE transition. Focusing on sharply changing electric field distribution in heavily-doped SiC Schottky structures, a novel concept to analyze the electric field-dependent TFE-FE transition, which utilizes the electric field at the energy of E_{peak} (defined as F_{peak}), was established. Besides, standing on a more fundamental aspect that the tunneling probability is directly determined from the barrier thickness, the critical condition for the TFE-FE transition at metal/heavily-doped SiC Schottky interfaces was clarified regardless of N_d and ϕ_{B0}: the dominant tunneling process changes from TFE to FE when the barrier thickness at E_{Fm} becomes less than about 4–7 nm.

A deep understanding of the tunneling phenomena at non-alloyed contacts on heavily-doped SiC should give an essential starting point toward clarifying the mechanism of ohmic contact formation and establishing a low-temperature fabrication process for low-resistance SiC ohmic contacts. Furthermore, the high-field tunneling current is expected to be commonly observed in Schottky structures on other WBG semiconductor materials. Hence, the present data and proposed concept will also help develop ohmic contacts on them.

References

[1] E. L. Murphy and R. H. Good, *Phys. Rev.* **102**, 1464 (1956).

[2] F. A. Padovani and R. Stratton, *Solid State Electron.* **9**, 695 (1966).

[3] R. Stratton, *J. Phys. Chem. Solids* **23**, 1177 (1962).

[4] W. A. Harrison, *Phys. Rev.* **123**, 85 (1961).

[5] T. Hatakeyama and T. Shinohe, *Mater. Sci. Forum* **389–393**, 1169 (2002).

[6] T. Kimoto and J. A. Cooper, *Fundamentals of Silicon Carbide Technology: Growth, Characterization, Devices and Applications* (John Wiley & Sons, 2014).

[7] D. Volm, B. K. Meyer, D. M. Hofmann, W. M. Chen, N. T. Son, C. Persson, U. Lindefelt, O. Kordina, E. Sörman, A. O. Konstantinov, B. Monemar, and E. Janzén, *Phys. Rev. B* **53**, 15409 (1996).

[8] S. M. Sze, Y. Li, and K. K. Ng, *Physics of Semiconductor Devices* (John Wiley & Sons, 4th edition, 2021).

[9] W. Li, D. Jena, and H. G. Xing, *J. Appl. Phys.* **131**, 015702 (2022).

[10] T. Kimoto and H. Watanabe, *Appl. Phys. Express* **13**, 120101 (2020).

[11] W. Li, D. Saraswat, Y. Long, K. Nomoto, D. Jena, and H. G. Xing, *Appl. Phys. Lett.* **116**, 192101 (2020).

[12] A. Y. C. Yu, *Solid State Electron.* **13**, 239 (1970).

[13] T. Kitawaki, M. Hara, H. Tanaka, M. Kaneko, and T. Kimoto, *Appl. Phys. Express* **16**, 031005 (2023).

[14] H. Tanaka, S. Asada, T. Kimoto, and J. Suda, *J. Appl. Phys.* **123**, 245704 (2018).

Chapter 4

Trap-Assisted Tunneling Through Schottky Contacts on Heavily-Doped *n*-Type SiC Induced by Phosphorus Ion Implantation

4.1 Introduction

Chapter 3 revealed that the carrier transport at Schottky contacts formed on heavily-doped SiC epitaxial layers is described by the direct tunneling (DT) model, which includes both the thermionic field emission (TFE) and field emission (FE). As a next step from an epitaxial layer, this chapter then investigates the carrier transport characteristics at Schottky contacts formed on high-dose ion-implanted SiC because ohmic contacts in real devices (e.g., source and body contacts in SiC power MOSFETs) are often formed on heavily ion-implanted SiC with a doping density above $10^{19}\,\mathrm{cm}^{-3}$.

To form a heavily-doped n-type SiC region, phosphorus ion (P^+) implantation is generally adopted because of the high solubility limit of P atoms in SiC ($\sim 10^{21}\,\mathrm{cm}^{-3}$) [1], allowing to achieve a higher doping density than nitrogen (N) doping through both epitaxial growth and implantation [2, 3]. Although it is qualitatively expected that a higher doping density in a P^+-implanted region leads to a larger tunneling current, no reports quantitatively compare current–voltage (I–V) characteristics at contacts formed on heavily-doped epitaxial and ion-implanted layers. In addition to the carrier transport characteristics, other fundamental electrical properties, such as the net donor density (N_d) in P^+-implanted region and the barrier height at metal/P^+-implanted SiC interfaces, are also practically significant regarding the ohmic contact formation.

In this chapter, vertical Schottky barrier diode (SBD) structures are fabricated using P^+-implanted n-type SiC with various P atom densities (N_P). Then, electrical properties, including N_d in the implanted region, the barrier height at the contact, and the carrier

transport characteristics, are investigated in detail by comparing them with the contacts formed on N-doped epitaxial SiC.

4.2 Experiment

The starting material was N-doped n-type SiC (N density: $5 \times 10^{15}\,\mathrm{cm}^{-3}$) epitaxially grown on an n-type 4H-SiC(0001) substrate. P ions were implanted into the epitaxial layers to form box-shaped profiles with a wide-range of N_P: 1×10^{17}, 1×10^{18}, 5×10^{18}, 9×10^{18}, 3×10^{19}, and $8 \times 10^{19}\,\mathrm{cm}^{-3}$. The implant depth and temperature were 600 nm and room temperature for $N_\mathrm{P} \leq 9 \times 10^{18}\,\mathrm{cm}^{-3}$, while 200 nm and 500°C for $N_\mathrm{P} \geq 3 \times 10^{19}\,\mathrm{cm}^{-3}$. Activation annealing in Ar ambient was conducted at 1750°C for 20 min with a surface-protective carbon cap employed [3].

A schematic image of the fabricated vertical SBD structure is depicted in Fig. 4.1. Prior to the SBD fabrication, sacrificial oxidation was carried out at 1300°C for 60 min to remove the surface region in which the implantation profile was not precisely controlled to a constant. Oxide thickness monotonically increased with a higher N_P, as reported in the literature [4], and was measured to be 74–118 nm. Ni, Ti, and Mg were deposited on the implanted layers as Schottky electrodes via resistive heating evaporation. N_d in the P^+-implanted layers and the barrier height at the Schottky contacts were characterized by capacitance–voltage (C–V) measurement on the fabricated SBDs. Besides, I–V measurement was performed to investigate the carrier transport mechanism at metal/P^+-implanted SiC interfaces. Vertical SBDs were also fabricated using heavily N-doped SiC epitaxial layers with various N_d (10^{17}–$10^{19}\,\mathrm{cm}^{-3}$) for comparison, whose data are the same as those presented in the former chapter.

4.3 Net Donor Density and Barrier Height

The solid lines in Fig. 4.2(a) show the depth profiles of N_P measured by secondary ion mass spectrometry (SIMS). A gray color indicates the surface regions removed by sacrificial oxidation. The successful formation of P^+-implanted regions with a box-shaped profile is confirmed in a wide range of N_P. Figure 4.2(a) also plots N_d extracted from the C–V characteristics of the Ni/SiC SBDs as circles. The N_d profiles are nearly identical to those for N_P up to $3\times10^{19}\,\mathrm{cm}^{-3}$. Note that C–V measurement was hardly performed due to a significant tunneling current for $8 \times 10^{19}\,\mathrm{cm}^{-3}$. From the N_d versus N_P plot shown in Fig. 4.2(b), the activation ratio of the implanted P atoms is determined to be above 90%, even for a very high N_P of $3\times10^{19}\,\mathrm{cm}^{-3}$. Since C–V measurement is a powerful technique that can directly and precisely determine N_d without requiring any fitting parameters, the high activation ratio presented in this study strongly supports the successful formation of low-resistance n-type SiC layers by P^+ implantation reported based on Hall-effect measurement [2, 3, 5–7].

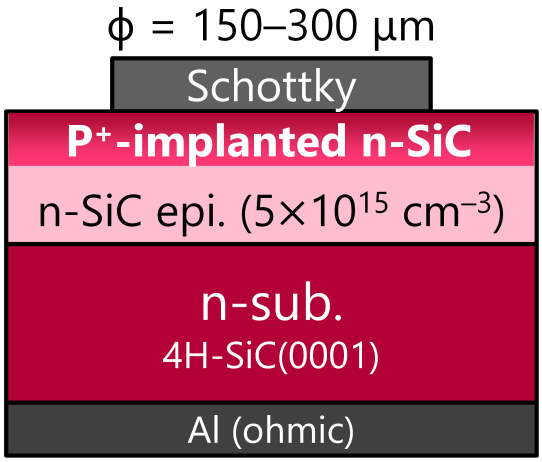

Figure 4.1: Schematic image of a vertical SBD structure fabricated on P^+-implanted n-type SiC.

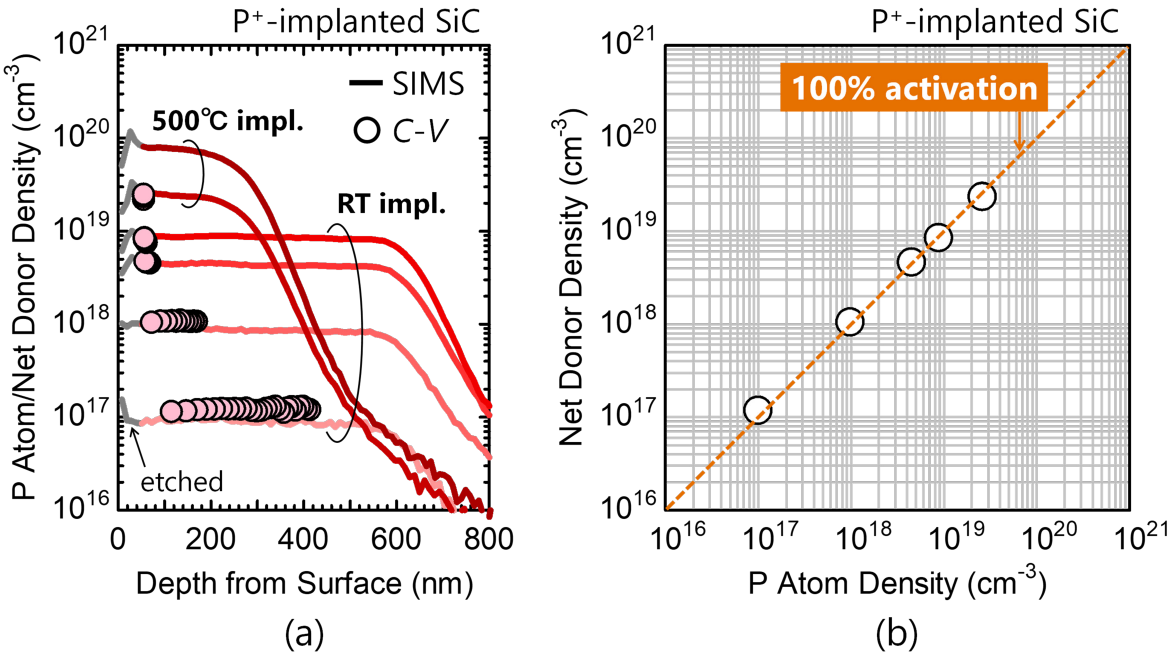

Figure 4.2: (a) Depth profiles of the implanted P atom and net donor densities in the P^+-implanted region characterized by SIMS and C–V measurements, respectively. (b) Net donor density versus implanted P atom density.

Figure 4.3 shows the N_d dependence of the zero-field barrier height (ϕ_{B0}) obtained from the C–V characteristics. Note that, as for the Mg/SiC SBDs fabricated on P^+-implanted layers, the current was too large to measure the capacitance even with a minimal bias voltage and accurately extract ϕ_{B0}. Regardless of the kind of Schottky electrodes, ϕ_{B0} is constantly obtained for each N_d: $\phi_{B0} \simeq 1.6\,\mathrm{eV}$ for the Ni/P^+-implanted SiC contacts and $\phi_{B0} \simeq 1.2\,\mathrm{eV}$ for the Ti contacts, respectively. Besides, the ϕ_{B0} values in the P^+-implanted SiC SBDs are almost the same as those in the epitaxial SiC SBDs, as indicated by blue symbols in Fig. 4.3. As a result, it is revealed that there are no factors to make a change in the barrier height only at metal/P^+-implanted SiC interfaces, and discussions on the barrier property at Schottky contacts on heavily-doped SiC epitaxial layers given in Chap. 2 are also adoptable to the case of P^+ implantation.

4.4 Current–Voltage Characteristics

Figure 4.4 shows the experimental (a) forward and (b) reverse I–V characteristics of the Ti/n-SiC SBDs fabricated using P^+-implanted SiC ($N_d = 1\times10^{18}$–$1\times10^{19}\,\mathrm{cm^{-3}}$) and epitaxial layers ($N_d = 9\times10^{17}$–$1\times10^{19}\,\mathrm{cm^{-3}}$). When comparing the I–V curves with a similar N_d (9×10^{17} and $1\times10^{18}\,\mathrm{cm^{-3}}$, 5×10^{18} and $6\times10^{18}\,\mathrm{cm^{-3}}$, and $1\times10^{19}\,\mathrm{cm^{-3}}$s, respectively), the current density in the P^+-implanted SiC SBDs is larger than in the epitaxial SiC SBDs, especially in a lower voltage range. A larger current is also observed in the P^+-implanted SiC SBDs fabricated with another Schottky electrode (Ni or Mg), as seen in the case of mid-$10^{18}\,\mathrm{cm^{-3}}$ shown in Fig. 4.5. As for the Mg/P^+-implanted SiC SBDs, the I–V curves are found to be independent of N_d when above $5\times10^{18}\,\mathrm{cm^{-3}}$, indicating a tiny voltage drop at the Schottky interface and dominant resistance components other than those at the contacts and in the implanted layers.

The author first tried to analyze these I–V characteristics based on the DT model described in Chap. 3. The red and blue symbols in Fig. 4.6 compare the I–V relationship in the Ti/n-SiC SBDs fabricated with P^+-implanted SiC ($N_d = 5\times10^{18}\,\mathrm{cm^{-3}}$) and epitaxially grown SiC ($N_d = 6\times10^{18}\,\mathrm{cm^{-3}}$), respectively. As depicted by the blue solid lines, the DT current calculated assuming $\phi_{B0} = 1.0\,\mathrm{eV}$ agrees well with the I–V characteristics of the epitaxial SiC SBD, while the same calculation hardly reproduces those in the implanted SiC SBD, despite similar N_d and ϕ_{B0} values. Almost identical N_d and ϕ_{B0} values should guarantee nearly the same thickness of the tunneling barrier and, thereby, the same tunneling probability and tunneling current. Therefore, it is considered that the DT process no longer describes the carrier transport in the P^+-implanted SiC SBDs, and the contribution of another conduction mechanism is responsible for the enhanced current density observed. In this sense, the author focuses on trap-assisted tunneling (TAT) through deep levels, created by a high-energy ion bombardment during the implantation [8–11], as the dominant conduction mechanism in the metal/P^+-implanted SiC Schottky structures.

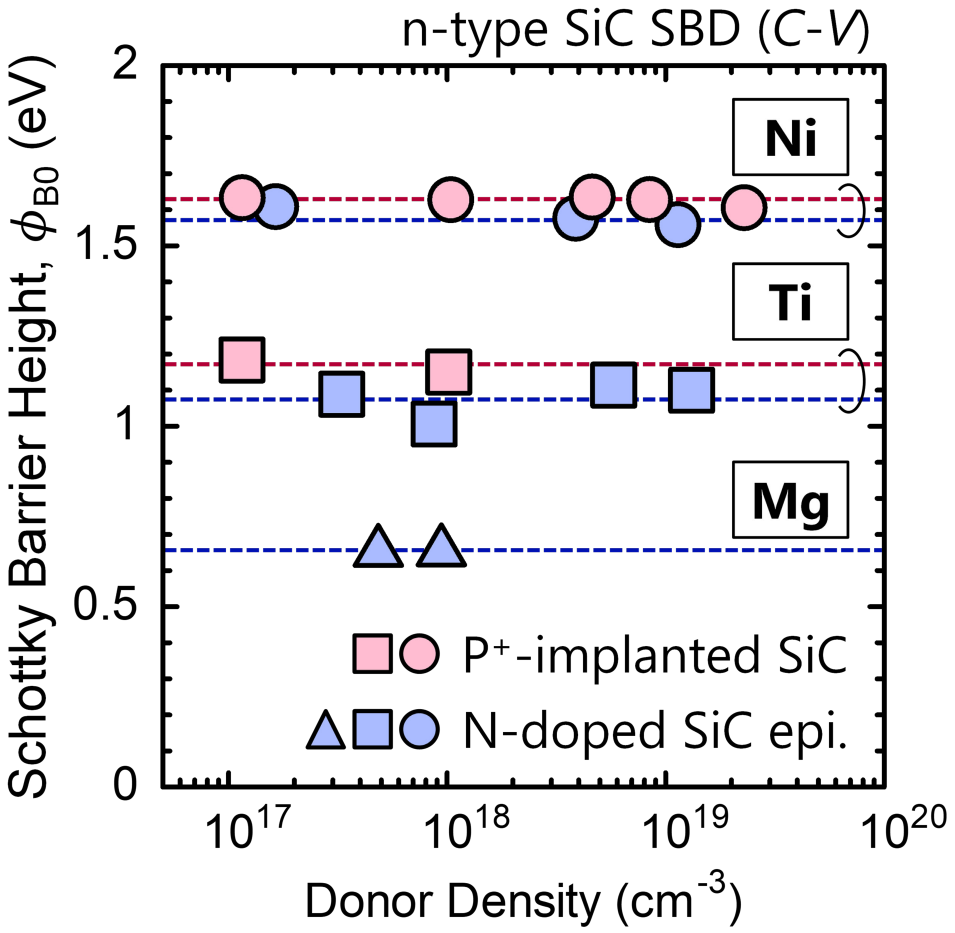

Figure 4.3: Donor density dependence of the zero-field barrier height (ϕ_{B0}) at Ni, Ti, and Mg Schottky contacts formed on P^+-implanted SiC and N-doped SiC epitaxial layer.

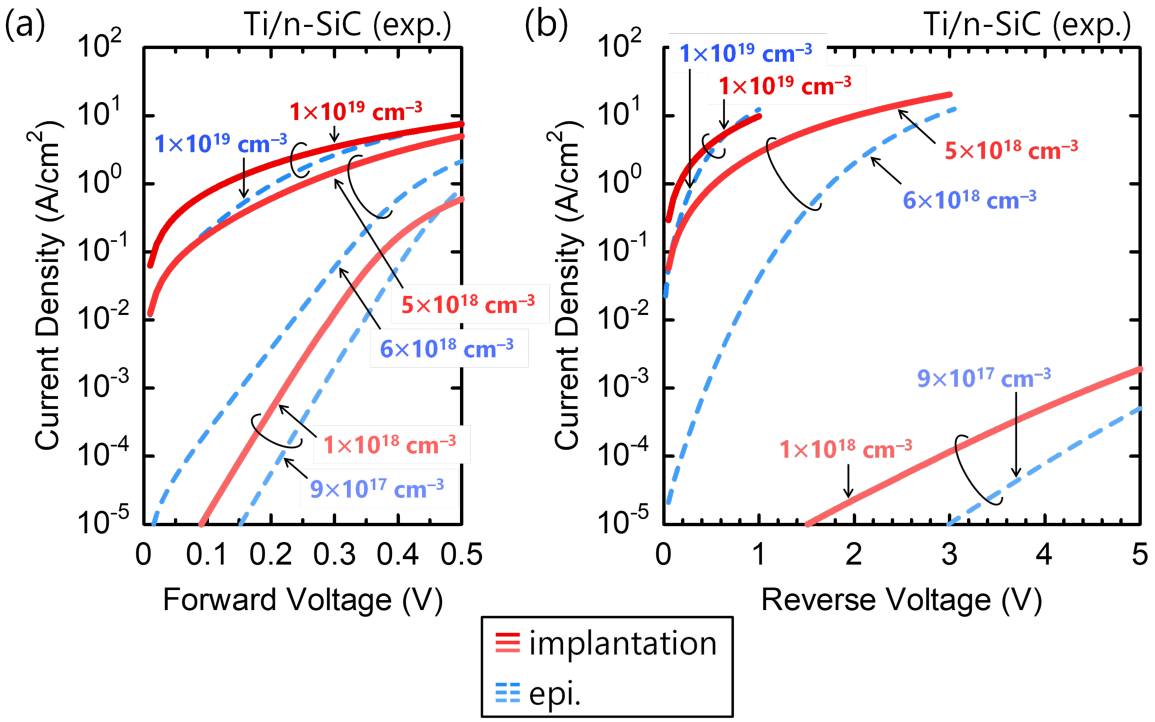

Figure 4.4: Experimental (a) forward and (b) reverse I–V characteristics of the Ti/n-SiC SBDs fabricated with P^+-implanted SiC ($N_d = 1 \times 10^{18}$–$1 \times 10^{19}\,cm^{-3}$) and N-doped SiC epitaxial layers ($N_d = 9 \times 10^{17}$–$1 \times 10^{19}\,cm^{-3}$).

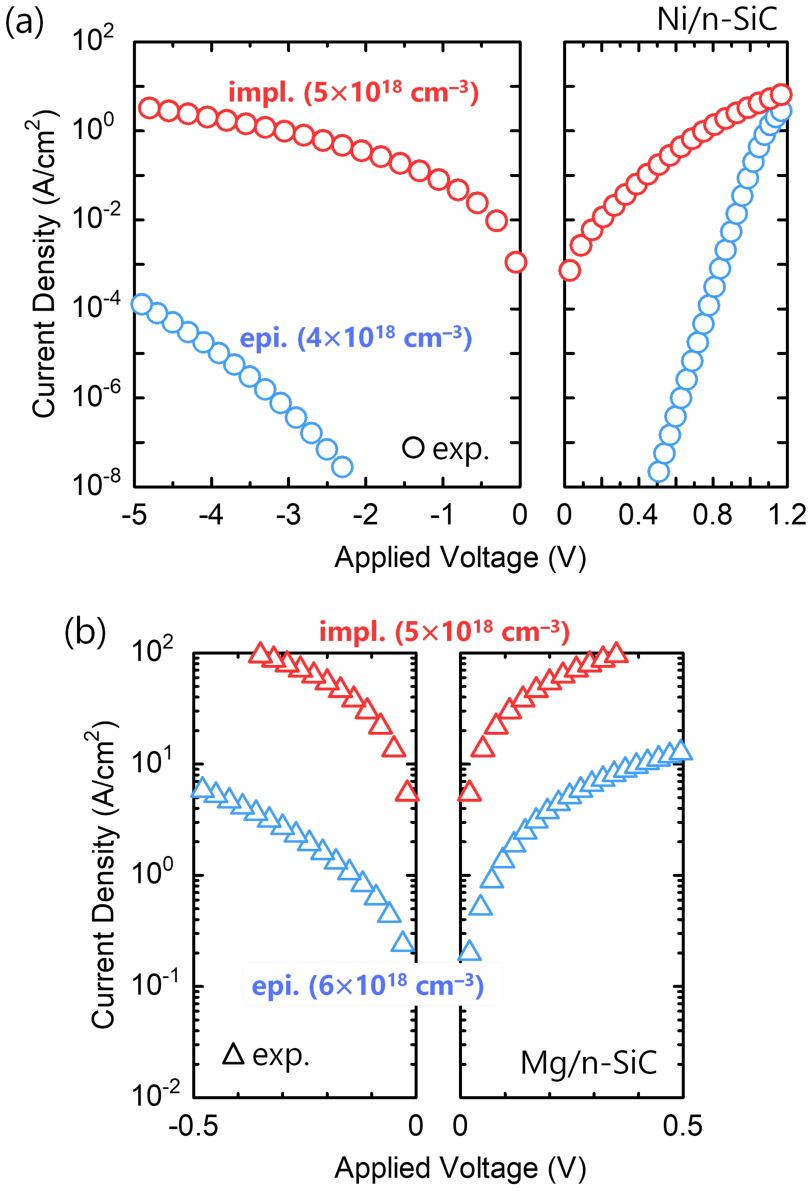

Figure 4.5: Experimental I–V characteristics of the (a) Ni/ and (b) Mg/n-SiC SBDs fabricated with P^+-implanted SiC ($N_d = 5 \times 10^{18}\,cm^{-3}$) and N-doped SiC epitaxial layers ($N_d = 4 \times 10^{18}$ or $6 \times 10^{18}\,cm^{-3}$).

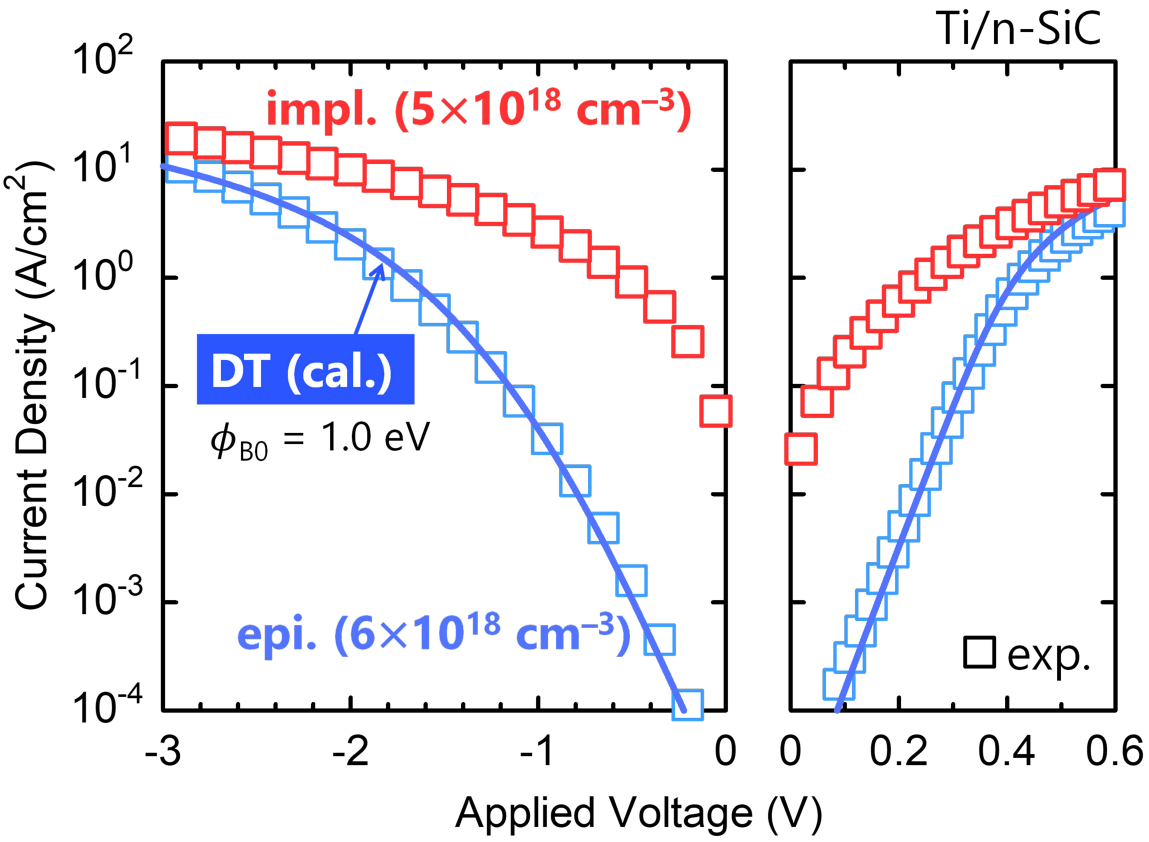

Figure 4.6: I–V characteristics of the Ti/n-SiC SBDs fabricated with P^+-implanted and epitaxial layers with nearly identical N_d (5×10^{18} or $6\times10^{18}\,cm^{-3}$, respectively). The square symbols represent experimental data, and the solid lines express the calculated DT current.

4.5 Enhanced Current by Trap-Assisted Tunneling

4.5.1 Numerical Formula

With the presence of a large amount of deep levels in the bandgap, TAT can be a dominant carrier transport mechanism [12]. In this conduction, carriers tunnel through a Schottky barrier via defect levels, as depicted in Fig. 4.7, through which the tunneling path is divided into two shorter paths, resulting in an enhanced tunneling probability compared to the DT process. The TAT probability [$P_{\mathrm{TAT}}(E)$] is derived by considering the equilibrium condition regarding the trap occupancy as [12–14],

$$P_{\mathrm{TAT}}(E) = N_{\mathrm{T}}\sigma_{\mathrm{T}}\frac{P_1(E)P_2(E)}{P_1(E)+P_2(E)}, \tag{4.1}$$

where N_{T} is the trap density (area density) and σ_{T} is the capture cross section of the trap for the tunneling carrier, respectively. $P_1(E)$ and $P_2(E)$ are the tunneling probabilities for the two paths, which are calculated by substituting x_{T} for x_{in} or x_{out} in Eq. (3.2), where x_{T} is the intersecting position of the carrier and trap, as illustrated in Fig. 4.7. Note that the former factor, $N_{\mathrm{T}}\sigma_{\mathrm{T}}$, is interpreted as how easily or frequently a tunneling carrier encounters a trap, and the latter factor gives the tunneling probability for a carrier passing through the trap. The TAT current (J_{TAT}) is calculated just by replacing the DT probability [$P_{\mathrm{DT}}(E)$] in Eq. (3.1) with $P_{\mathrm{TAT}}(E)$, that is,

$$J_{\mathrm{TAT}} = \frac{A^*T}{k_{\mathrm{B}}}\int P_{\mathrm{TAT}}(E)\ln\left[\frac{\exp\{-(E-E_{\mathrm{Fm}})/k_{\mathrm{B}}T\}+1}{\exp\{-(E-E_{\mathrm{Fs}})/k_{\mathrm{B}}T\}+1}\right]\mathrm{d}E, \tag{4.2}$$

where A^* is the effective Richardson constant ($151\,\mathrm{A/cm^2K^2}$ as calculated in Chap. 2), T is the absolute temperature, k_{B} is the Boltzmann constant, E is the electron energy along the tunneling direction, and E_{Fm} and E_{Fs} are the Fermi levels in the metal and semiconductor, respectively.

In MOS structures fabricated with defect-containing oxides (e.g., nitrided oxides), leakage current due to TAT is often observed under a relatively low oxide field before Fowler-Nordheim (FN) tunneling arises [15–17]. Although analytical formulas for TAT to describe the leakage current in the oxide have been developed [18, 19], these models treat a constant oxide field. Thus, it is required to perform the numerical calculation based on Eq. (4.1) when dealing with metal/heavily-doped SiC structures, as is the case for DT.

4.5.2 Calculation

As seen in Eq. (4.1), the TAT calculation has many parameters, such as N_{T}, σ_{T}, and E_{T} as well as ϕ_{B0}. Although these trap parameters in ion-implanted SiC have been carefully studied based on deep-level transient spectroscopy (DLTS) measurement [10, 11], the maximum doping density investigated was limited up to $1\times10^{18}\,\mathrm{cm^{-3}}$ (corresponding to the dose of $8\times10^{13}\,\mathrm{cm^{-2}}$). Therefore, the defect properties in an ion-implanted region formed with a

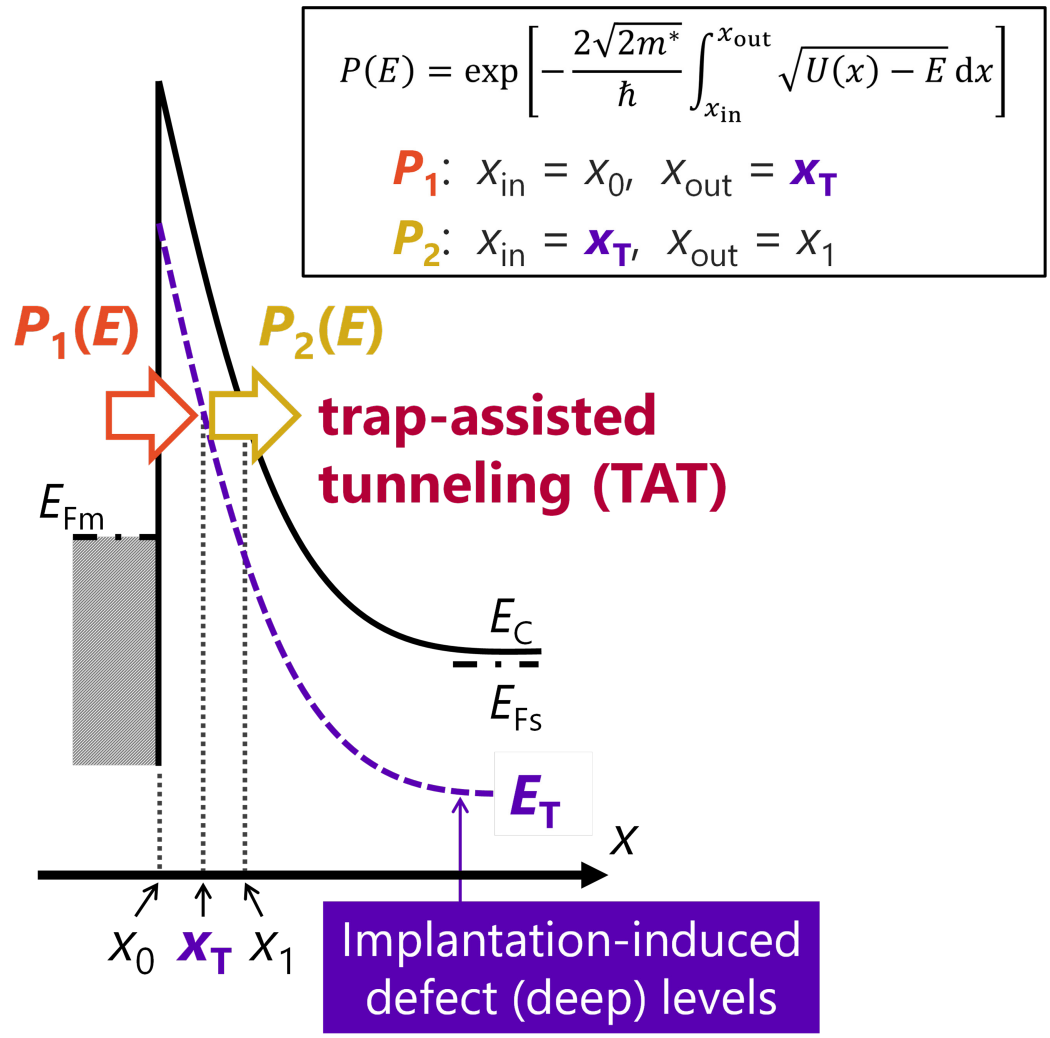

Figure 4.7: Schematic band diagram of trap-assisted tunneling (TAT) through a Schottky barrier.

higher dose are still poorly understood, making it difficult to perform quantitative analysis of the experimental I–V characteristics of the heavily P^+-implanted SiC SBDs through the numerical calculation with reasonable parameters.

In this study, the author focuses mainly on the E_T dependence of the TAT current and tries to speculate the trap levels that dominantly contribute to the TAT process at metal/P^+-implanted SiC interfaces. In the calculation, N_d was set to be $5 \times 10^{18}\,cm^{-3}$, and ϕ_{B0} values of 0.7, 1.0, and 1.6 eV were treated. Note that the energy potential was defined as the sum of the parabolic and image force potentials, as described in Chap. 3. Regarding N_T (unit: cm^{-2}), implantation-induced traps were assumed to be uniformly distributed in the P^+-implanted region with a volume density of a hundredth N_d (i.e., $5 \times 10^{16}\,cm^{-3}$). Thus, the area density of the trap is calculated as $3 \times 10^{12}\,cm^{-2}$, multiplying the volume density by the implantation depth (600 nm). Since the capture cross section for the tunneling carriers is unknown, σ_T was assumed to be $1 \times 10^{-13}\,cm^2$. With these parameters, the TAT calculation was performed by varying E_T.

4.5.3 Speculation of Dominant Trap Levels

Figure 4.8 shows an example of the calculated (a) band diagram, (b) tunneling probability, and (c) tunneling current as a function of the electron energy under a forward bias of 0.1 V, comparing the DT probability and DT current with those in the case of TAT through a trap with the energy level of $E_C - E_T = 0.3\,eV$, where E_C is the conduction band edge in SiC. As depicted by the red and blue solid lines, $P_{TAT}(E)$ is several orders of magnitude higher than $P_{DT}(E)$ at a given energy. The enhanced tunneling probability in a lower energy range allows more electrons to tunnel through the barrier, shifting E_{peak} (energy where the electron tunneling most frequently occurs) to the lower energy side and leading to a larger tunneling current, as seen in Fig. 4.8(c). Investigating the two probability components of $P_1(E)$ and $P_2(E)$, it is found that the smaller one (i.e., the tunneling probability for a longer tunneling path) determines the TAT probability, as displayed by the orange and yellow dashed lines in Fig. 4.8(b). Since the barrier thickness for a longer tunneling path becomes similar to that for the DT process in the case of too deep or shallow trap levels, moderately deep levels are expected to contribute most effectively to the enhanced tunneling current. In this sense, how an E_T change influences the TAT current is examined to speculate the dominant trap level.

Figure 4.9 shows (a) forward and (b) reverse I–V characteristics in n-type SiC Schottky structures ($\phi_{B0} = 1.0\,eV$) calculated based on the TAT model assuming various E_T. The calculated DT current is also displayed by the gray dashed lines. While the TAT current is larger than the DT current in most cases, the obtained I–V curves are very different strongly depending on the E_T value. In the forward characteristics, the tunneling current is enhanced in a wide voltage range with the contribution of relatively shallow levels ($E_C - E_T = 0.2$–$0.3\,eV$). In contrast, under a small forward bias ($V \lesssim +0.1\,V$), the energy

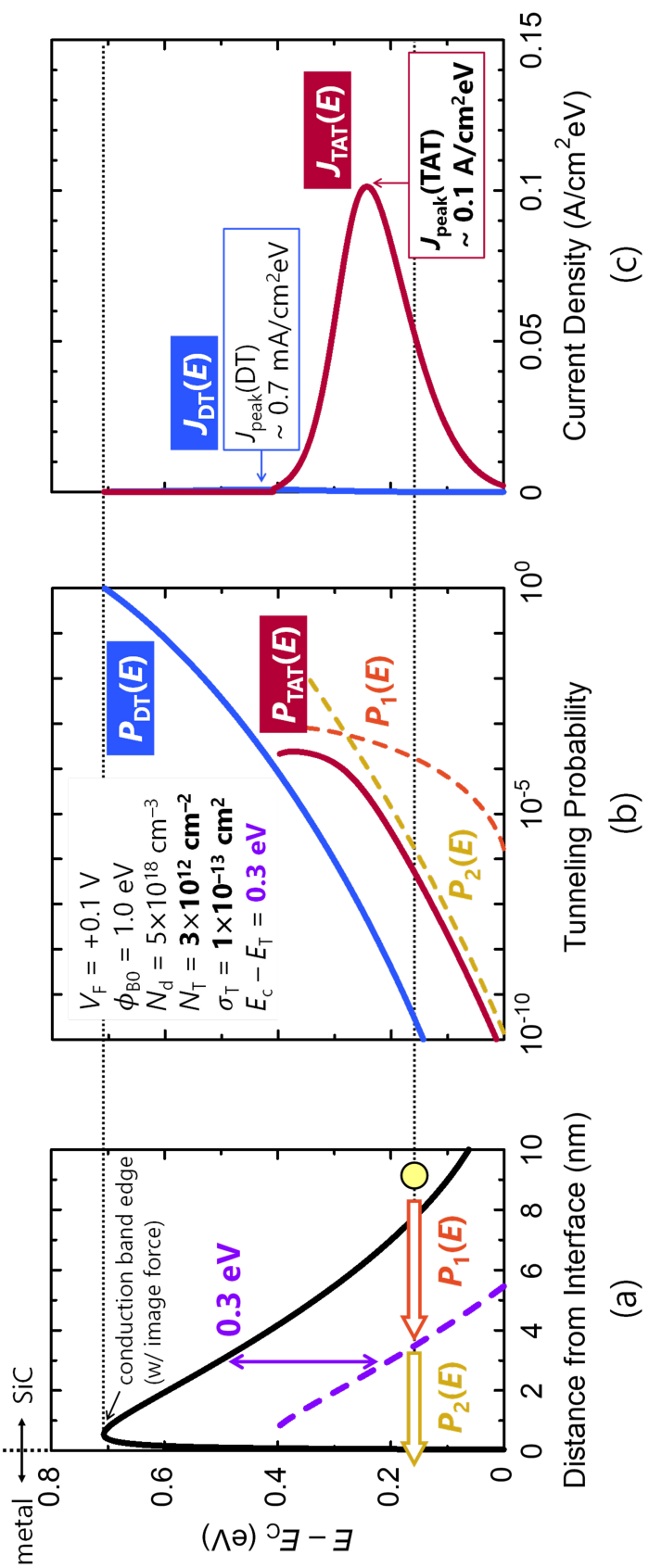

Figure 4.8: (a) Band diagram, (b) tunneling probability, and (c) tunneling current as a function of the electron energy numerically calculated based on the DT and TAT models. The parameters used in the calculation are indicated in the figure.

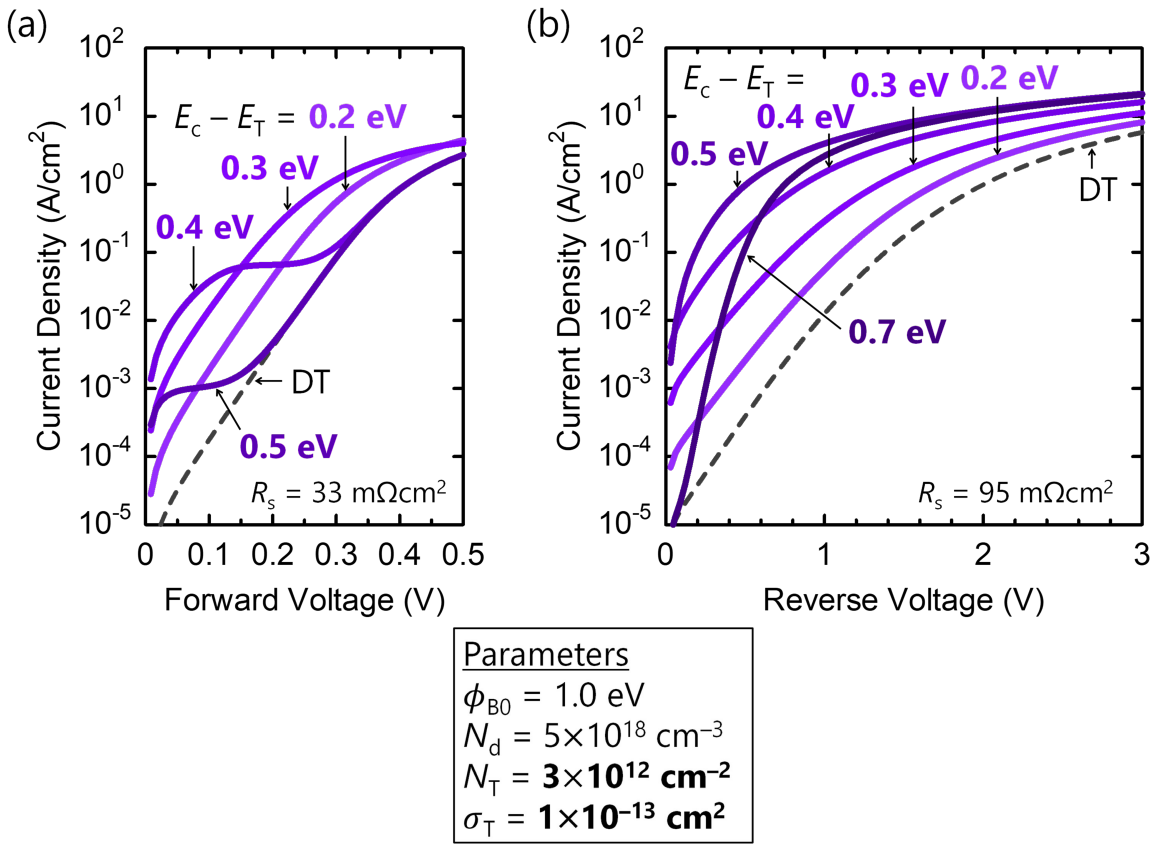

Figure 4.9: (a) Forward and (b) reverse I–V characteristics in n-type SiC Schottky structures calculated based on the TAT model assuming various E_T.

level of $E_C - E_T \simeq 0.4\,\mathrm{eV}$ most largely increases the current density. With a reverse bias applied, a larger TAT current is obtained with the contribution of deeper trap levels when $E_C - E_T$ is below 0.5 eV. On the other hand, the TAT current becomes smaller (especially under a small bias condition) and almost equal to the DT current with deeper traps ($E_C - E_T > 0.5\,\mathrm{eV}$). The applied-voltage-dependent changes in which trap level mainly contributes to the enhanced tunneling current are discussed based on the E_T dependence of $P_{TAT}(E)$ in each bias condition.

Figure 4.10(a) again plots the forward I–V characteristics in n-type SiC Schottky structures calculated with the TAT model. First, under a small forward bias of $V = +0.05\,\mathrm{V}$, the tunneling path is divided into almost halves in a wide energy range when passing through the trap level with $E_C - E_T \simeq 0.4\,\mathrm{eV}$, resulting in a high tunneling probability and large tunneling current, as plotted in Fig. 4.10(b). As the applied forward voltage increases, on the other hand, tunneling electrons can encounter traps located deep below E_C only in a narrow energy range, and positions where the tunneling path is divided shift toward the interface side (i.e., a balance between P_1 and P_2 is broken.). Therefore, the enhancement of the tunneling probability and current by deep trap levels ($E_C - E_T > 0.4\,\mathrm{eV}$) is limited in a small voltage range, and relatively shallower trap levels ($E_C - E_T = 0.2$–$0.3\,\mathrm{eV}$) become dominant instead, as shown in Fig. 4.10(c). As a result, it is shown that, in the case of a forward bias condition, different trap levels play a significant role in the enhanced tunneling current, depending on the applied voltage. The dominant trap levels under a small forward bias are speculated to be located at the energy of $E_C - E_T \simeq 0.4\,\mathrm{eV}$, which is about half of the Schottky barrier height ($\phi_{B0} = 1.0\,\mathrm{eV}$). Then, relatively shallow traps with the energy level of $E_C - E_T = 0.2$–$0.3\,\mathrm{eV}$ become predominant as the applied forward voltage increases.

Reverse I–V characteristics in n-type SiC Schottky structures calculated with the TAT model are again indicated in Fig. 4.11(a) to discuss how different the situation is under a reverse bias condition. Since tunneling mainly occurs at the energy above the Fermi level, the TAT current is greatly enhanced when the tunneling path above E_{Fm} is divided into halves. In this sense, too-deep traps with $E_C - E_T \gtrsim 0.6\,\mathrm{eV}$ do not make the tunneling current larger effectively, especially at a small reverse bias, as shown in Fig. 4.11(b). Under an increased reverse bias, on the other hand, the TAT current through deep traps (typically $E_C - E_T = 0.6$–$0.7\,\mathrm{eV}$) is found to be larger than that with $E_C - E_T < 0.4\,\mathrm{eV}$ because the TAT probability in the energy range below E_{Fm} is greatly enhanced by a nearly identical distance of the two divided paths, as indicated in Fig. 4.11(c). Despite that, as is the case of the forward bias, these very deep traps can affect the tunneling process in a limited energy range. Therefore, the calculated TAT current with $E_C - E_T > 0.7\,\mathrm{eV}$ is confirmed to become smaller when further deep traps are assumed, even at a large reverse bias. As a result, almost in the entire voltage range calculated, a trap level with $E_C - E_T \simeq 0.5\,\mathrm{eV}$, which is about half of the Schottky barrier height ($\phi_{B0} = 1.0\,\mathrm{eV}$), is speculated to be the dominant trap level also under a reverse bias condition.

The trap levels that may significantly enhance the TAT current in Schottky structures on

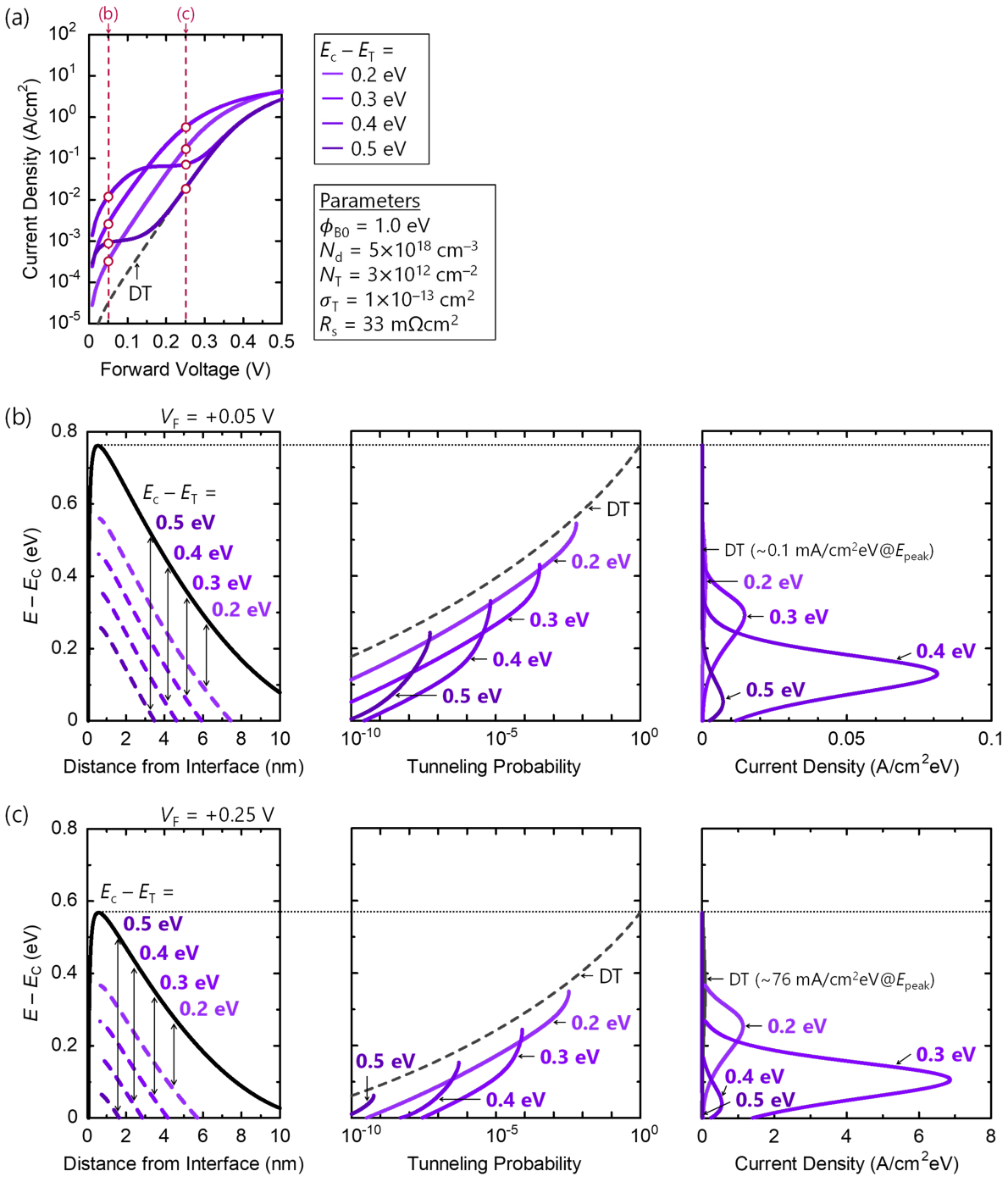

Figure 4.10: (a) Forward I–V characteristics in n-type SiC Schottky structures calculated based on the TAT model, in which the TAT current at a small or large bias is compared for various E_T. Band diagram, tunneling probability, and tunneling current as a function of the electron energy at (b) a small forward bias ($V = +0.05\,\mathrm{V}$) and (c) a large forward bias ($V = +0.25\,\mathrm{V}$).

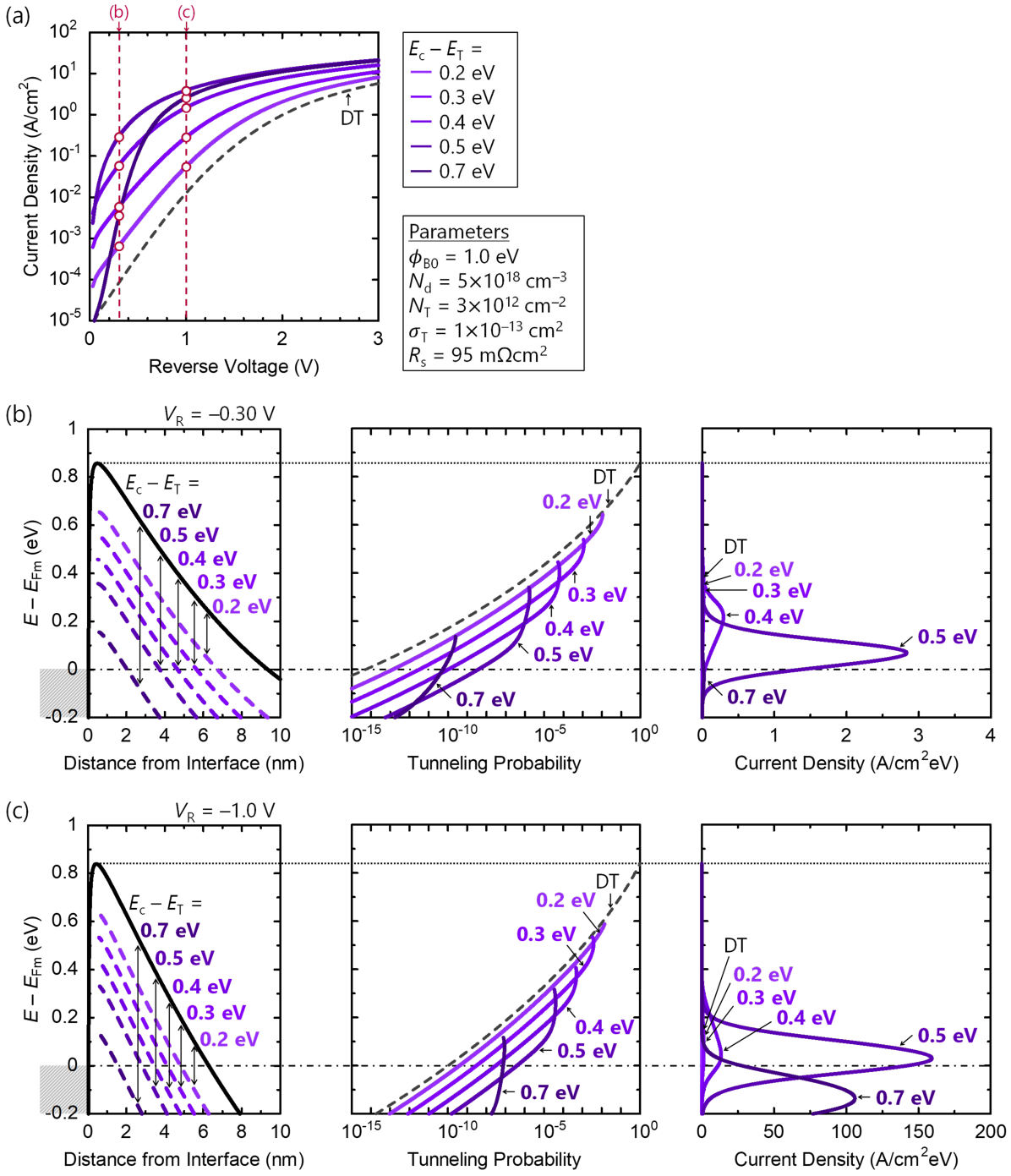

Figure 4.11: (a) Reverse I–V characteristics in n-type SiC Schottky structures calculated based on the TAT model, in which the TAT current at a small or large bias is compared for various E_T. Band diagram, tunneling probability, and tunneling current as a function of the electron energy at (b) a small reverse bias ($V = -0.30\,\mathrm{V}$) and (c) a large reverse bias ($V = -1.0\,\mathrm{V}$).

heavily P^+-implanted SiC ($N_d = 5 \times 10^{18}\,cm^{-3}$) speculated from the numerical calculation are summarized in Table 4.1. Note that identical trap parameters (N_T and σ_T) were assumed in the speculation, which does not correctly deal with the actual situation.

4.6 Discussion

First, the dominant trap levels speculated above are compared with the traps experimentally detected in P^+-implanted SiC through DLTS measurement [11], which are summarized in Fig. 4.12. It is considered that IN2 (ID_8) and IN3 ($Z_{1/2}$) centers are responsible for enhancing the TAT current among the reported traps. Based on the trap properties listed in Table 4.2, on the other hand, the TAT calculation performed in this study assumed very large values of N_T and σ_T, even if the capture cross sections for tunneling carriers (parameters in the calculation) and thermal process (reported ones) need not be identical. Even using such large values, however, the calculated TAT current is still smaller by several orders of magnitude than the experimental data. As mentioned above, the maximum doping density of P^+-implanted SiC investigated so far is limited up to $1 \times 10^{18}\,cm^{-3}$, and thus, more kinds and amounts of traps are expected inside a higher-dose implanted region. Therefore, it is indispensable to characterize and clarify the defect properties in such a high-dose implanted region ($> 10^{18}\,cm^{-3}$) through careful experiments, including electrical measurement and structural analyses. Besides, it seems that several aspects have to be considered in the TAT calculation additionally: for example, how to convert the trap density from the volume density to area density, the energy conservation before and after trapping, thermionic emission of carriers from traps, and so forth. It is an essential future research subject to perform quantitative analysis and full modeling of the TAT current in heavily P^+-implanted SiC Schottky structures with various N_d and ϕ_{B0} by addressing these matters.

From a practical point of view, the enhanced tunneling current should be advantageous in obtaining low-resistance ohmic contacts. Considering the significant contribution of the traps located at the energy of $E_C - E_T \simeq \phi_{B0}/2$ in a small bias range, a very low contact resistivity (ρ_c) is expected for contacts on heavily P^+-implanted SiC, as if the Schottky barrier became about half of ϕ_{B0}. Thus, the next interest is in identifying how low ρ_c can be achieved without performing high-temperature sintering and whether a ρ_c value is predicted considering the contribution of TAT as well as DT, which will be extensively discussed in the following chapter.

4.7 Summary

In this chapter, fundamental properties in metal/heavily P^+-implanted SiC Schottky structures, including the net donor density (N_d), barrier height (ϕ_{B0}), and carrier transport

Table 4.1: Trap levels that may mainly contribute to the TAT current through metal/heavily P^+-implanted SiC interfaces ($N_d = 5 \times 10^{18}\,cm^{-3}$) with various barrier heights, which are speculated from the numerical calculation assuming that all the traps have the same trap parameters (N_T and σ_T).

Barrier height ϕ_{B0} (eV)	Bias condition	Dominant trap level $E_C - E_T$ (eV)
0.7	forward, small ($\|V\| \lesssim 0.05\,V$)	0.2–0.3
	forward, large ($\|V\| \gtrsim 0.05\,V$)	0.2
	reverse	0.3
1.0	forward, small ($\|V\| \lesssim 0.1\,V$)	0.4
	forward, large ($\|V\| \gtrsim 0.1\,V$)	0.2–0.3
	reverse, small ($\|V\| \lesssim 0.4\,V$)	0.4–0.5
	reverse, large ($\|V\| \gtrsim 0.4\,V$)	0.5–0.7
1.6	forward, small ($\|V\| \lesssim 0.2\,V$)	0.6–0.7
	forward, large ($\|V\| \gtrsim 0.2\,V$)	0.3–0.5
	reverse, small ($\|V\| \lesssim 0.5\,V$)	0.7–0.8
	reverse, large ($\|V\| \gtrsim 0.5\,V$)	0.8–1.0

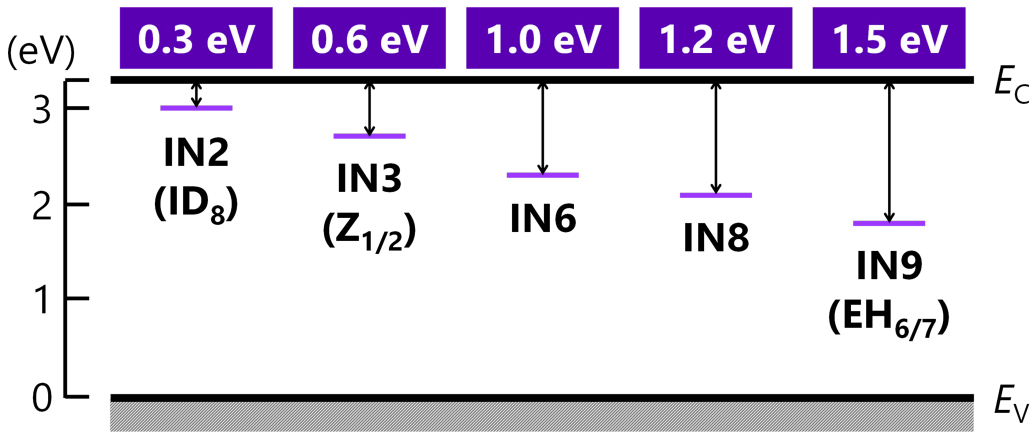

Figure 4.12: Major traps detected in P^+-implanted SiC and their energy levels [11].

Table 4.2: Major traps in P^+-implanted SiC and their energy levels, capture cross sections, and densities reported based on DLTS measurement [11].

Label	Dose	Impurity density	Energy level	Capture cross section	Trap density (after oxidation; 1150°C, 2 h for 2 times)
	(cm^{-2})	(cm^{-3})	$E_C - E_T$ (eV)	σ (cm^2)	N_T (cm^{-3})
IN2 (ID_8)	8.0×10^{13}	1×10^{18}	0.30	10^{-18}	$< 2 \times 10^{15}$
IN3 ($Z_{1/2}$)	5.6×10^{10}	7×10^{14}	0.63	10^{-14}	2×10^{14}
IN6	8.0×10^{13}	1×10^{18}	1.0	10^{-15}	$< 7 \times 10^{15}$
IN8	8.0×10^{13}	1×10^{18}	1.2	10^{-15}	$< 4 \times 10^{15}$
IN9 ($EH_{6/7}$)	5.6×10^{10}	7×10^{14}	1.5	10^{-14}	2×10^{14}

characteristics, were investigated in detail. C–V measurement on vertical SBDs fabricated with P^+-implanted SiC with various P atom densities allowed to accurately characterize N_d and ϕ_{B0}, revealing that above 90% of the implanted P atoms are activated as donors even at a high N_d of $3 \times 10^{19}\,cm^{-3}$, and the barrier heights at Schottky contacts on implanted and epitaxial layers are nearly identical. The tunneling current at a metal/P^+-implanted SiC interface was larger by several orders of magnitude than that at contacts on epitaxial layers with almost the same N_d, which is likely ascribed to the contribution of trap-assisted tunneling (TAT) through implantation-induced deep levels. By performing the numerical calculation of the TAT current, it was speculated which trap level dominantly contributes to the enhanced tunneling current under various applied bias conditions. As a result, it was indicated that trap levels located below the energy of about half of the barrier height below the conduction band edge seem to be dominant near the zero bias condition, which may significantly impact the ohmic contact formation.

The similarities and differences in the fundamental properties between contacts formed on ion-implanted and epitaxial SiC are vital for discussing the ohmic contact formation mechanism and designing low-resistance ohmic contacts.

References

[1] T. Kimoto and J. A. Cooper, *Fundamentals of Silicon Carbide Technology: Growth, Characterization, Devices and Applications* (John Wiley & Sons, 2014).

[2] M. Laube, F. Schmid, G. Pensl, G. Wagner, M. Linnarsson, and M. Maier, *J. Appl. Phys.* **92**, 549 (2002).

[3] Y. Negoro, K. Katsumoto, T. Kimoto, and H. Matsunami, *J. Appl. Phys.* **96**, 224 (2004).

[4] T. Kobayashi, J. Suda, and T. Kimoto, *Appl. Phys. Express* **7**, 121301 (2014).

[5] M. A. Capano, R. Santhakumar, R. Venugopal, M. R. Melloch, and J. A. Cooper, *J. Electron. Mater.* **29**, 210 (2000).

[6] J. Senzaki, K. Fukuda, and K. Arai, *J. Appl. Phys.* **94**, 2942 (2003).

[7] M. Spera, G. Greco, A. Severino, M. Vivona, P. Fiorenza, F. Giannazzo, and F. Roccaforte, *Appl. Phys. Lett.* **117**, 013502 (2020).

[8] T. Dalibor, G. Pensl, H. Matsunami, T. Kimoto, W. J. Choyke, A. Schöner, and N. Nordell, *Phys. Stat. Sol. A* **162**, 199 (1997).

[9] M. L. David, G. Alfieri, E. M. Monakhov, A. Hallén, C. Blanchard, B. G. Svensson, and J. F. Barbot, *J. Appl. Phys.* **95**, 4728 (2004).

[10] K. Kawahara, G. Alfieri, and T. Kimoto, *J. Appl. Phys.* **106**, 013719 (2009).

[11] K. Kawahara, J. Suda, G. Pensl, and T. Kimoto, *J. Appl. Phys.* **108**, 033706 (2010).

[12] G. H. Parker and C. A. Mead, *Appl. Phys. Lett.* **14**, 21 (1969).

[13] J. C. Penley, *Phys. Rev.* **128**, 596 (1962).

[14] J. W. Gadzuk, *J. Appl. Phys.* **41**, 286 (1970).

[15] F. W. Schmidlin, *J. Appl. Phys.* **37**, 2823 (1966).

[16] E. Suzuki, D. K. Schroder, and Y. Hayashi, *J. Appl. Phys.* **60**, 3616 (1986).

[17] X. R. Cheng, Y. C. Cheng, and B. Y. Liu, *J. Appl. Phys.* **63**, 797 (1988).

[18] S. Fleischer, P. T. Lai, and Y. C. Cheng, *J. Appl. Phys.* **72**, 5711 (1992).

[19] M. P. Houng, Y. H. Wang, and W. J. Chang, *J. Appl. Phys.* **86**, 1488 (1999).

Chapter 5

Tunneling Phenomena-Based Modeling of Contact Resistivity for Non-Alloyed Ohmic Contacts on *n*-Type SiC

5.1 Introduction

As introduced in Chap. 1, the currently available high-temperature process for the ohmic contact formation has several negative impacts on device performance and reliability and does not offer a very low contact resistivity ($\rho_c < 10^{-6}\,\Omega\text{cm}^2$) [1–4]. Therefore, a novel fabrication process for low-resistance SiC ohmic contacts with a low thermal budget is strongly desired. So far, several trials have been made to achieve a low ρ_c with a low-temperature process, basically based on high-dose ion implantation or barrier height lowering with a low-work-function electrode metal [5–7]. However, no guidelines exist over how high doping density and low barrier height are required to achieve a sufficiently low ρ_c, and even the difference between epitaxial growth and ion implantation regarding the formation of contact regions has not been discussed.

In Chaps. 2–4, barrier properties and high-field tunneling phenomena, including direct tunneling (DT) and trap-assisted tunneling (TAT), at metal/heavily-doped SiC Schottky (non-alloyed) interfaces have been clarified. The deep understanding of the fundamental physics of the non-alloyed contacts gained in the former chapters helps to construct a model predicting ρ_c at non-alloyed SiC ohmic contacts and to establish design guidelines for ρ_c reduction.

In this chapter, non-alloyed contacts are formed on heavily P^+-implanted SiC, and their ρ_c values are systematically investigated. In the experiment, ρ_c is characterized by varying the net donor density (N_d) in the implanted layers and employing various electrode metals (i.e., various barrier heights). Besides, the experimentally obtained ρ_c is analyzed based on

the numerical calculation of the tunneling current. Through the experiment and calculation, a model to describe ρ_c at non-alloyed SiC ohmic contacts as a function of N_d and zero-field barrier height (ϕ_{B0}) is proposed.

5.2 Experimental Characterization

5.2.1 Circular Transmission Line Model Structures

Figure 5.1 illustrates a schematic image of the circular transmission line model (CTLM) structure [8] fabricated on P^+-implanted SiC. This structure consists of the inner and outer electrodes and is designed to have various gap distances between them. When measuring the current through the inner and outer electrodes, the total resistance is composed of the contact resistance at the two electrodes and the resistance of the semiconductor layer between them. Since the semiconductor layer resistance is directly connected to the electrode spacing, the contact resistance component is extracted by performing current–voltage (I–V) measurement for various electrode spacings. The CTLM structure has several advantages over the conventional rectangle-shaped TLM pattern; the current flow is limited only between the electrodes, allowing the accurate extraction of ρ_c with a mesa-free structure [9].

5.2.2 Sample Preparation

In the fabrication, p-type SiC epitaxial layers (net acceptor density: $2 \times 10^{15}\,\mathrm{cm}^{-3}$) on n-type 4H-SiC(0001) substrates were prepared for the electrical isolation between the P^+-implanted n-type region and the n-type substrate. P ions were implanted into the epitaxial layer, and about 230-nm deep box-shaped profiles were created with various P atom densities ($N_P = 4.0\times10^{18}$, 9.0×10^{18}, 2.7×10^{19}, 7.0×10^{19}, and $2.3\times10^{20}\,\mathrm{cm}^{-3}$), as shown in Fig. 5.2. The implantation for $N_P = 2.7 \times 10^{19}$, 7.0×10^{19}, and $2.3 \times 10^{20}\,\mathrm{cm}^{-3}$ was conducted at 500°C. Activation annealing was performed at 1750°C in Ar ambient, and the N_P profile near the surface was flattened by sacrificial oxidation at 1300°C and subsequent oxide removal with hydrogen fluoride dipping. Ti or Mg was deposited by resistive heating evaporation as a contact metal on the P^+-implanted SiC. The ϕ_{B0} values for the Ti and Mg electrodes correspond to about 1.0 eV and 0.7 eV, respectively, which were characterized by using a vertical SBD structure fabricated on epitaxial layers. The thicknesses of the deposited Ti and Mg films are about 40 nm and 300 nm, respectively. Then, Al(280 nm)/Ni(80 nm) and Ni(120 nm) electrode stacks are subsequently formed on the Ti and Mg films, respectively, to ensure a negligibly small parasitic resistance of the electrode metal in the direction parallel to the interface. It should be noted that no post-metallization sintering was performed on the electrodes. The radius of the inner electrodes (L) was 96 μm, and the electrode spacing (d) between the inner and outer electrodes was varied from 13 to 54 μm, confirmed based on optical microscope images. I–V characteristics of the CTLM structures were measured

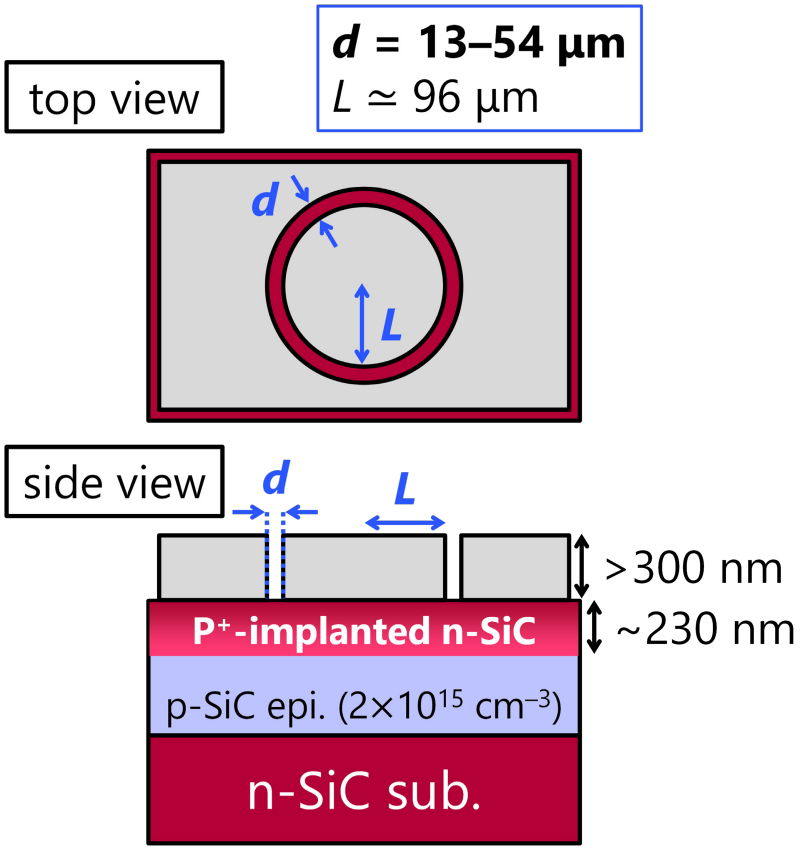

Figure 5.1: Schematic image of a circular transmission line model (CTLM) structure fabricated on P^+-implanted n-type SiC.

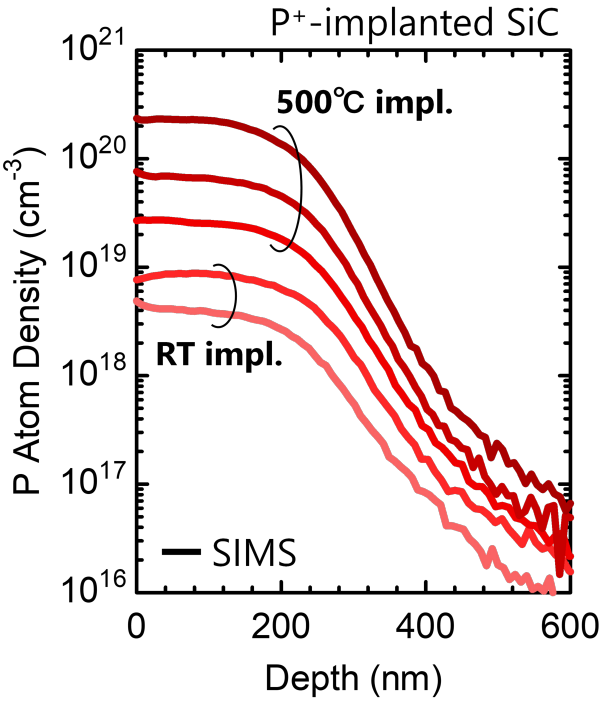

Figure 5.2: Depth profile of the P atom density implanted into p-type SiC epilayers obtained by SIMS measurement.

with a four-probe configuration, which can eliminate the parasitic resistance components in the measurement system. The ρ_c value was determined by extracting the resistance (R) from the measured I–V curves with various d.

5.2.3 Current–Voltage and Resistance–Electrode Spacing Characteristics

Figure 5.3 plots the experimental I–V curves (linear scale) at the Ti and Mg contacts. An ohmic-like linear I–V relationship is obtained without performing high-temperature sintering for every electrode. Concerning the N_P dependence, a larger current is observed for the sample with a higher N_P (i.e., higher N_d). When comparing the Ti and Mg contacts, the Mg electrodes show a larger current than Ti, especially when N_P is lower than $3 \times 10^{19}\,\mathrm{cm}^{-3}$, reflecting the lower ϕ_{B0} of the Mg contacts. On the other hand, when N_P exceeds $7 \times 10^{19}\,\mathrm{cm}^{-3}$, the I–V characteristics become less dependent on ϕ_{B0} and almost similar. This tendency can be understood by considering the barrier thickness for tunneling carriers at metal/heavily-doped SiC interfaces with a different ϕ_{B0}. Figure 5.4 gives the N_d dependence of the depletion layer width (w) at zero bias roughly calculated by assuming that the built-in potential (V_d) equals ϕ_{B0}. As seen in Fig. 5.4, w becomes less dependent on ϕ_{B0} with increasing N_d and is obtained to be about 4 nm or 3 nm for $\phi_{B0} = 1.0\,\mathrm{eV}$ or $0.7\,\mathrm{eV}$, respectively, at $N_d = 7 \times 10^{19}\,\mathrm{cm}^{-3}$. Thus, the tunneling probability becomes closer with increasing N_d in any case where DT or TAT is dominant, leading to the ϕ_{B0}-independent I–V characteristics obtained for a high N_P.

Then, the R values were extracted from the I–V curves of the CTLM patterns with various d. The symbols in Fig. 5.5 represent the experimental R–d plots for the (a) Ti and (b) Mg CTLM structures with various N_P. A fitting analysis of the experimental R–d relationship was performed to determine ρ_c. An expression to relate R to d is given by [9],

$$R(d) = \frac{R_{sh}}{2\pi}\left[\frac{L_T}{L}\frac{I_0(L/L_T)}{I_1(L/L_T)} + \frac{L_T}{L+d}\frac{K_0(L/L_T)}{K_1(L/L_T)} + \ln\left(1+\frac{d}{L}\right)\right], \tag{5.1}$$

where R_{sh} is the sheet resistance in the semiconductor layer beneath the contact, L_T is the transfer length, I and K are the modified Bessel functions of the first and second kinds whose subscript (0 or 1) expresses their order, respectively. Taking R_{sh} and L_T in Eq. (5.1) as parameters, a numerical fitting to the experimental data was conducted, as depicted by the dashed lines in Fig. 5.5.

Figure 5.6 shows (a) R_{sh} as a function of the total implant dose and (b) L_T versus N_P plots. The R_{sh} values were consistently obtained for both the Ti and Mg CTLM structures. Besides, a lower R_{sh} is obtained when the P^+ implantation is performed with a higher dose, which is consistent with the reported values in heavily P^+-implanted SiC characterized by Hall-effect measurement on Van der Pauw structures [10], as indicated by the gray circles in Fig. 5.6(a). The L_T value decreases with increasing N_P and is obtained to be

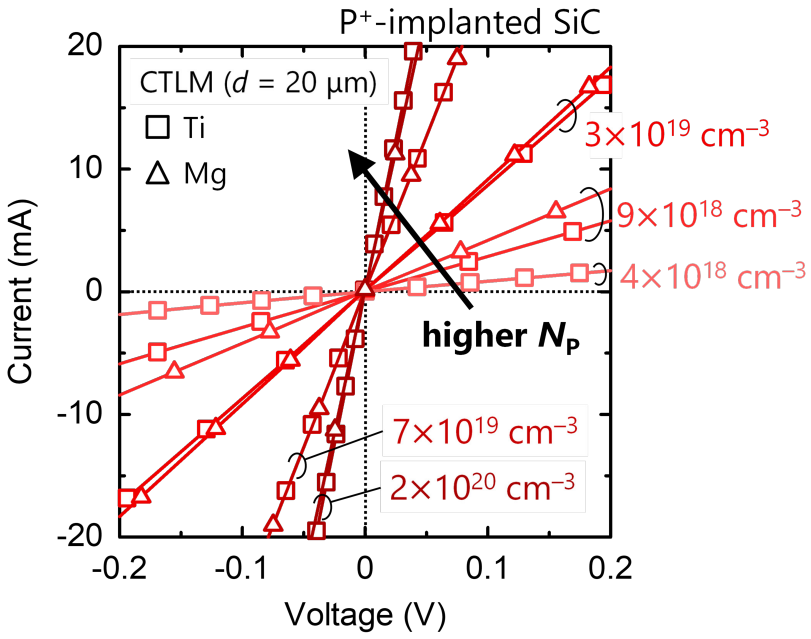

Figure 5.3: I–V characteristics (linear plots) of the Ti and Mg CTLM structures with various N_{P} (electrode spacing, $d = 20\,\mu$m).

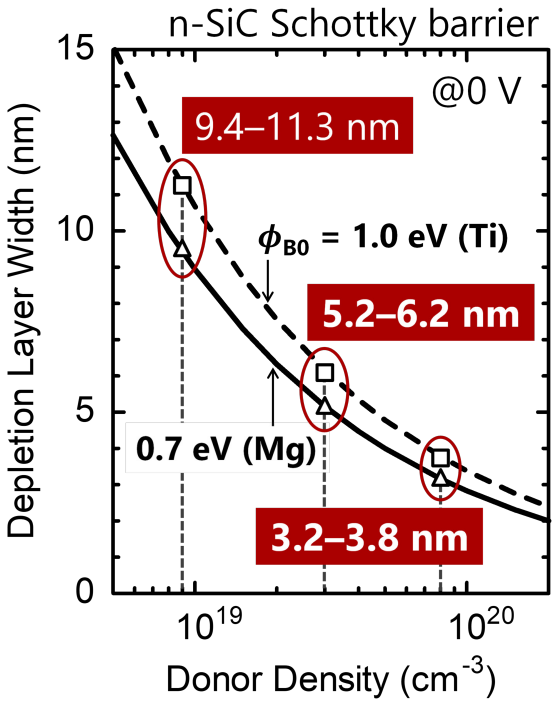

Figure 5.4: Depletion layer width at zero bias calculated for n-type SiC Schottky structures as a function of the donor density of SiC.

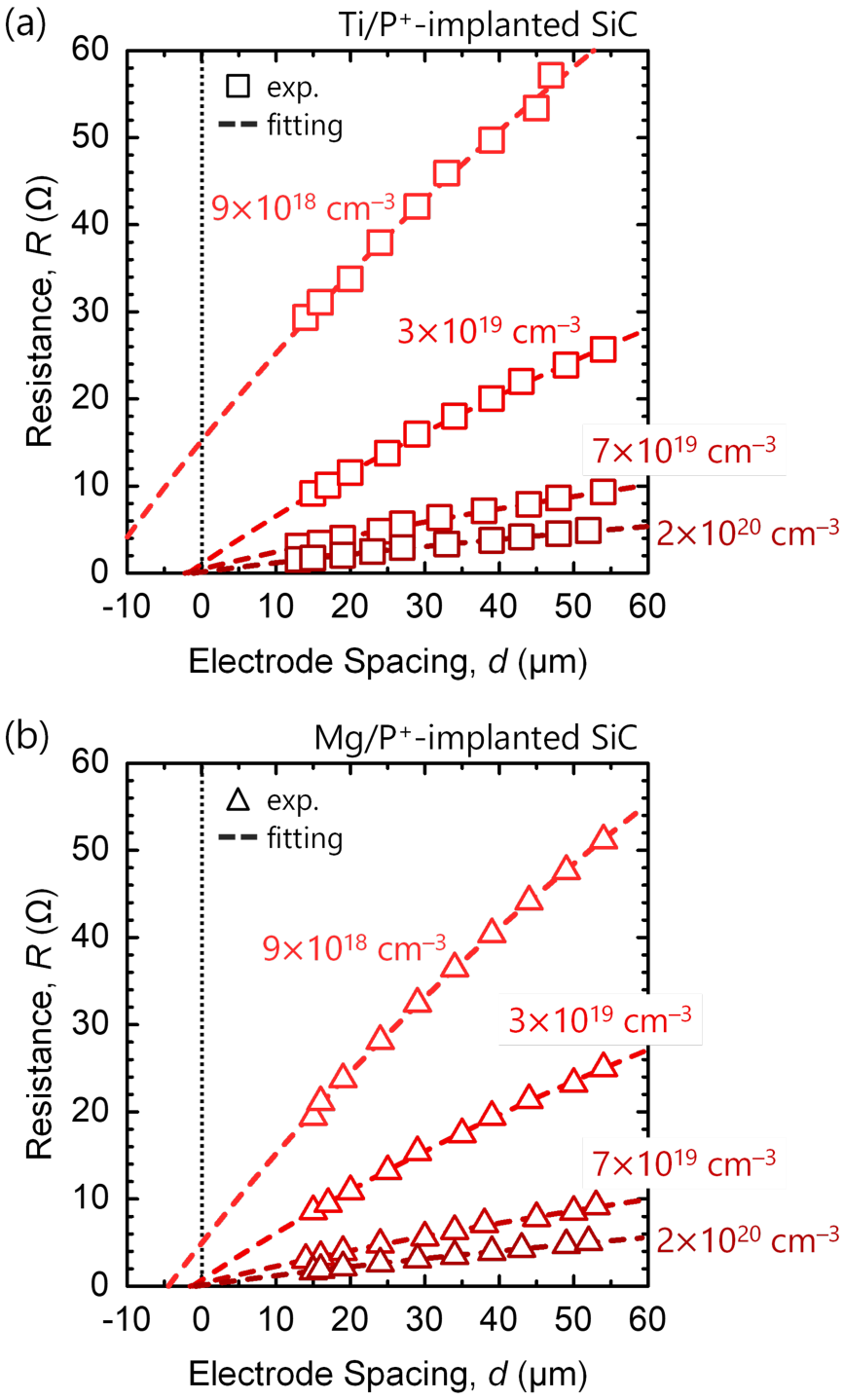

Figure 5.5: Resistance (R) versus electrode spacing (d) of the (a) Ti and (b) Mg CTLM structures. The symbols are experimental data, and the dashed lines depict fitting curves based on Eq. (5.1).

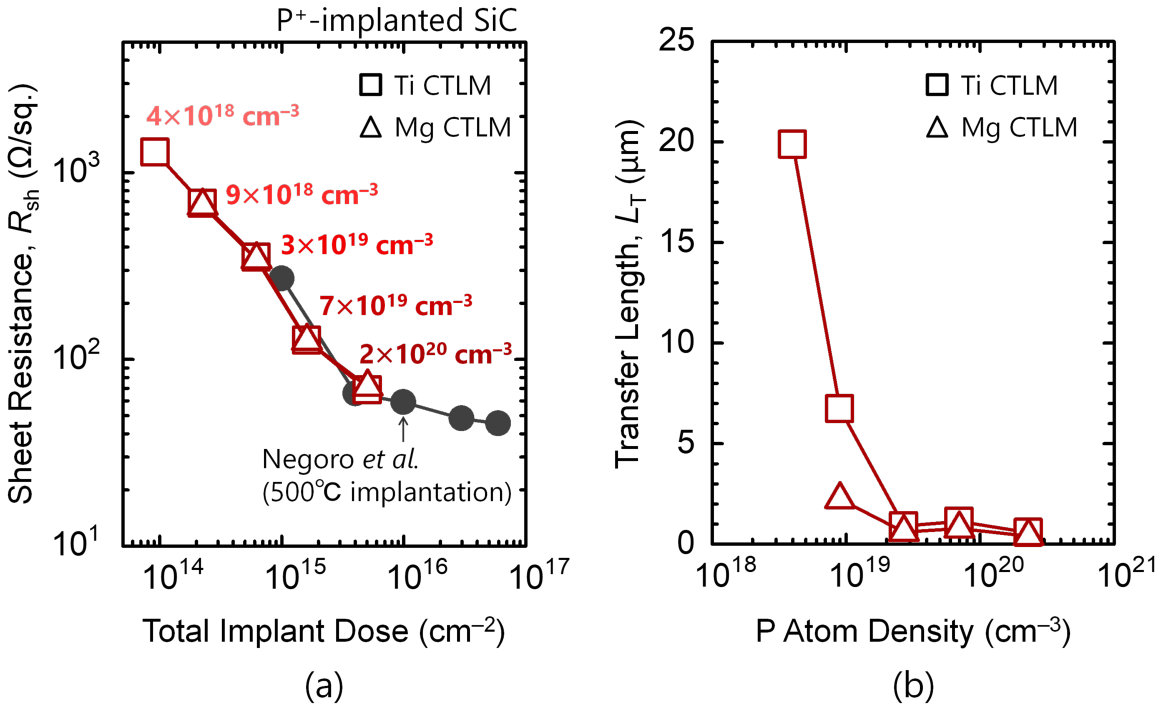

Figure 5.6: (a) Sheet resistance in the P^+-implanted regions as a function of the total implant dose. Reported data based on Hall-effect measurement (Negoro *et al.* [10]) are also shown by circles. (b) Transfer length plotted against the implanted P atom density.

0.6–20 μm and 0.4–2.2 μm for the Ti and Mg CTLM structures, respectively. From these obtained parameters ($R_{\rm sh}$ and $L_{\rm T}$), the contact resistivity is determined with the formula of $\rho_{\rm c} = R_{\rm sh}L_{\rm T}^2$ [9], which will be presented in Sect. 5.4.

5.3 Calculation of Contact Resistivity Based on Direct Tunneling

For modeling the experimental $\rho_{\rm c}$ based on understanding the tunneling phenomena, $\rho_{\rm c}$ was also determined by the DT current calculation. Although the $\rho_{\rm c}$ analysis has been conventionally performed with the analytical formulas of the thermionic field emission (TFE) and field emission (FE) models [11, 12], the numerical calculation of the DT current with Eq. (3.1) was performed to consider the TFE-FE transition and accurately analyze $\rho_{\rm c}$ in an entire range of $N_{\rm d}$, as mentioned in Chap. 3. The calculation procedure for the DT-based $\rho_{\rm c}$ is as follows:

1. At the given $N_{\rm d}$ and $\phi_{\rm B0}$, DT current through metal/n-type SiC is calculated based on Eq. (3.1) in the voltage range from -0.05 to 0.05 V.

2. $\rho_{\rm c}$ is extracted by taking the slope of the calculated $J_{\rm DT}$–V characteristics near 0 V ($-0.01\,{\rm V} \le V \le +0.01\,{\rm V}$).

3. The above calculation is repeatedly performed with various $N_{\rm d}$ and $\phi_{\rm B0}$, and the DT-based $\rho_{\rm c}$ is obtained as a function of these parameters.

Figure 5.7(a) shows the calculated $J_{\rm DT}$–V curves in metal/n-type SiC Schottky structures with various $N_{\rm d}$ assuming $\phi_{\rm B0} = 1.0\,{\rm eV}$. A larger current and steeper slope are obtained with increasing $N_{\rm d}$, indicating that $\rho_{\rm c}$ decreases at a higher $N_{\rm d}$, as calculated for various $\phi_{\rm B0}$ cases (0.4–1.1 eV) shown in Fig. 5.7(b).

5.4 Contact Resistivity Modeling

5.4.1 Contact Resistivity vs. Donor Density and Barrier Height

The $N_{\rm d}$ dependence of $\rho_{\rm c}$ at non-alloyed Ti and Mg contacts formed on P^+-implanted SiC is shown by symbols in Fig. 5.8. For the highest $N_{\rm P}$ of $2.3 \times 10^{20}\,{\rm cm}^{-3}$, the $N_{\rm d}$ value is treated as 75% of $N_{\rm P}$ (i.e., $N_{\rm d} = 1.7 \times 10^{20}\,{\rm cm}^{-3}$) based on the reported activation ratio of the implanted P atoms in SiC (60–90%) [13, 14]. Regarding the $\phi_{\rm B0}$ dependence of $\rho_{\rm c}$, a lower $\rho_{\rm c}$ is obtained for the Mg contacts ($\phi_{\rm B0} \simeq 0.7\,{\rm eV}$) than Ti ($\phi_{\rm B0} \simeq 1.0\,{\rm eV}$). As discussed above, the difference in $\rho_{\rm c}$ between the Ti and Mg electrodes becomes smaller at a higher $N_{\rm d}$, reflecting a less $\phi_{\rm B0}$-dependent barrier thickness. As for the dependency on $N_{\rm d}$, $\rho_{\rm c}$ decreases with increasing $N_{\rm d}$, and at a very high $N_{\rm d}$ ($1.7 \times 10^{20}\,{\rm cm}^{-3}$), an extremely

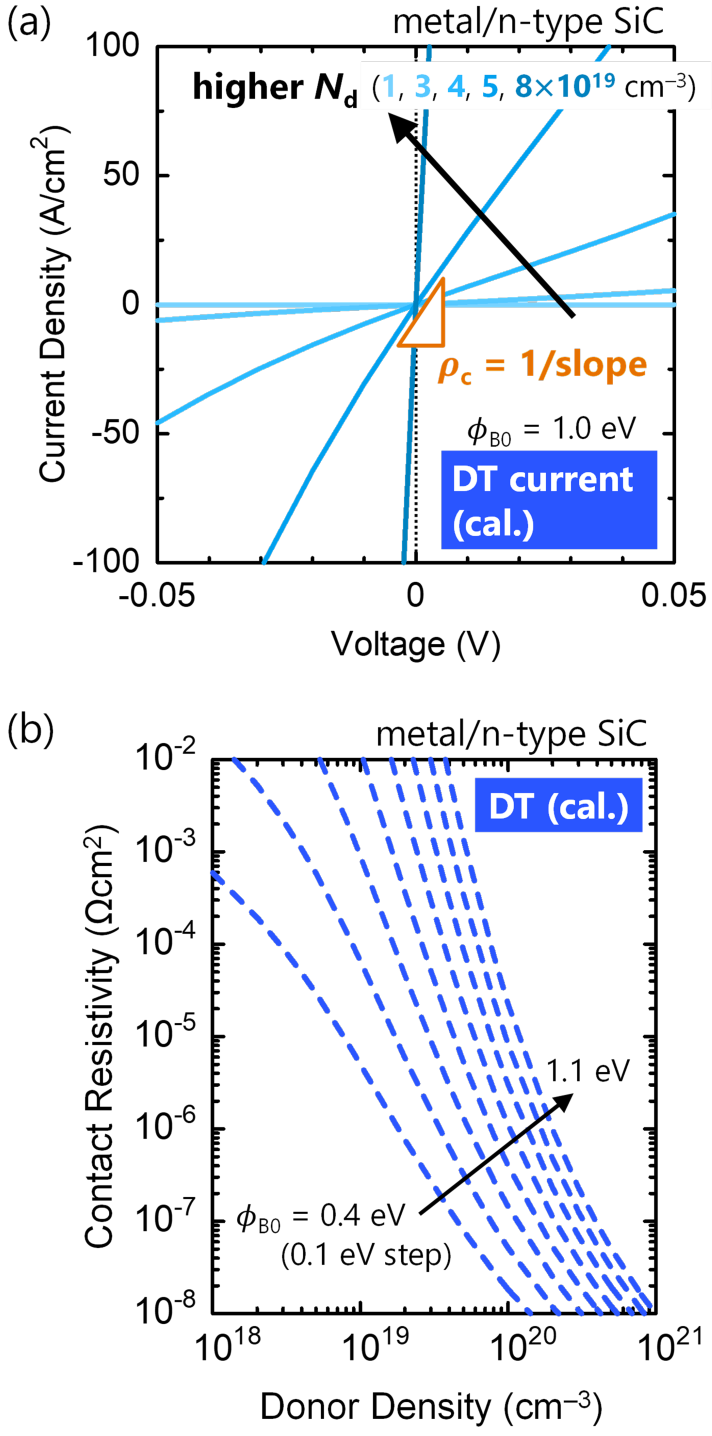

Figure 5.7: (a) I–V characteristics calculated based on the direct tunneling (DT) model assuming $\phi_{B0} = 1.0\,\mathrm{eV}$ and varying N_d (1×10^{19}–$8 \times 10^{19}\,\mathrm{cm}^{-3}$). (b) Contact resistivity at metal/n-type SiC interfaces calculated based on the DT model as a function of the donor density assuming various ϕ_{B0} (0.4–1.1 eV).

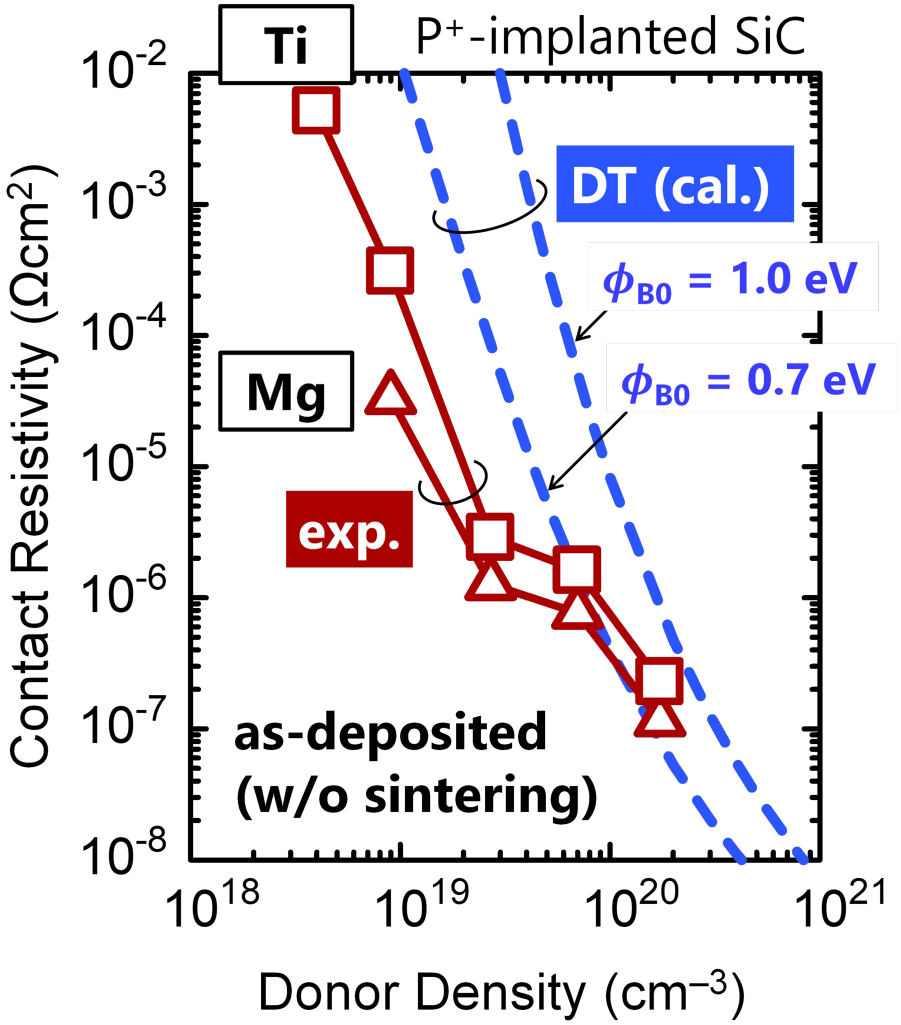

Figure 5.8: Donor density dependence of the contact resistivity experimentally obtained for non-alloyed Ti and Mg contacts formed on heavily P^+-implanted SiC (symbols) and calculated based on the direct tunneling (DT) model (dashed lines).

low ρ_c of $1 \times 10^{-7}\,\Omega\text{cm}^2$ or $2 \times 10^{-7}\,\Omega\text{cm}^2$ is achieved for the non-alloyed Mg or Ti contact, respectively. These values are comparable to or even lower than those obtained for the practical Ni-based alloyed ohmic contacts formed by performing high-temperature sintering (~ 1000°C).

The blue dashed lines in Fig. 5.8 present the DT-based ρ_c as a function of N_d calculated assuming $\phi_{B0} = 0.7$ and 1.0 eV, corresponding to the barrier heights at the Mg and Ti contacts, respectively. Through the comparison of ρ_c between the experiment and the DT-based calculation, it is discussed how the dominant tunneling process (DT or TAT) changes depending on N_d and how the changes have an impact on ρ_c in terms of the value itself and the N_d dependence. Based on the experimental and calculated data, the N_d range is divided into three parts: (i) $N_d <$ low-$10^{19}\,\text{cm}^{-3}$, (ii) N_d in mid-$10^{19}\,\text{cm}^{-3}$, and (iii) $N_d >$ high-$10^{19}\,\text{cm}^{-3}$. The author focuses on the basic concept of the tunneling phenomena introduced in Chap. 3 (i.e., the tunneling current is determined as the product of the tunneling probability and the energy distribution of carriers), and then modeling of ρ_c at non-alloyed contacts on P^+-implanted SiC is performed considering the contributions of DT and TAT in each N_d range.

5.4.2 Contribution of Direct Tunneling and Trap-Assisted Tunneling

Figure 5.9 schematically depicts the tunneling probability for DT [$P_{DT}(E)$] and TAT [$P_{TAT}(E)$], the Fermi-Dirac distribution function, and the tunneling current as a function of the electron energy in each N_d range. Note that $P_{TAT}(E)$ is depicted excluding the factor $N_T\sigma_T$ in Eq. (4.1), where N_T is the trap density, and σ_T is the capture cross section of the trap, respectively. In other words, the schematic illustration for $P_{TAT}(E)$ only considers the electrons that encounter a trap. The energy where the electron tunneling most frequently occurs (defined as E_{peak}) is also indicated in Fig. 5.9 because the magnitude relationship between E_{peak} and the conduction band edge (E_C) or the Fermi level in the metal (E_{Fm}) is a crucial part of the discussion.

(i) $N_d <$ low-$10^{19}\,\text{cm}^{-3}$:

In this N_d range with 1–2 $\times 10^{19}\,\text{cm}^{-3}$ or lower, the measured ρ_c values are much lower than those expected from the DT model, and a sharp decrease in ρ_c according to the N_d increase having almost the same slope as the calculated ρ_c–N_d plots is observed. With such a moderate or relatively high N_d, E_{peak} for DT and TAT near 0 V are both higher than E_C or E_{Fm} (i.e., TFE regime). Since $P_{TAT}(E)$ is several orders of magnitude higher than $P_{DT}(E)$ at a given energy, E_{peak} for TAT is kept lower than that for DT, resulting in a much larger current thanks to the contribution of a more significant number of carriers through the TAT process, as depicted in Fig. 5.9(i). The E_{peak} shift toward a lower energy side and the enhanced tunneling current by TAT can be regarded as if the DT current were increased by barrier height lowering. Based on Fig. 5.7, the experimental data for the Ti and Mg

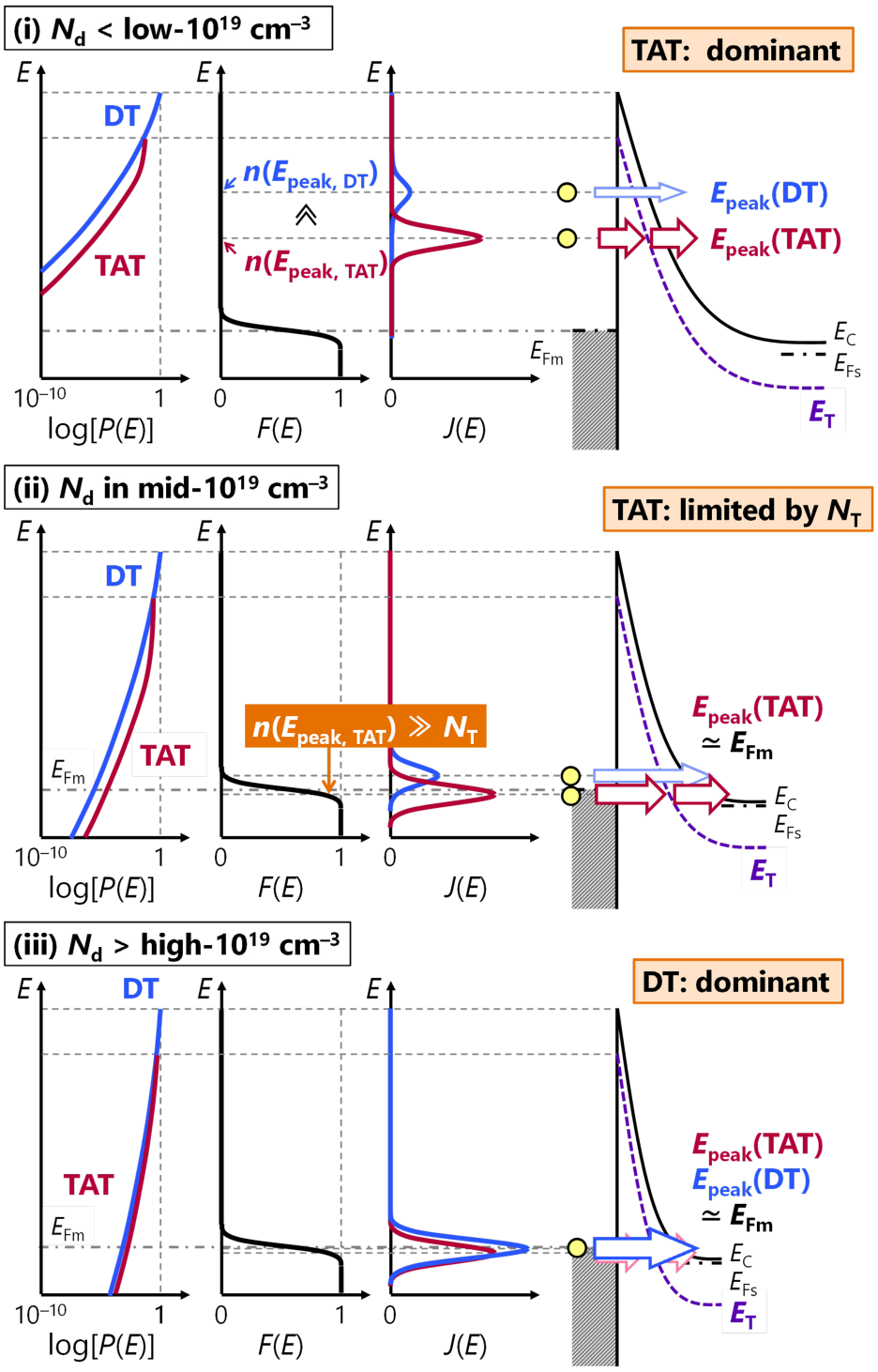

Figure 5.9: Schematic illustrations of how the contributions of direct tunneling (DT) and trap-assisted tunneling (TAT) change depending on the donor density based on the tunneling probability, Fermi-Dirac distribution function, and tunneling current in the donor density range of (i) below low-10^{19} cm^{-3}, (ii) in mid-10^{19} cm^{-3}, and (iii) above high-10^{19} cm^{-3}.

contacts are similar to the DT-based ρ_c values calculated with $\phi_{B0} = 0.5$–$0.6\,\mathrm{eV}$ and 0.4–$0.5\,\mathrm{eV}$. These values are close to about half of the actual ϕ_{B0}, which is reasonably consistent with the expectation regarding the dominant trap levels for the TAT current presented in Chap. 4. These descriptions help understand why the measured ρ_c is much lower than the calculated value based on DT, and the slopes in the experimental ρ_c–N_d plots are similar to those from the DT-based calculation.

(ii) N_d in mid-$10^{19}\,\mathrm{cm}^{-3}$:

At a very high N_d in the mid-$10^{19}\,\mathrm{cm}^{-3}$ range, the measured ρ_c is still lower than the calculated values based on DT but shows a slower decrease with increasing N_d. With such a high N_d, E_{peak} for TAT shifts toward E_C or E_{Fm} (i.e., FE regime), where many carriers occupy most electronic states with the occupancy almost equal to unity. Since the implantation-induced trap density is expected to be as high as 1/100 of N_d [15], the carrier density near E_{peak} ($> 10^{19}\,\mathrm{cm}^{-3}$) should be much higher than N_T, as indicated in Fig. 5.9(ii). As a result, only a tiny number of electrons is allowed to pass through the traps, and the TAT current becomes saturated with the limitation by N_T even if the tunneling probability becomes higher with increasing N_d. Thus, the experimental ρ_c has a weaker N_d dependence in this high N_d range, while the ρ_c value is still lower than the DT-based one.

(iii) $N_d >$ high-$10^{19}\,\mathrm{cm}^{-3}$:

With an extremely high N_d over high-$10^{19}\,\mathrm{cm}^{-3}$ or $10^{20}\,\mathrm{cm}^{-3}$, the experimental and calculated ρ_c become very close to each other and both sharply decrease with increasing N_d. When making N_d that high, E_{peak} for TAT and DT are both located at E_C or E_{Fm}, and the probabilities for TAT and DT become very high and comparable to each other at E_{peak}. In this situation, electrons can directly tunnel through the Schottky barrier with a very high probability without passing through the trap. As a result, DT becomes even more predominant over TAT because the DT process is irrelevant to N_T. Hence, the carrier transport in the extremely high N_d range is dominated by DT instead of TAT, leading to a sharp decrease in ρ_c toward a very low value of $10^{-7}\,\Omega\mathrm{cm}^2$.

Through the above discussions, the contributions of DT and TAT can be schematically expressed as plotted in Fig. 5.10 by the blue and red dashed lines, respectively. As the sum of these components, a physical model to predict ρ_c at non-alloyed ohmic contacts formed on ion-implanted SiC is proposed, as given by the black solid line in Fig. 5.10. Based on this proposed model, several guidelines for low-resistance non-alloyed ohmic contacts on SiC are presented in the next section.

5.4.3 Design Guidelines for Non-Alloyed Ohmic Contacts on *n*-Type SiC

One crucial fact is that ion implantation should be adopted rather than epitaxial growth to form contact regions. This is not only because ion implantation can achieve a higher N_d than

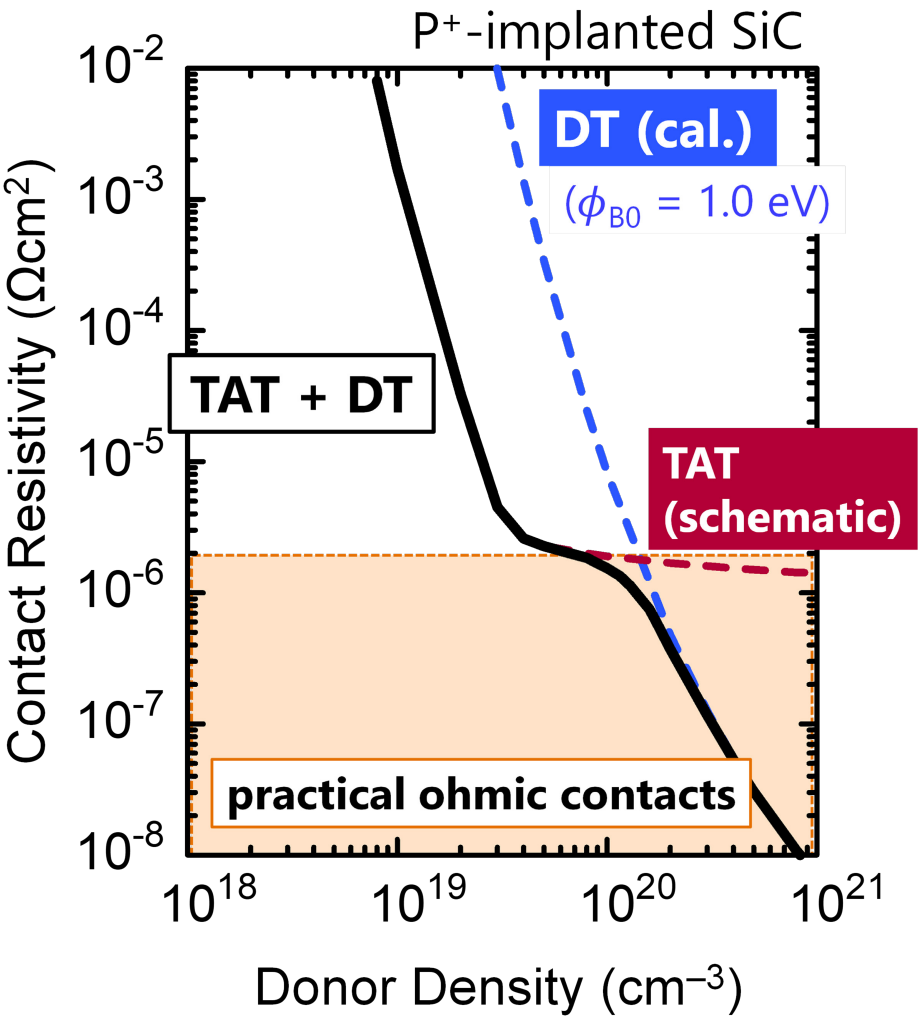

Figure 5.10: Contact resistivity modeling for non-alloyed ohmic contacts formed on P^+-implanted SiC, considering the contributions of DT (blue dashed line) and TAT (red dashed line).

epitaxial growth but also because it can effectively utilize the advantage of a significantly large current attributed to TAT. Regarding the doping density and barrier height, a ρ_c value in a low-$10^{-6}\,\Omega\mathrm{cm}^2$ range can be obtained by making N_d higher than about $3\times10^{19}\,\mathrm{cm}^{-3}$ and ϕ_{B0} lower than about 1.0 eV, which is qualitatively explained by the contribution of TAT. Besides, very high-dose ion implantation ($> 10^{20}\,\mathrm{cm}^{-3}$) even makes it possible to achieve an extremely low ρ_c ($< 10^{-7}\,\Omega\mathrm{cm}^2$) without high-temperature sintering (~ 1000°C), which is quantitatively predictable with the numerical calculation of the DT current. Consequently, quantitative guidelines regarding N_d and ϕ_{B0} to reduce ρ_c at non-alloyed ohmic contacts have been suggested based on a physical model considering the contributions of DT and TAT.

5.5 Discussion

The author has to emphasize that while the main focus of this chapter was on the formation and characterization of non-alloyed ohmic contacts, it is preferable to perform a low-temperature thermal treatment (e.g., sintering at about 500–600°C) after the metallization, from the practical point of view. This is because, in the actual device fabrication, devices are usually exposed to heat ($\sim$ 500–600°C) after the metallization to deposit a dielectric film for the metal interconnect isolation. This kind of thermal treatment may cause changes in the electrical properties of non-alloyed (non-sintered) ohmic contacts. Therefore, it is indispensable to investigate how the post-metallization sintering affects the ρ_c value, starting with the case of non-alloyed ohmic contacts presented in this study and systematically elevating the sintering temperature. It should be noted that careful structural analyses conventionally done in previous studies on SiC ohmic contacts [1–3] are essential in characterizing sintered metal/SiC contacts. Combining the analyses of tunneling phenomena and interfacial reactions will help to clarify how the proposed model for non-alloyed SiC ohmic contacts should be modified, giving quite beneficial guidelines in exploring a novel fabrication process alternative to the currently available high-temperature sintering (~ 1000°C). Furthermore, it will also be expected to provide critical insights into fully understanding the formation mechanism of the conventional alloyed ohmic contacts on SiC.

In any case of non-alloyed or alloyed ohmic contacts, the barrier height reduction is an effective way to achieve a low ρ_c. The ρ_c modeling presented in this study gives a guideline concerning the barrier height: a ρ_c value can be reduced as low as $10^{-6}\,\Omega\mathrm{cm}^2$ by making ϕ_{B0} lower than about 1 eV. While Ti electrodes ($\phi_{B0} \simeq 1$ eV) are promising for the practical ohmic contacts (probably even when annealed at 500–600°C), lower ϕ_{B0} is more favorable to make the ρ_c value as low as possible. Although just choosing an electrode metal with a low work function (ϕ_m) is a simple way to reduce ϕ_{B0}, most low-ϕ_m metals, including Mg, are chemically unstable with a low melting temperature, low tolerance to oxidation, and so forth. In this perspective, the author believes that inserting an interfacial

layer between metal and SiC is a promising alternative for barrier height reduction. An interesting result regarding the interlayer-based ohmic contact formation was reported by Mohammad *et al.* [16], in which an indium nitride (InN) film is introduced to a Ti/n-type SiC interface, and $\rho_c = 1.8 \times 10^{-4}\,\Omega\mathrm{cm}^2$ is achieved without sintering. As partly pointed out in the article [16], the requirements for a semiconductor-based interfacial layer are as follows:

(1) The interlayer and SiC should have proper band alignment.
(2) To reduce the barrier height, the interlayer and SiC should have the same conductivity type, and the doping density in the interlayer should be as high as possible.
(3) The barrier height between the interlayer and electrode metal should also be sufficiently low, ensuring an ohmic characteristic.
(4) Formation of the metal/interlayer/SiC stack is preferable to be performed at a moderate temperature (500–600°C).

In Ref. [16], TLM structures were fabricated on an n-type SiC epitaxial layer with $N_d = 1 \times 10^{19}\,\mathrm{cm}^{-3}$. Thus, it is crucial to investigate further the effect of the InN film insertion on the ohmic contact formation and ρ_c reduction by utilizing heavily P^+-implanted SiC. Besides, the author regards heavily-doped n-type silicon (Si) as a promising candidate to achieve a low ρ_c as well, thanks to the good band alignment for the n-Si/n-SiC junction (electron affinity of Si: 4.0 eV [17]) and mature contact formation process regarding the metal/Si interface. Several recent trials by the author for barrier height reduction at contacts by inserting Si interlayers are described in Appendix B. Exploration of an interfacial layer suitable for ρ_c reduction and optimization of the interlayer-based ohmic contact formation process are also critical future prospects.

From another viewpoint involved in effectively utilizing the TAT phenomenon, the author also suggests a new concept for low-resistance ohmic contacts by intentionally creating deep levels in contact regions. Although the TAT contribution is advantageous regarding the ρ_c reduction, as mentioned above, it is almost impossible to control the kind, density, and depth profile of the implantation-induced deep levels. Thus, it may be effective to perform ion implantation for an additional impurity atom, which forms a deep level in the bandgap of SiC, in addition to the dopant atom implantation. Intentionally introducing deep levels may make it easier to predict the TAT current and design ohmic contacts. In this sense, the author focuses on the sulfur (S) impurity, which acts as a deep donor in SiC [18, 19] and whose depth profile is controllable by ion implantation [19]. Note that the additionally implanted atoms do not necessarily act as dopants; the point is just on forming "deep levels." Considering the significant contribution of TAT in the N_d range of low- to mid-$10^{19}\,\mathrm{cm}^{-3}$, this concept may help to achieve a very low ρ_c without performing very high-dose dopant implantation ($\sim 10^{20}\,\mathrm{cm}^{-3}$), which requires high-temperature implantation and, thereby, a high process cost. Several data regarding contact formation on P and S co-implanted SiC are also presented in Appendix B. While priority should be given to identifying the trap levels that dominantly contribute to the TAT current and quantitative

modeling of the TAT phenomenon at metal/heavily P^+-implanted SiC interfaces, the author believes that the proposed concept will help develop the ohmic contact formation process and reduce the device fabrication cost.

Finally, it should be mentioned how different the situation is regarding a non-alloyed ohmic contact on p-type SiC. Recently, Kuwahara *et al.* carefully investigated ρ_c at non-alloyed contacts formed on heavily Al^+-implanted p-type SiC (implanted Al atom density: $N_{Al} = 1\times10^{19}$–$5\times10^{20}\,cm^{-3}$) [20]. Thanks to the contribution of the TAT and split-off band holes with a light effective mass ($0.2m_0$) [21], a nearly ohmic-like linear I–V relationship was obtained, and a low ρ_c of $9.8\times10^{-3}\,\Omega cm^2$ at $N_{Al} = 5\times10^{20}\,cm^{-3}$ was achieved for Ni contacts without performing any thermal treatment. On the other hand, Ref. [20] also reported a severe out-diffusion of the implanted Al atoms during activation annealing (1750°C) and incomplete activation of the Al atoms (less than 40% when $N_{Al} > 10^{20}\,cm^{-3}$), making it challenging to design and fabricate ohmic contacts. Besides, the Schottky barrier height at a metal/p-type SiC interface is intrinsically high (typically higher than 1.2 eV [22]). Therefore, a low-temperature sintering- or interlayer-based ohmic contact formation has to be relied on for ρ_c reduction, which should be further studied in the future, as is the case of n-type SiC. At the same time, based on the extensive exploration of a novel fabrication process for n- and p-type individual ohmic contacts, establishing an optimum fabrication process for simultaneous ohmic contacts on n- and p-type SiC is also a crucial future prospect.

5.6 Summary

This chapter systematically investigated the contact resistivity (ρ_c) at non-alloyed Ti and Mg contacts formed on heavily P^+-implanted SiC ($N_d > 4\times10^{18}\,cm^{-3}$) through the experimental characterization with CTLM structures and numerical calculation of the direct tunneling (DT) current. In the N_d range below mid-$10^{19}\,cm^{-3}$ (4×10^{18}–$7\times10^{19}\,cm^{-3}$), the experimental ρ_c was much lower than that expected from the DT model, which is qualitatively explained by the significant contribution of trap-assisted tunneling (TAT). At a further higher N_d above $10^{20}\,cm^{-3}$, on the other hand, the ρ_c value sharply decreased with increasing N_d in good agreement with the calculated DT-based ρ_c. It was demonstrated that an extremely low ρ_c of 1–$2\times10^{-7}\,\Omega cm^2$ is achievable for the Mg and Ti contacts without performing high-temperature sintering ($\sim$ 1000°C) by utilizing very high-dose P^+ implantation ($2\times10^{20}\,cm^{-3}$). Based on the experiment and calculation, a physics-based model for predicting ρ_c at non-alloyed ohmic contacts on ion-implanted SiC was proposed, carefully considering the contributions of DT and TAT. Consequently, a design guideline concerning the barrier height and donor density for low-resistance non-alloyed ohmic contacts on n-type SiC was suggested; the zero-field barrier height (ϕ_{B0}) as low as or lower than about 1.0 eV and N_d higher than about $3\times10^{19}\,cm^{-3}$ allow to achieve a very low ρ_c ($< 10^{-6}\,\Omega cm^2$).

The data, model, and design guidelines regarding the non-alloyed ohmic contacts can provide essential future prospects for establishing a novel low-temperature fabrication process for low-resistance SiC ohmic contacts.

References

[1] L. M. Porter and R. F. Davis, *Mater. Sci. Eng. B* **34**, 83 (1995).

[2] J. Crofton, L. M. Porter, and J. R. Williams, *Phys. Stat. Sol. B* **202**, 581 (1997).

[3] F. Roccaforte, F. La Via, and V. Raineri, *Int. J. High Speed Electron. Syst.* **15**, 781 (2005).

[4] S. Tanimoto and H. Ohashi, *Phys. Stat. Sol. A* **206**, 2417 (2009).

[5] S. Tanimoto, J. Senzaki, Y. Hayami, H. Hoshi, and H. Okushi, *Extended Abstract of the Symposium on Future Electron Devices*, Vol. 172 (2000), p. 107.

[6] H. Shimizu, A. Shima, Y. Shimamoto, and N. Iwamuro, *Jpn. J. Appl. Phys.* **56**, 04CR15 (2017).

[7] T. Doi, S. Shibayama, M. Sakashita, K. Kojima, M. Shimizu, and O. Nakatsuka, *Appl. Phys. Express* **15**, 015501 (2022).

[8] G. K. Reeves, *Solid State Electron.* **23**, 487 (1980).

[9] D. K. Schroder, *Semiconductor Material and Device Characterization* (John Wiley & Sons, 3rd edition, 2005).

[10] Y. Negoro, K. Katsumoto, T. Kimoto, and H. Matsunami, *J. Appl. Phys.* **96**, 224 (2004).

[11] F. A. Padovani and R. Stratton, *Solid State Electron.* **9**, 695 (1966).

[12] A. Y. C. Yu, *Solid State Electron.* **13**, 239 (1970).

[13] M. Laube, F. Schmid, G. Pensl, G. Wagner, M. Linnarsson, and M. Maier, *J. Appl. Phys.* **92**, 549 (2002).

[14] J. Senzaki, K. Fukuda, and K. Arai, *J. Appl. Phys.* **94**, 2942 (2003).

[15] K. Kawahara, J. Suda, G. Pensl, and T. Kimoto, *J. Appl. Phys.* **108**, 033706 (2010).

[16] F. A. Mohammad, Y. Cao, and L. M. Porter, *J. Electron. Mater.* **36**, 312 (2007).

[17] S. M. Sze, Y. Li, and K. K. Ng, *Physics of Semiconductor Devices* (John Wiley & Sons, 4th edition, 2021).

[18] S. A. Reshanov, G. Pensl, H. Nagasawa, and A. Schöner, *J. Appl. Phys.* **99**, 123717 (2006).

[19] T. Matsuoka, M. Kaneko, and T. Kimoto, *Jpn. J. Appl. Phys.* **62**, 010908 (2023).

[20] K. Kuwahara, T. Kitawaki, M. Hara, M. Kaneko, and T. Kimoto, *International Conference on Silicon Carbide and Related Materials 2023* (Sorrento, 2023), Process 6-3.

[21] T. Kitawaki, M. Hara, H. Tanaka, M. Kaneko, and T. Kimoto, *Appl. Phys. Express* **16**, 031005 (2023).

[22] T. Kimoto and J. A. Cooper, *Fundamentals of Silicon Carbide Technology: Growth, Characterization, Devices and Applications* (John Wiley & Sons, 2014).

Chapter 6

Conclusions

6.1 Summary of This Thesis

In this thesis, the author systematically investigated the barrier height and high-field carrier transport phenomena in Schottky structures formed on heavily-doped n-type SiC and proposed a design guideline for low-resistance non-alloyed ohmic contacts based on a physical understanding of metal/heavily-doped SiC interfaces. The main conclusions gained in the present study are summarized as follows.

In Chapter 2, the Schottky barrier height at a metal/heavily-doped n-type SiC interface was characterized with three different techniques: internal photoemission (IPE), capacitance–voltage (C–V), and current–voltage (I–V) measurements. The barrier height at zero bias (ϕ_{B}) decreased with increasing the donor density (N_{d}), the difference of which was about 0.2 eV between the Ni/SiC Schottky barrier diodes (SBDs) with $N_{\mathrm{d}} = 7 \times 10^{15}$ and $2 \times 10^{19}\,\mathrm{cm}^{-3}$. The barrier height drop quantitatively agreed with the image force lowering ($\Delta\phi = 0.18\,\mathrm{eV}$) caused by a high electric field ($>$ MV/cm) resulting from a thin Schottky barrier ($\sim 10\,\mathrm{nm}$), even at zero bias. Besides, the *zero-field barrier height* (ϕ_{B0}), defined without including the image force effect, was almost constant regardless of N_{d}. The higher electric field also induces the forward tunneling current described by the thermionic field emission (TFE) model, and the TFE-based analysis of the forward I–V characteristics allowed a consistent barrier height with IPE and C–V measurements to be obtained. Employing Mg, Ti, and Ni as Schottky electrodes (metal work function: $\phi_{\mathrm{m}} = 3.7$, 4.0, and 5.2 eV, respectively) clarified that the barrier height in a metal/n-type SiC interface is controllable in a wide range ($\phi_{\mathrm{B0}} \simeq 0.7$–$1.6\,\mathrm{eV}$), irrelevant to N_{d}.

In Chapter 3, the author investigated the direct tunneling (DT) phenomenon in Schottky structures formed on heavily-doped SiC epitaxial layers, including both the TFE and field emission (FE) transport ascribed to tunneling of thermal and cold electrons, respectively. Based on the numerical calculation of DT current, the forward and reverse I–V characteristics of the vertical SBD structures fabricated using heavily-doped n-type SiC epitaxial layers ($N_{\mathrm{d}} = 10^{17}$–$10^{19}\,\mathrm{cm}^{-3}$) were well reproduced in a very wide range of the

current density (10^{-6}–1 A/cm^2) for each N_d and ϕ_{B0}. Through the investigation of the energy where electron tunneling most frequently occurs (defined as E_{peak}), it was revealed that the TFE transport is dominant in the heavily-doped SiC SBDs ($N_\mathrm{d} > 10^{17}\,\mathrm{cm}^{-3}$) under a forward bias, while the dominant DT process changes from TFE to FE in reverse-biased heavily-doped SiC SBDs (N_d: above mid-$10^{18}\,\mathrm{cm}^{-3}$), due to a higher electric field. The critical electric field for the TFE-FE transition was uniquely determined for a given ϕ_{B0} irrelevant to N_d by carefully considering the sharply changing electric field distribution in heavily-doped SiC Schottky structures. From a more universal aspect, the critical thickness of a Schottky barrier for the TFE-FE transition was given as 4–7 nm at the energy of the Fermi level in a metal, almost regardless of both N_d and ϕ_{B0}.

In Chapter 4, Schottky structures were formed on heavily phosphorus ion (P^+)-implanted n-type SiC (P atom density: $N_\mathrm{P} = 1 \times 10^{17}$–$8 \times 10^{19}\,\mathrm{cm}^{-3}$), and differences in electrical properties were compared with those on epitaxial layers. C–V measurement revealed that the implanted P atoms are almost perfectly activated as donors (activation ratio: over 90%), even at a very high N_P of $3 \times 10^{19}\,\mathrm{cm}^{-3}$. The barrier height at metal/P^+-implanted SiC interfaces was also characterized through C–V measurement, and nearly identical values were obtained for the ion-implanted and epitaxial layers. The current density in the P^+-implanted SiC SBDs was several orders of magnitude larger than that in the epitaxial SiC SBDs, even with a similar N_d and ϕ_{B0}, which is likely attributed to trap-assisted tunneling (TAT) via implantation-induced deep levels. The trap levels that dominantly contribute to the TAT process were speculated for various applied voltage conditions through the numerical calculation of the TAT current.

In Chapter 5, the contact resistivity (ρ_c) at non-alloyed Ti and Mg contacts formed on heavily P^+-implanted SiC ($N_\mathrm{P} = 4 \times 10^{18}$–$2 \times 10^{20}\,\mathrm{cm}^{-3}$) was systematically investigated based on the experimental characterization using circular transmission line model (CTLM) structures and numerical calculation of the DT current. The ρ_c value experimentally determined was much lower than that expected from the DT calculation when N_d is below mid-$10^{19}\,\mathrm{cm}^{-3}$, which is qualitatively explained by the significant contribution of TAT. In a higher N_d range above $10^{20}\,\mathrm{cm}^{-3}$, on the other hand, the measured ρ_c agreed well with the sharply decreasing ρ_c calculated based on the DT model, and an extremely low ρ_c of 1–$2 \times 10^{-7}\,\Omega\mathrm{cm}^2$ was achieved for non-alloyed Mg and Ti ohmic contacts with a very high N_P of $2 \times 10^{20}\,\mathrm{cm}^{-3}$. Through careful consideration regarding the contributions of DT and TAT, ρ_c modeling in terms of the dependency on N_d and ϕ_{B0} for non-alloyed ohmic contacts was established. The proposed model provided a quantitative guideline concerning the barrier height ($\phi_{\mathrm{B0}} \leq 1\,\mathrm{eV}$) and donor density ($N_\mathrm{d} \geq 3 \times 10^{19}\,\mathrm{cm}^{-3}$) for designing low-resistance non-alloyed ohmic contacts ($\rho_\mathrm{c} < 10^{-6}\,\Omega\mathrm{cm}^2$) formed on P^+-implanted SiC.

The present data, physics-based model, and design guidelines for non-alloyed metal/heavily-doped SiC interfaces contribute to resolving critical issues in the ohmic contact formation on SiC, namely, establishing a novel fabrication process for low-resistance ohmic contacts with a low thermal budget and clarifying the formation mechanism of alloyed

ohmic contacts sintered at a very high temperature (~ 1000°C). In addition, the high-field phenomena at the metal/heavily-doped SiC interfaces are expected to be commonly observed in Schottky structures fabricated on other wide-bandgap semiconductor materials. Thus, the author believes that the present study also leads to a deeper understanding of the ohmic contact formation on them and helps improve their fabrication process as well.

6.2 Future Outlook

The author has clarified the fundamental properties of non-alloyed metal/heavily-doped SiC interfaces and has demonstrated the potential applicability of a low-temperature fabrication process for low-resistance ohmic contacts on SiC. On the other hand, research subjects to be further studied and critical issues to be resolved still remain, as listed below.

1. **Full understanding of the direct tunneling phenomena in heavily-doped n- and p-type SiC Schottky structures**

   This study extensively investigated the DT current through heavily-doped n-type SiC Schottky contacts for various N_{d}, ϕ_{B0}, and applied voltage (i.e., electric field). Besides, a unique tunneling phenomenon in heavily-doped p-type SiC SBDs reported from the author's group [1] was also introduced, which is described by tunneling of the split-off band holes with a light effective mass ($0.2m_0$). At the present stage, on the other hand, all the I–V characteristics were taken at room temperature. Since an ambient temperature is also a critical factor that significantly influences the tunneling process [2, 3], investigation of the temperature dependence of the I–V characteristics of heavily-doped SiC Schottky structures is vital. Especially for the hole tunneling through metal/heavily-doped p-type SiC interfaces, the tunneling current should be more sensitive to the temperature because the split-off band is located at a higher energy (about 60 meV from the band edge) in the valence band in SiC [4]. Since the tunneling process strongly correlates to ρ_{c} at ohmic contacts, the DT current in both heavily-doped n- and p-type SiC Schottky structures should be further studied in terms of the dependency on N_{d}, ϕ_{B0}, electric field, and temperature, which will give a helpful insight into the ρ_{c} analysis for ohmic contacts.

2. **Quantitative analysis of the trap-assisted tunneling current through Schottky contacts formed on heavily ion-implanted SiC**

   Chapters 4 and 5 pointed out the contribution of TAT to explain a significantly larger current and much lower ρ_{c} at the contacts on heavily P^+-implanted SiC than those on epitaxial layers. The author's group recently reported an enhanced tunneling current through metal/heavily Al^+-implanted SiC interfaces [5]. However, discussions on the TAT current remain qualitative mainly due to a poor understanding of defect properties in heavily ion-implanted SiC ($> 1 \times 10^{18}\,\mathrm{cm}^{-3}$). Besides, it seems that some

modifications are required for the numerical formula of TAT current: for instance, the way to convert the unit of trap density from the volume density to area density, accurately treating the energy conservation during the trapping/emitting process for deep levels, considering the thermal excitation of the trapped carriers, and so on. These aspects must be addressed for fully modeling the TAT phenomenon in metal/heavily ion-implanted SiC interfaces and quantitatively predicting ρ_c at non-alloyed ohmic contacts in a doping density range of mid-$10^{19}\,\mathrm{cm}^{-3}$.

3. **Establishing a low-temperature formation process for both individual and simultaneous ohmic contacts on n- and p-type SiC**

   The present study proposed a design guideline regarding ϕ_{B0} and N_d to achieve a low ρ_c ($< 10^{-6}\,\Omega\mathrm{cm}^2$) for non-alloyed ohmic contacts formed on heavily P^+-implanted n-type SiC. On the other hand, a low-temperature thermal treatment at about 500–600°C is performed after the metallization in the actual device fabrication process. Therefore, a new formation process for low-resistance and stable ohmic contacts on n-type SiC has to be explored mainly based on a metal/SiC interface and a metal/interlayer/SiC stack sintered at a low temperature, by combining the understanding of the tunneling phenomena (presented in this study) and analysis of interfacial reactions (extensively conducted so far [6–8]), as in detail discussed in Chap. 5. As for p-type SiC ohmic contacts, meanwhile, a high Schottky barrier at metal/p-type SiC contacts (typically higher than 1.2 eV [9]) makes it more difficult to obtain a sufficiently low ρ_c ($\sim 10^{-6}\,\Omega\mathrm{cm}^2$) at non-alloyed contacts [5], and the situation is expected to be almost identical even when low-temperature sintering is performed. Besides, formation of low-resistance simultaneous ohmic contacts on n- and p-type SiC is challenging because it is almost impossible to form a low Schottky barrier both for n- and p-type SiC just by depositing an electrode. From these points of view, unfortunately, it is still far from adopting a low-temperature process to practical device fabrication, and intensive research on exploring a novel fabrication process is further required. However, the author believes that a step-by-step pile of the physical understanding of metal/heavily-doped SiC contacts, including both the tunneling phenomena and interfacial reactions, should one day lead to a breakthrough in the ohmic contact formation process.

References

[1] T. Kitawaki, M. Hara, H. Tanaka, M. Kaneko, and T. Kimoto, *Appl. Phys. Express* **16**, 031005 (2023).

[2] E. L. Murphy and R. H. Good, *Phys. Rev.* **102**, 1464 (1956).

[3] F. A. Padovani and R. Stratton, *Solid State Electron.* **9**, 695 (1966).

[4] H. Tanaka, S. Asada, T. Kimoto, and J. Suda, *J. Appl. Phys.* **123**, 245704 (2018).

[5] K. Kuwahara, T. Kitawaki, M. Hara, M. Kaneko, and T. Kimoto, *International Conference on Silicon Carbide and Related Materials 2023* (Sorrento, 2023), Process 6-3.

[6] L. M. Porter and R. F. Davis, *Mater. Sci. Eng. B* **34**, 83 (1995).

[7] J. Crofton, L. M. Porter, and J. R. Williams, *Phys. Stat. Sol. B* **202**, 581 (1997).

[8] F. Roccaforte, F. La Via, and V. Raineri, *Int. J. High Speed Electron. Syst.* **15**, 781 (2005).

[9] T. Kimoto and J. A. Cooper, *Fundamentals of Silicon Carbide Technology: Growth, Characterization, Devices and Applications* (John Wiley & Sons, 2014).

Appendix A

Calculation of Fermi Level and Carrier Density

This chapter briefly introduces the calculation procedure for Fermi level and carrier density in a semiconductor [1, 2]. Starting with the fundamental equations of statistical mechanics in a solid-state material, the calculation based on the Boltzmann approximation, which is valid for non-degenerate (lightly-doped) semiconductors, is explained, followed by the case of degenerate (heavily-doped) semiconductors for which self-consistent computation is required.

A.1 Fundamental Equations

The electron density (n_{e}) in the conduction band is obtained by taking the integral for the product of the density of states [$N(E)$] and the occupancy [$F(E)$],

$$n_{\mathrm{e}} = \int_{E_{\mathrm{C}}}^{\infty} N(E)F(E)\mathrm{d}E. \tag{A.1}$$

Here, $N(E)$ is given by

$$N(E) = \frac{M_{\mathrm{C}}}{2\pi^2}\left(\frac{2m^*_{\mathrm{dse}}}{\hbar^2}\right)^{3/2}\sqrt{E - E_{\mathrm{C}}}, \tag{A.2}$$

and $F(E)$ is the Fermi-Dirac distribution function expressed as

$$F(E) = \frac{1}{1 + \exp\left(\dfrac{E - E_{\mathrm{Fs}}}{k_{\mathrm{B}}T}\right)}. \tag{A.3}$$

Here, $\hbar$ is the Dirac constant, k_{B} is the Boltzmann constant, T is the absolute temperature, E is the electron energy, E_{C} is the conduction band edge, M_{C} is the number of equivalent conduction band minima, E_{Fs} is the Fermi level in the semiconductor, and m^*_{dse} is the density-of-state effective mass, respectively. m^*_{dse} is calculated as $m^*_{\mathrm{dse}} = (m^*_{\mathrm{ML}}m^*_{\mathrm{M\Gamma}}m^*_{\mathrm{MK}})^{1/3}$, using the effective mass at E_{C} along ML, MΓ, and MK directions.

When impurity atoms are introduced to the semiconductor, the total negative charges (electrons and ionized acceptors) and positive charges (holes and ionized donors) must be balanced. In the case of n-type SiC with the net donor density N_d, the hole density is extremely low ($p_\mathrm{h} = n_\mathrm{i}^2/n_\mathrm{e} < 10^{-30}\,\mathrm{cm}^{-3}$, where n_i is the intrinsic carrier density). Thus, the charge neutrality equation is expressed as

$$n_\mathrm{e} = N_\mathrm{d}^+. \tag{A.4}$$

Here, N_d^+ is the ionized donor density given by

$$N_\mathrm{d}^+ = \frac{N_\mathrm{d}/2}{1 + 2\exp\left(\dfrac{E_\mathrm{Fs} - E_\mathrm{d,h}}{k_\mathrm{B}T}\right)} + \frac{N_\mathrm{d}/2}{1 + 2\exp\left(\dfrac{E_\mathrm{Fs} - E_\mathrm{d,k}}{k_\mathrm{B}T}\right)}, \tag{A.5}$$

where $E_\mathrm{d,h}$ and $E_\mathrm{d,k}$ are the donor levels at hexagonal (h-) and cubic (k-) sites, respectively. Note that Eq. (A.5) assumes that the dopants equally occupy h- and k-sites.

The above equations allow computing E_Fs and n_e with the procedure described below. In the calculation, N_d dependence of the ionization energy of the dopants ($\Delta E_\mathrm{d} = E_\mathrm{C} - E_\mathrm{d}$),

$$\Delta E_\mathrm{d}(N_\mathrm{d}) = \begin{cases} \Delta E_\mathrm{d0} - \alpha_\mathrm{d} N_\mathrm{d}^{1/3} & (\Delta E_\mathrm{d} > 0) \\ 0 & (\text{otherwise}) \end{cases}, \tag{A.6}$$

was taken into account, where ΔE_d0 and α_d are constants. The physical properties of SiC related to the E_Fs and n_e calculation are listed in Table A.1 [3–5].

A.2 Boltzmann Approximation

For lightly-doped semiconductors in which E_Fs is far from E_C satisfying the relationship $E_\mathrm{C} - E_\mathrm{Fs} > 2.3 k_\mathrm{B}T$, so-called non-degenerate semiconductors, the Boltzmann approximation simplifies Eq. (A.3) as

$$F_\mathrm{B}(E) = \exp\left(-\frac{E - E_\mathrm{Fs}}{k_\mathrm{B}T}\right). \tag{A.7}$$

In this case, the integral in Eq. (A.1) can be analytically solved as

$$n_\mathrm{e} = 2M_\mathrm{C}\left(\frac{m_\mathrm{dse}^* k_\mathrm{B}T}{2\pi\hbar^2}\right)^{3/2} \exp\left(-\frac{E_\mathrm{C} - E_\mathrm{Fs}}{k_\mathrm{B}T}\right) = N_\mathrm{C}\exp\left(-\frac{E_\mathrm{C} - E_\mathrm{Fs}}{k_\mathrm{B}T}\right), \tag{A.8}$$

where N_C is the effective density of state in the conduction band. As a result, the charge neutrality equation is rewritten as

$$n_\mathrm{e} = \frac{N_\mathrm{d}/2}{1 + 2\dfrac{n_\mathrm{e}}{N_\mathrm{C}}\exp\left(\dfrac{\Delta E_\mathrm{d,h}}{k_\mathrm{B}T}\right)} + \frac{N_\mathrm{d}/2}{1 + 2\dfrac{n_\mathrm{e}}{N_\mathrm{C}}\exp\left(\dfrac{\Delta E_\mathrm{d,k}}{k_\mathrm{B}T}\right)}. \tag{A.9}$$

The electron density is obtained by solving this equation for n_e, and then, the Fermi level is determined with n_e as

$$\Delta E_\mathrm{Fs} = E_\mathrm{C} - E_\mathrm{Fs} = k_\mathrm{B}T\ln\left(\frac{N_\mathrm{C}}{n_\mathrm{e}}\right). \tag{A.10}$$

Table A.1: Physical properties of SiC used in this study to calculate the Fermi level and electron density in n-type SiC [3–5].

M_{C}	m^{*}_{dse} (m_0)	$\Delta E_{\mathrm{d0,h}}$ (eV)	$\Delta E_{\mathrm{d0,k}}$ (eV)	$\alpha_{\mathrm{d,h}}$ (eV cm)	$\alpha_{\mathrm{d,k}}$ (eV cm)
3	0.39	0.071	0.124	4×10^{-8}	4×10^{-8}

A.3 Numerical Approach Based on Fermi-Dirac Statistics

When N_d becomes higher and E_Fs becomes closer to E_C, the Boltzmann approximation comes to be invalid, and thus, the charge neutrality equation (A.4) has to be numerically solved with Eqs. (A.1) and (A.5). The procedure is as follows;

1. n_e is numerically calculated at a given E_Fs based on Eq. (A.1).
2. N_d^+ is obtained with the same E_Fs according to Eq. (A.5).
3. The difference between n_e and N_d^+ is evaluated.
4. The above procedures are repeated by varying E_Fs until n_e and N_d^+ become identical.
5. n_e and E_Fs at the convergence are extracted.

A.4 Calculation Results

Figure A.1 compares the electron density and the Fermi level in n-type SiC calculated based on the Boltzmann approximation and the numerical computation. Although the calculated values agree well with each other in the case of $N_\mathrm{d} < 1 \times 10^{17}\,\mathrm{cm}^{-3}$, n_e and E_Fs based on the Boltzmann approximation deviate from those obtained by the numerical calculation in the higher N_d range. Since an extensive range of N_d is treated in this study, the calculation of n_e and E_Fs is performed through the numerical approach.

References

[1] S. M. Sze, Y. Li, and K. K. Ng, *Physics of Semiconductor Devices* (John Wiley & Sons, 4th edition, 2021).

[2] B. L. Anderson and R. L. Anderson, *Fundamentals of semiconductor devices* (McGraw-Hill Higher Education, 2005).

[3] D. Volm, B. K. Meyer, D. M. Hofmann, W. M. Chen, N. T. Son, C. Persson, U. Lindefelt, O. Kordina, E. Sörman, A. O. Konstantinov, B. Monemar, and E. Janzén, *Phys. Rev. B* **53**, 15409 (1996).

[4] S. Kagamihara, H. Matsuura, T. Hatakeyama, T. Watanabe, M. Kushibe, T. Shinohe, and K. Arai, *J. Appl. Phys.* **96**, 5601 (2004).

[5] T. Kimoto and J. A. Cooper, *Fundamentals of Silicon Carbide Technology: Growth, Characterization, Devices and Applications* (John Wiley & Sons, 2014).

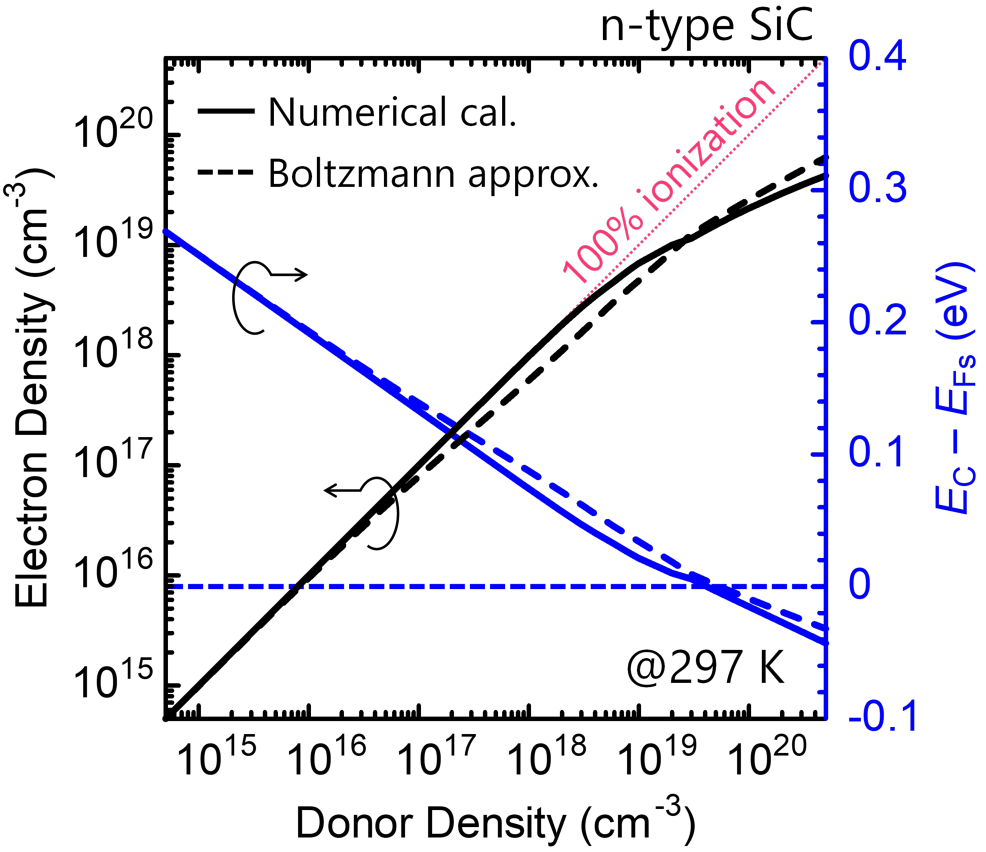

Figure A.1: Donor density dependence of the electron density and Fermi level in n-type SiC calculated based on the Boltzmann approximation and numerical computation.

Appendix B

New Process Proposal for Low-Temperature Formation of Ohmic Contacts on *n*-Type SiC

B.1 Introduction

Chapter 5 proposed a physics-based model to predict the contact resistivity (ρ_c) at non-alloyed ohmic contacts on SiC, considering the contributions of direct tunneling (DT) and trap-assisted tunneling (TAT). Based on the proposed model, the author suggested two potential approaches toward low-resistance ohmic contacts on n-type SiC in Chap. 5: (1) insertion of a silicon (Si) interlayer for barrier height lowering and (2) creation of sulfur (S) deep donor levels for enhanced TAT current. In this chapter, the author's recent trials regarding these new processes toward the formation of low-resistance ohmic contacts are presented.

B.2 Insertion of a Silicon Interlayer for Barrier Height Lowering

B.2.1 Basic Concept

Chapter 5 revealed that a very low ρ_c ($< 10^{-6}\,\Omega\mathrm{cm}^2$) can be achieved with a low zero-field barrier height (ϕ_{B0}) of lower than about 1 eV. Due to the chemical and physical instability of metals with a low work function (ϕ_m), the author takes interlayer insertion as a promising pathway for lowering the barrier height [1]. According to the requirements for the interlayer mentioned in Sect. 5.5, Si is focused on as a potential candidate for interlayer-based ohmic contact formation. Figure B.1 depicts the energy band alignment among SiC, Si, and several metals. Regarding the contact formation on n-type SiC, a lower energy barrier at a Si/SiC

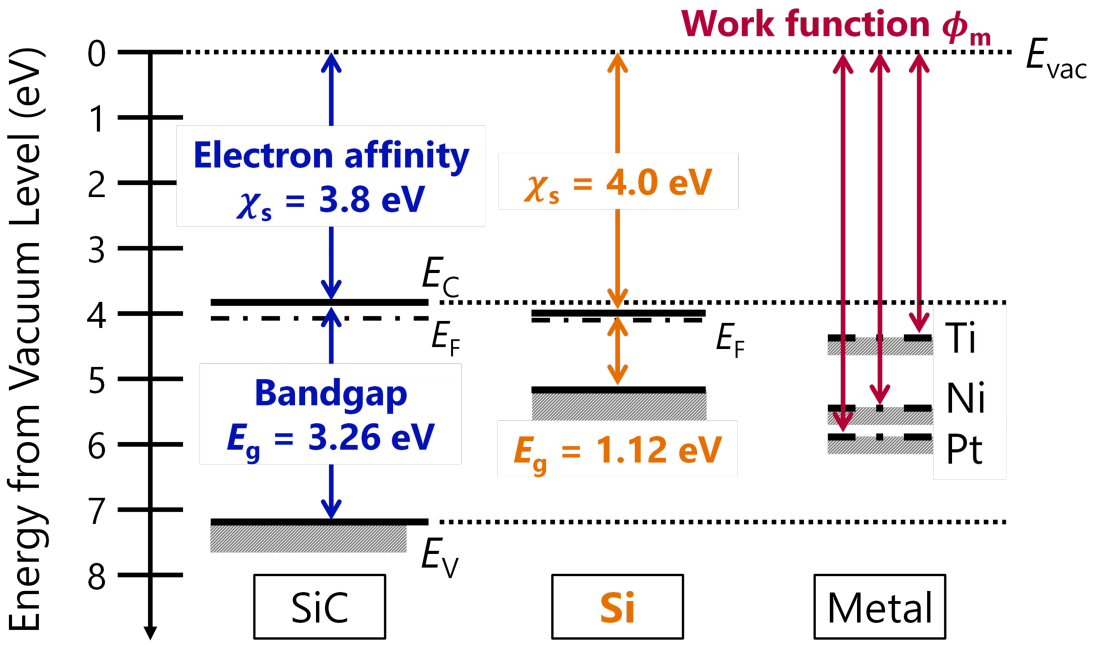

Figure B.1: Energy band diagram of SiC, Si, and several metals (Ti, Ni, and Pt).

interface is expected than at Ti/SiC interfaces by heavily doping a donor into Si. Barrier height reduction at a metal/Si interface is another crucial point, which can be achieved through a mature fabrication process based on silicide formation by thermal treatment.

Several groups have tried to form ohmic contacts by introducing a Si interlayer and have characterized the ρ_c values so far [2–5]. However, these previous reports often intended to suppress carbon accumulation during nickel silicide formation in the standard process [6]. Besides, high-temperature post-metallization annealing ($> 800°C$) was performed to reduce ρ_c, and the obtained ρ_c values were not sufficiently low. On the other hand, the main point of the author's proposal is barrier height engineering by forming Si/SiC junctions, and the Si interlayer should remain after an annealing process. Thus, the proposed concept is more similar to that reported by Tanaka *et al.* [7], in which p-type polycrystalline Si is employed as a Schottky electrode to achieve a low forward voltage drop and low leakage current in SBDs.

In this study, the author proposes a new process as follows: (1) a metal/n-Si stack is deposited on n-type SiC, (2) the stack is annealed ($\sim 600°C$) to cause an interfacial reaction between metal and Si, and (3) a metal/silicide/n-Si/n-SiC stack with a low barrier height is formed. Thermal treatment with a proper condition is critical in this process, which has to ensure the Si interlayer remains after annealing and keeps the Si/SiC interface, as mentioned above. According to a review paper by Gambino and Colgan [8], the final state of the stack basically depends on the thickness ratio between the metal and Si; a silicide/Si stack is formed after thermal treatment when the Si film is thicker than the metal, while, with a thinner Si film, the metal layer remains on silicide and Si is fully consumed. Table B.1 summarizes the formation temperature and the amount of Si consumed during the reaction for various silicides [8]. Based on these properties, annealing conditions and the thickness of Si and metal films have to be appropriately designed.

B.2.2 Design and Formation of Metal/Silicon/SiC Stacks

In this study, vertical Schottky barrier diodes (SBDs) were fabricated on an n-type SiC epitaxial layer (net donor density: $N_d \simeq 1 \times 10^{16}\,cm^{-3}$) with a Ni/n-Si stack as a Schottky electrode to investigate the barrier height. Si was deposited on the epitaxial layer via resistive heating evaporation by using reed-shaped small chips taken from an antimony (Sb)-doped Si wafer with a resistivity of $0.01\,\Omega cm$ (corresponding to $N_d \simeq 5 \times 10^{18}\,cm^{-3}$ [9]), followed by Ni deposition on the top. Electrode patterning was performed with a lithography and lift-off process. The Fermi level in the deposited Si is expected to be located at 0.1 eV below the conduction band edge (E_C), resulting in a work function of about 4.1 eV. Since this value is comparable to or lower than ϕ_m of Ti [10], a similar or lower barrier height is ideally expected. The thickness of the deposited Si film was 79 nm, and two different conditions of the Ni thickness (60 and 196 nm) were prepared, intending to leave the Si layer and entirely consume the Si layer after annealing, respectively. After the Schottky

Table B.1: Formation temperature and amount of Si consumed during the reaction for various silicide materials [8].

Silicide	$CoSi_2$	Pd_2Si	NiSi	$NiSi_2$	$TiSi_2$
Formation temperature (°C)	600–700	200–500	400–600	600–700	600–700
Si consumed per nm of metal (nm)	3.6	0.7	1.8	3.6	2.3

electrode deposition, some samples were annealed at 500°C for 2 min or 600°C for 3 min in N_2 ambient, and no annealing was performed on the others. Based on Table B.1, NiSi and $NiSi_2$ are expected to be the main phases when the Ni/Si stack is annealed at 500°C and 600 °C, respectively. Finally, Al backside electrodes were deposited on the n-type SiC substrate. Capacitance–voltage (C–V) measurement was conducted on the fabricated SBDs to extract ϕ_{B0}. Note that current–voltage (I–V) characteristics were also investigated, and rectification was confirmed for all the samples, indicating Schottky contact formation at the Si/SiC interface.

B.2.3 Barrier Height Characterization

Figure B.2 plots the ϕ_{B0} values in the SiC SBDs with Ni/Si-stack-based Schottky electrodes formed with various annealing conditions and Ni thicknesses. In the non-sintered Si/SiC structures, the barrier height of $\phi_{B0} \simeq 1.3$ eV is obtained, which is higher than predicted from the work function of the Si evaporation source. Since the deposited film is expected to be amorphous, the same donor density of Si before and after deposition is not necessarily guaranteed. This result indicates that taking another method to deposit Si (e.g., chemical vapor deposition) and/or performing additional doping into the Si thin film are required for barrier height lowering.

In the sintered stacks, ϕ_{B0} is determined as about 1.6–1.8 eV, almost regardless of the annealing conditions and Ni thicknesses. These values agree with the reported barrier height at nickel silicide/SiC Schottky contacts annealed at a low temperature ($\sim$ 600°C) [11, 12]. Therefore, it is speculated that the Si interlayer was totally consumed, and nickel silicide/SiC interfaces were formed in every annealing condition. According to Table B.1, the thickness of the Si film should be twice or four times thicker than Ni to make the Si interlayer remain during the NiSi or $NiSi_2$ reaction, respectively. Since the structure optimization is insufficient at the present stage, exploring appropriate Ni/Si thickness ratio and annealing conditions are essential for demonstrating a low barrier height.

B.2.4 Discussion

As seen in the former section, the ϕ_{B0} values obtained by the present process are above 1 eV and insufficient to achieve a very low ρ_c ($< 10^{-6}\,\Omega\mathrm{cm}^2$). In order to optimize the stack structure and fabrication process, chemical and structural analyses, such as X-ray photoelectron spectroscopy (XPS) and transmission electron microscopy (TEM), are indispensable. If a sufficiently low barrier height can be obtained with an improved stack formation process, low-temperature formation of low-resistance ohmic contacts may be demonstrated through ρ_c characterization at contacts formed on heavily phosphorus (P)-implanted SiC. Although there is much room to refine the proposed process, the author believes that this concept can potentially be adopted for the practical ohmic contact formation process.

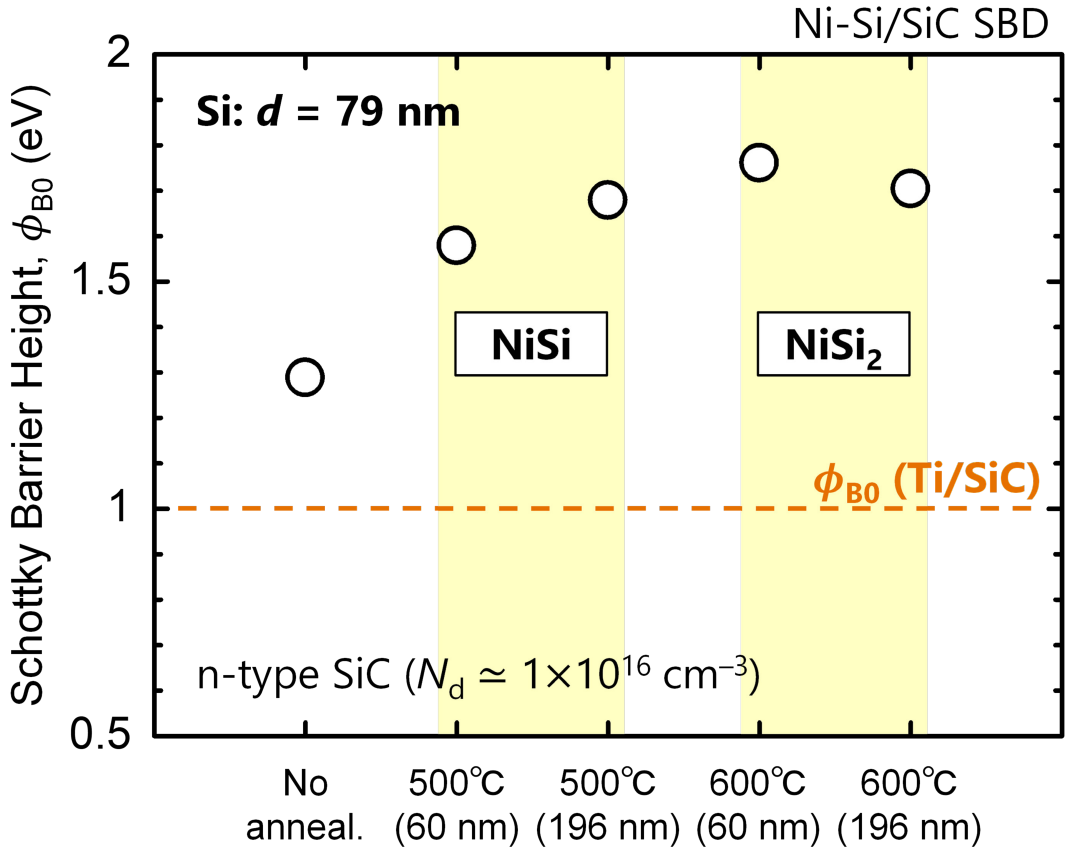

Figure B.2: Zero-field barrier height (ϕ_{B0}) in the Ni/Si/SiC Schottky structures formed with various annealing conditions and Ni thicknesses.

B.3 Creation of Sulfur Deep Donor Levels for Enhanced Trap-Assisted Tunneling

B.3.1 Basic Concept

Chapter 5 clarified that ρ_c is significantly reduced by the contribution of TAT, especially in the N_d range below about $10^{20}\,cm^{-3}$. As schematically illustrated in Fig. B.3, controlling the trap density (or deep level density, N_T) is expected to greatly impact the ρ_c value in this N_d range. In this sense, an intentional introduction of deep levels may be an effective way to achieve ρ_c with relatively low-dose P^+ implantation (N_d: below mid-$10^{19}\,cm^{-3}$), which does not require high-temperature implantation and reduces the process cost.

Since the point is forming "deep levels" in the bandgap of SiC, the author focuses on the S impurity that acts as a deep and double donor in SiC [13, 14], as depicted in Fig. B.4. Based on the prediction in Chap. 4, these energy levels (0.3–0.5 eV below E_C) seem to effectively enhance the TAT current. Besides, the depth profile of S atoms is controllable in a wide density range (1×10^{17}–$1 \times 10^{20}\,cm^{-3}$) by ion implantation [15]. As a result, S impurities can be regarded as "intentionally formable and controllable deep levels."

B.3.2 Design and Formation of Phosphorus and Sulfur Co-Implanted Regions

Since S donor levels are very deep, and the solubility limit is indicated to be very low ($\sim 2 \times 10^{18}\,cm^{-3}$) [15], P^+ implantation is necessary to form a low-resistance implanted region. In this study, I–V characteristics of SBDs fabricated with P-implanted SiC and P/S co-implanted SiC are compared to investigate the effect of the additional S^+ implantation.

The starting material was an n-type SiC epitaxial layer ($10^{15}\,cm^{-3}$) grown on an n-type 4H-SiC(0001) substrate. P^+ implantation with various P atom densities (N_P) of 9.0×10^{18} and $8.0 \times 10^{19}\,cm^{-3}$ was conducted at room temperature and 500°C, respectively, and about 200 nm-deep box-shaped implantation profiles were created. Then, S^+ implantation with the S atom density (N_S) of $1 \times 10^{18}\,cm^{-3}$ was performed at room temperature for some samples. Note that the N_S value was set to be below the reported solubility limit [15]. After the activation annealing (1750°C, 20 min, Ar ambient) and subsequent sacrificial oxidation (1300°C, 60 min), Ti Schottky electrodes were formed on the implanted layers via resistive heating evaporation. Backside ohmic contacts were formed by depositing Al onto the substrate. The I–V characteristics of the fabricated SBDs were measured at room temperature, and effects of the additional S^+ implantation were investigated.

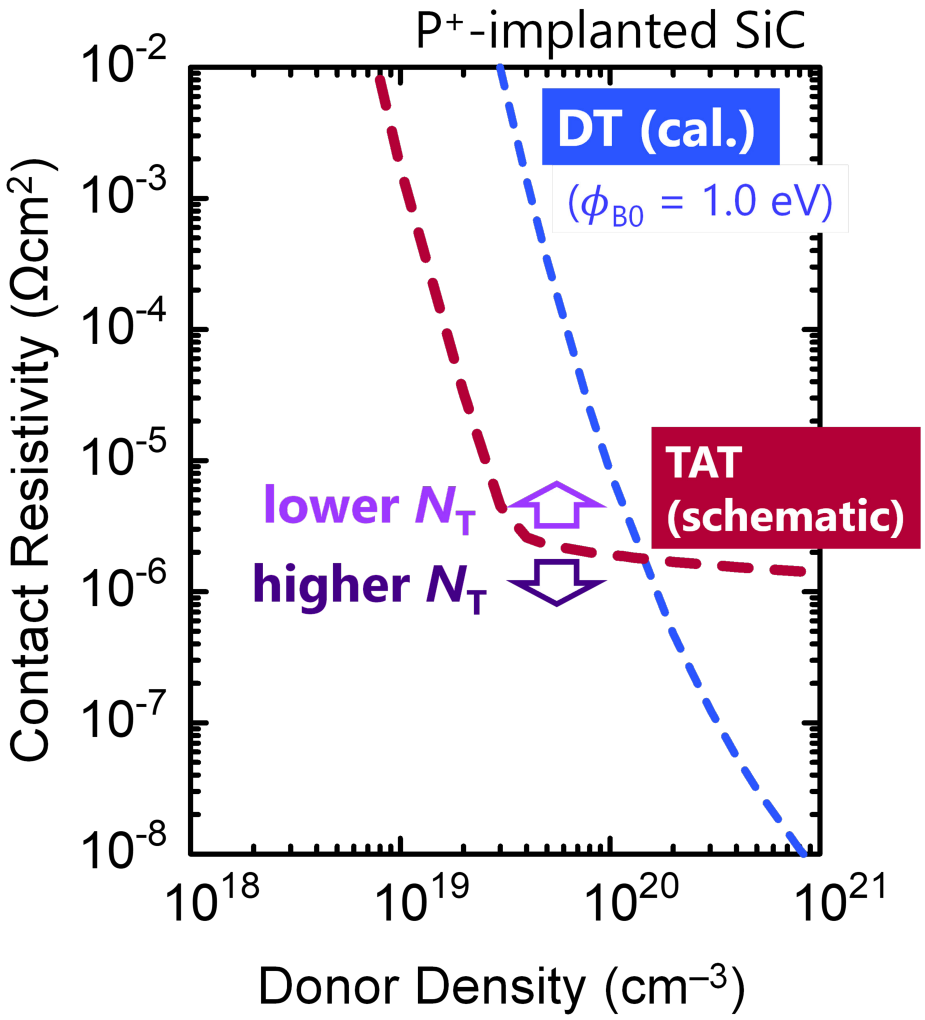

Figure B.3: Schematic illustration of an N_T-dependent change in the contribution of TAT to the contact resistivity reduction.

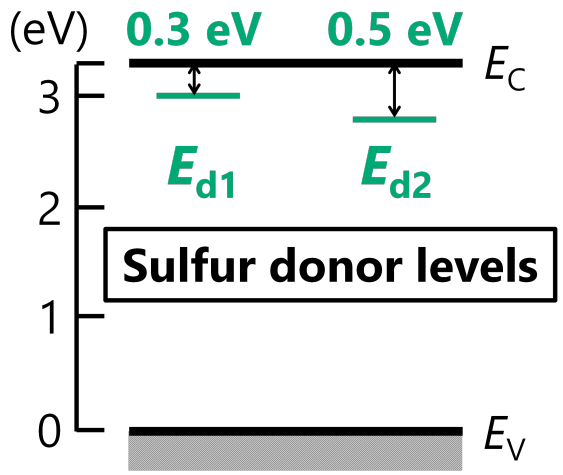

Figure B.4: Donor levels of S impurities in SiC [13, 14].

B.3.3 Current–Voltage Characteristics

Figure B.5 compares the *I–V* characteristics of the Ti/SiC SBDs fabricated with P-implanted and P/S co-implanted samples. The current density in the P/S co-implanted samples is about 1.2 times larger than only the P-implanted ones at $N_{\mathrm{P}} = 9 \times 10^{18}\,\mathrm{cm}^{-3}$, while the additional S^+ implantation less affects the *I–V* curves at a higher N_{P} of $8 \times 10^{19}\,\mathrm{cm}^{-3}$. The N_{P}-dependent difference in how effective the P/S co-implantation for enhanced current density seems consistent with the N_{d}-dependent change in the contribution of TAT discussed in Chap. 5. Since it is reported that there is no barrier height difference between S- and P-implanted SiC SBDs [16], it is indicated that the increased current density may be attributed to the enhanced TAT current by the introduced S deep levels. On the other hand, the donor density in the P/S co-implanted samples is higher by $2 \times 10^{18}\,\mathrm{cm}^{-3}$, which can also be responsible for the larger tunneling current. Consequently, the mechanism of the enhanced current in the P/S co-implanted SiC SBDs is still controversial, and further detailed investigation is necessary.

B.3.4 Discussion

The former section indicated the effectiveness of intentionally creating S deep levels for enhanced TAT current based on the *I–V* characteristics in vertical SBDs. However, the increase in the current density is less than twice at about $N_{\mathrm{d}} = 1 \times 10^{19}\,\mathrm{cm}^{-3}$, and it is still unclear what mainly contributes to the current enhancement by the additional S implantation. In addition, ρ_{c} characterization in P/S co-implanted samples has still not been performed. Since it is reported that S implantation with N_{S} higher than the solubility limit still leads to a larger current in SBDs [16], varying N_{S} in a wide range up to about $10^{20}\,\mathrm{cm}^{-3}$ will be effective in further investigating the effect of S implantation. Besides, the implantation of other impurities or even host material atoms (Si or C) can also contribute to the enhanced TAT current if they form a deep level in the bandgap of SiC. Thus, it is crucial to explore an implant material that can improve ρ_{c} at SiC ohmic contacts based on previous numerical and experimental studies regarding deep levels in SiC [17]. In adopting the new process for practical fabrication, additional-impurity-related reliability issues and sintering-induced changes in the contact property should be carefully investigated.

B.4 Summary

In this chapter, the author proposed two new processes for the low-temperature formation of low-resistance ohmic contacts on SiC and investigated several fundamental contact properties with these processes.

Ni/Si electrode stack-based barrier height engineering was demonstrated by controlling Ni and Si thicknesses and varying the annealing temperature. Although the minimum

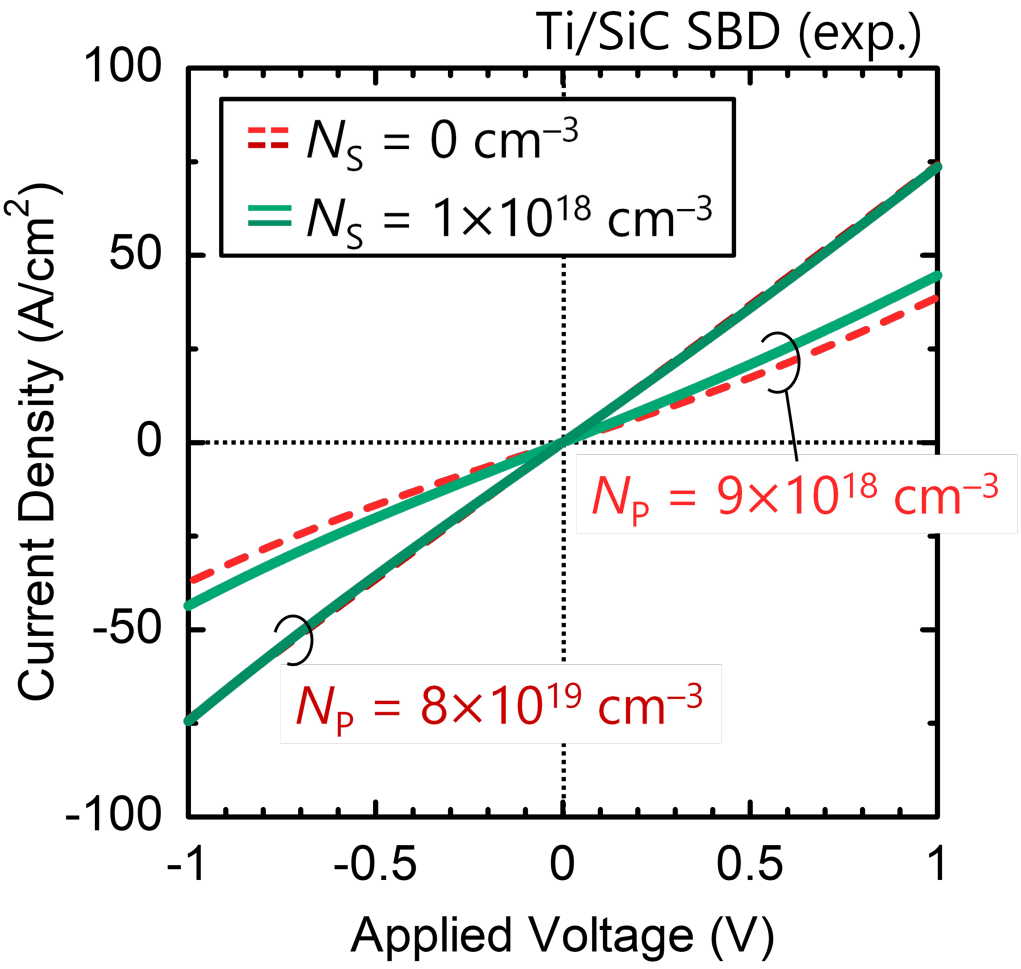

Figure B.5: I–V characteristics of the Ti/n-type SiC SBDs fabricated with P-implanted SiC ($N_\mathrm{P} = 9 \times 10^{18}$ and $8 \times 10^{19}\,\mathrm{cm}^{-3}$) and P/S co-implanted SiC ($N_\mathrm{P} = 9 \times 10^{18}$ and $8 \times 10^{19}\,\mathrm{cm}^{-3}$ with $N_\mathrm{S} = 0$ or $1 \times 10^{18}\,\mathrm{cm}^{-3}$).

barrier height was $\phi_{B0} \simeq 1.3\,\mathrm{eV}$ at the present stage, which is insufficient to obtain a sufficiently low contact resistivity ($< 10^{-6}\,\Omega\mathrm{cm}^2$), several approaches and crucial aspects to improve the interlayer-based process were suggested.

Aiming to enhance the TAT current by intentionally introducing "deep levels," phosphorus (P) and sulfur (S) co-implantation was performed in fabricating SBDs. The current density in the P/S co-implanted SiC SBDs was about 1.2 times larger than that of only P-implanted samples. The necessity of further investigation of the mechanism of the increased current density in the SBDs, the contact resistivity value, effects of the implantation of other material atoms, and thermal stability was pointed out for putting the process into practice.

There is quite a large room to improve the present process. By addressing the remaining issues, the author hopes the proposed concept and process will contribute to developing a more cost-efficient fabrication process and encouraging the prevalence of SiC devices in modern society.

References

[1] F. A. Mohammad, Y. Cao, and L. M. Porter, *J. Electron. Mater.* **36**, 312 (2007).

[2] T. Jang, J. W. Erickson, and L. M. Porter, *J. Electron. Mater.* **31**, 506 (2002).

[3] W. Y. Lee, K. S. Teng, and S. P. Wilks, *Mater. Sci. Forum* **457–460**, 849 (2004).

[4] O. J. Guy, G. Pope, I. Blackwood, K. S. Teng, L. Chen, W. Y. Lee, S. P. Wilks, and P. A. Mawby, *Surf. Sci.* **573**, 253 (2004).

[5] H. Hanafusa, A. Ohta, R. Ashihara, K. Maruyama, T. Mizuno, S. Hayashi, H. Murakami, and S. Higashi, *Mater. Sci. Forum* **778–780**, 649 (2014).

[6] J. Crofton, L. M. Porter, and J. R. Williams, *Phys. Stat. Sol. B* **202**, 581 (1997).

[7] H. Tanaka, T. Hayashi, Y. Shimoida, S. Yamagami, S. Tanimoto, and M. Hoshi, *2005 17th International Symposium on Power Semiconductor Devices & ICs (ISPSD)* (2005), p. 287.

[8] J. P. Gambino and E. G. Colgan, *Mater. Chem. Phys.* **52**, 99 (1998).

[9] S. M. Sze and J. C. Irvin, *Solid State Electron.* **11**, 599 (1968).

[10] H. B. Michaelson, *J. Appl. Phys.* **48**, 4729 (1977).

[11] F. La Via, F. Roccaforte, V. Raineri, M. Mauceri, A. Ruggiero, P. Musumeci, L. Calcagno, A. Castaldini, and A. Cavallini, *Microelectron. Eng.* **70**, 519 (2003).

[12] L. Calcagno, A. Ruggiero, F. Roccaforte, and F. La Via, *J. Appl. Phys.* **98**, 023713 (2005).

[13] S. A. Reshanov, G. Pensl, H. Nagasawa, and A. Schöner, *J. Appl. Phys.* **99**, 123717 (2006).

[14] T. Matsuoka, M. Kaneko, and T. Kimoto, *Jpn. J. Appl. Phys.* **62**, 010908 (2023).

[15] T. Matsuoka, M. Kaneko, and T. Kimoto, *International Conference on Silicon Carbide and Related Materials 2022* (Davos, 2022), Th-2-A.2.

[16] M. Takayasu, T. Matsuoka, M. Hara, M. Kaneko, and T. Kimoto, *International Conference on Silicon Carbide and Related Materials 2023* (Sorrento, 2023), Process 6-1.

[17] T. Kimoto and J. A. Cooper, *Fundamentals of Silicon Carbide Technology: Growth, Characterization, Devices and Applications* (John Wiley & Sons, 2014).

List of Publications

A. Original Papers (Peer Reviewed)

1. M. Hara, S. Asada, T. Maeda, and T. Kimoto,
"Forward thermionic field emission transport and significant image force lowering caused by high electric field at metal/heavily-doped SiC Schottky interfaces,"
Applied Physics Express **13**, 041001 (2020).

2. M. Hara, M. Kaneko, and T. Kimoto,
"Nearly Fermi-level-pinning-free interface in metal/heavily-doped SiC Schottky structures,"
Japanese Journal of Applied Physics **60**, SBBD14 (2021).

3. R. Ishikawa, M. Hara, H. Tanaka, M. Kaneko, and T. Kimoto,
"Electron mobility along $\langle 0001 \rangle$ and $\langle 1\bar{1}00 \rangle$ directions in 4H-SiC over a wide range of donor concentration and temperature,"
Applied Physics Express **14**, 061005 (2021).

4. M. Hara, H. Tanaka, M. Kaneko, and T. Kimoto,
"Critical electric field for transition of thermionic field emission/field emission transport in heavily doped SiC Schottky barrier diodes,"
Applied Physics Letters **120**, 172103 (2022).
[Featured as an APL Editor's Pick]

5. M. Hara, M. Kaneko, and T. Kimoto,
"Enhanced tunneling current and low contact resistivity at Mg contacts on heavily phosphorus-ion-implanted SiC"
Applied Physics Express **16**, 021003 (2023).

6. T. Kitawaki, M. Hara, H. Tanaka, M. Kaneko, and T. Kimoto,
"Impact of the split-off band on the tunneling current at metal/heavily-doped p-type SiC Schottky interfaces,"
Applied Physics Express **16**, 031005 (2023).

7. M. Hara, T. Kitawaki, H. Tanaka, M. Kaneko, and T. Kimoto,
"Tunneling current through non-alloyed metal/heavily-doped SiC interfaces,"
Materials Science in Semiconductor Processing **171**, 108023 (2024).
[Invited Review Paper]

8. M. Hara, H. Tanaka, M. Kaneko, and T. Kimoto,
"Trap-assisted tunneling current in metal/heavily-doped SiC Schottky structures induced by phosphorus ion implantation,"
in preparation.

B. International Conferences (Peer Reviewed)

1. M. Hara, S. Asada, T. Maeda, and T. Kimoto,
"Forward Thermionic Field Emission Current and Barrier Height Lowering in Heavily-Doped 4H-SiC Schottky Barrier Diodes,"
International Conference on Silicon Carbide and Related Materials 2019,
Kyoto (Japan), Sep.–Oct. (2019), Oral, We-3A-02.

2. M. Hara, S. Asada, T. Maeda, and T. Kimoto,
"Significant Image Force Lowering at Metal/Heavily-Doped SiC Interfaces,"
The 9th Asia-Pacific Workshop on Widegap Semiconductors,
Okinawa (Japan), Nov. (2019), Oral, ED3-4.

3. M. Hara, M. Kaneko, and T. Kimoto,
"Accurate Determination of Barrier Heights in Heavily-Doped SiC Schottky Barrier Diodes Fabricated with Various Metals,"
2020 International Conference on Solid State Devices and Materials,
Virtual, Sep. (2020), Oral, D-4-01.

4. R. Ishikawa, M. Hara, H. Tanaka, M. Kaneko, and T. Kimoto,
"High electron mobility along the *c*-axis in 4H-SiC,"
2020 International Conference on Solid State Devices and Materials,
Virtual, Sep. (2020), Oral, D-4-02.

5. M. Hara, H. Tanaka, M. Kaneko, and T. Kimoto,
"Ideal Thermionic Field Emission and Field Emission Transport through Metal/Heavily-Doped SiC Schottky Barriers,"
European Conference on Silicon Carbide and Related Materials 2020/2021,
Tours (France)/Virtual, Oct. (2021), Oral, Tu-3B-01.
[Best Oral Presentation Award]

6. R. Ishikawa, M. Hara, H. Tanaka, M. Kaneko, and T. Kimoto,
"Anisotropy of electron mobility in 4H-SiC over wide ranges of donor concentration and temperature,"
European Conference on Silicon Carbide and Related Materials 2020/2021,
Tours (France)/Virtual, Oct. (2021), Oral, Tu-4B-01.

7. M. Hara, M. Kaneko, and T. Kimoto,
"Enhanced tunneling current at Schottky contacts formed on heavily P^+-implanted SiC,"
International Conference on Silicon Carbide and Related Materials 2022,
Davos (Switzerland), Sep. (2022), Oral, Tu-4-B.1.

8. T. Kitawaki, M. Hara, H. Tanaka, M. Kaneko, and T. Kimoto,
"Contribution of a split-off band to tunneling current in heavily-doped p-type SiC Schottky barrier diodes,"
International Conference on Silicon Carbide and Related Materials 2022,
Davos (Switzerland), Sep. (2022), Oral, We-4-B.2.

9. M. Kaneko, M. Hara, M. Nakajima, Q. Jin, and T. Kimoto,
"Ion Implantation Technology in SiC for Advanced Electron Devices" (invited),
International Conference on Ion Implantation Technology 2022,
San Diego (USA), Sep. (2022), Oral, TU1.04.

10. T. Kimoto, H. Niwa, X. Chi, M. Hara, R. Ishikawa, H. Tanaka, and M. Kaneko,
"High-Field Phenomena in SiC Material and Devices" (invited),
Symposium on Silicon Carbide as Quantum-Classical Platform,
Erlangen (Germany), Sep. (2023), Oral, 4-1.

11. M. Takayasu, T. Matsuoka, M. Hara, M. Kaneko, and T. Kimoto,
"Carrier transport and barrier height of S^+-implanted SiC Schottky barrier diodes,"
International Conference on Silicon Carbide and Related Materials 2023,
Sorrento (Italy), Sep. (2023), Oral, Process 6-1.

12. M. Hara, M. Kaneko, and T. Kimoto,
"Reduction of contact resistivity at non-alloyed SiC ohmic contacts based on understanding of tunneling phenomena,"
International Conference on Silicon Carbide and Related Materials 2023,
Sorrento (Italy), Sep. (2023), Oral, Process 6-2.

13. K. Kuwahara, T. Kitawaki, M. Hara, M. Kaneko, and T. Kimoto,
"Formation of non-alloyed ohmic contacts on heavily Al^+-implanted p-type SiC,"
International Conference on Silicon Carbide and Related Materials 2023,
Sorrento (Italy), Sep. (2023), Oral, Process 6-3.